

**Design, Analysis and Fabrication
of Micro Optical Systems involving UV-Deep Lithography
- with an Application in Atomic Physics**

Inauguraldissertation
zur Erlangung des akademischen Grades
eines Doktors der Naturwissenschaften
der Universität Mannheim

vorgelegt von

Diplom-Informatikerin
Xiyuan Liu
aus China

Mannheim, 2008

Dekan: Prof. Dr. Felix Freiling, Universität Mannheim
Referent: Prof. Dr. Karl-Heinz Brenner, Universität Mannheim
Korreferent: Prof. Dr. Jürgen Jahns, FernUniversität Hagen

Tag der mündlichen Prüfung: 17. Oktober 2008

Abstract

Integrated free space optics is a widespread and important field in today's technology. This study outlines one application in atomic physics and quantum optics. Since optimized design requires the adequate mathematical treatment of light propagation in free space, this study deals with the various existing scalar methods of light propagation, including plane wave expansion, the Fresnel approximation, and ray-transfer matrices applied to geometrical optics and the ABCD-law for Gaussian beams. As do other scientific methods, these mathematical treatments have their own prerequisites. Consequently, the application scope of these methods is restricted. This thesis aims at relaxing some prerequisites for conventional methods and also at demonstrating new application aspects. Using a research project in atomic physics as an application example, this thesis is restricted to two main research fields: micro optics and deep lithography. The topic comprises a design tool for minimal optical systems, energy investigation in scalar fields, mask diffraction in thick absorbing resists with partially coherent illumination, a phase reconstruction method using the ambiguity function, lithographic fabrication of alignment structures for a fiber resonator, and fabrication of micro lenses using replication techniques.

Zusammenfassung

Integrierte Freiraum-Optik ist umfassend und auch bedeutend in der heutigen Technologie. Die vorliegende Arbeit befasst sich mit einer Anwendung in der Atomphysik und Quantenoptik. Da ein optimierter Entwurf eine adäquate mathematische Behandlung der Lichtausbreitung erfordert, beschäftigt sich diese Arbeit mit diversen skalaren Theorien für Lichtausbreitung. Dazu gehören die Zerlegung nach ebenen Wellen, die Fresnel-Näherung, sowie die Strahl-Transfermatrizen für geometrische Optik und das ABCD-Gesetz für Gauß-Strahlen. Wie alle anderen wissenschaftlichen Methoden haben die mathematischen Behandlungen auch ihre eigenen Anwendungsbedingungen. Ziel dieser Arbeit ist, die Anwendungsbedingungen zu erleichtern und folglich neue Anwendungsbereiche zu demonstrieren. Diese Arbeit hat zwei wesentlichen Bestandteile: Mikrooptik und UV-Tiefenlithografie. Die Hauptthemen sind das Systemdesign durch minimale Matrixzerlegung, die Energieanalyse für skalare Felder, Lichtausbreitung in absorbierenden Medien mit teilkohärenter Beleuchtung, Phasenrekonstruktion mit Ambiguity-Funktion, lithografische Fertigung der Alignmentstrukturen für einen Faserresonator und die Abformung der Mikrolinsen.

Information is physical.
Rolf Landauer

Contents

I	Introduction	1
1	Introduction and overview	3
1.1	Overview - Miniaturized optics for atom detection as an application example in atomic physics	3
II	Design and Analysis of Micro Optical Systems and their Components	9
2	Optical system design based on ray transfer matrices	11
2.1	Introduction	11
2.2	One-dimensional optics	13
2.2.1	Commonly used optical components	14
2.2.2	System realization using matrix decomposition	15
2.2.3	Minimal realization consisting of thin lenses and propagations	18
2.3	Extension to two-dimensional optics	21
2.3.1	Commonly used optical components	23
2.3.2	System realization using matrix decomposition	27
2.3.3	Minimal realization consisting of thin lenses and propagations	27
2.4	Conclusion	34
3	Investigating energy flow in scalar wave fields	37
3.1	Introduction and motivation	38
3.2	Scalar field flux according to Born/Wolf	40
3.3	Generalizing the energy flux for media with complex refractive indices	41
3.4	Two examples comparing energy flux, the Poynting-vector and $ u ^2$	43
3.4.1	Standing wave	44
3.4.2	Interference of two plane waves	46
3.4.3	Summary and conclusion	48
3.5	Energy conservation in various scalar theories	48

3.5.1	Single plane wave	49
3.5.2	Plane wave expansion based on the continuity of u	49
3.5.3	Plane wave expansion based on the continuity of $\partial u/\partial z$	50
3.5.4	Kirchhoff diffraction	52
3.5.5	Debye approximation	53
3.6	Conditions for energy conservation behind a thin optical element	54
3.7	Conclusion	58
4	Coherent mask diffraction in absorbing photoresists	59
4.1	Introduction	60
4.2	Electromagnetic plane waves in media with complex refractive indices	62
4.3	Electromagnetic plane wave at an absorbing interface	64
4.4	Non-paraxial light propagation in absorbing media	69
4.5	An example of light propagation in absorbing media in the presence of a lens	70
4.6	Paraxial light propagation in absorbing media	71
4.7	Conclusion	73
5	Characterizing the angular spectrum	75
5.1	Introduction	75
5.2	Fourier transformation and angular spectrum	77
5.3	Measurement setup	78
5.3.1	Adjusting the lens in the optical Fourier operator	79
5.3.2	Measured angular spectrum	81
5.4	Conclusion	82
6	Partially coherent mask diffraction	83
6.1	Introduction	84
6.2	Mask diffraction with a 2D light source on the focal plane of a condenser	86
6.2.1	An example of a light source with a Gaussian profile	88
6.2.2	Experimental verification	89
6.3	Generalization to polychromatic illumination sources	92
6.4	Conclusion	93
7	Optical system for phase reconstruction with phase space representations	95
7.1	Introduction	96
7.2	Definition and properties of the ambiguity function	97
7.3	Reconstruction method	100
7.3.1	Optical 1D propagator	102
7.3.2	Optical 1D Fourier-propagator	104

7.3.3	Experimental verification of 1D operators	106
7.3.4	Outline of the method and a numerical demonstration	107
7.4	Improved reconstruction method	108
7.4.1	Redundancy property of the ambiguity function	108
7.4.2	Improving the method based on redundancy properties	111
7.4.3	Residue minimization algorithm for phase elements	113
7.4.4	Experimental results	116
7.5	Conclusion	116
III	Experimental Results	119
8	Fabricating alignment structures	121
8.1	Introduction	121
8.2	Fiber resonator setup	123
8.2.1	Intrinsic losses	124
8.2.2	Losses caused by the gap	124
8.3	UV deep lithography using SU-8 photoresist	125
8.3.1	Structural requirements	125
8.3.2	Optimizing the fabrication process	126
9	Quality of SU-8 structures and resonator performance	129
9.1	Building a fiber resonator	129
9.2	Measurement results	130
9.3	Conclusion	131
10	Fabrication of micro lenses using replication techniques	133
10.1	Introduction	133
10.2	Micro cavity setup	135
10.2.1	Determining all parameters	136
10.2.2	Investigating the stability of an operating point	138
10.3	Fabricating micro lens-array using replication techniques	139
10.3.1	Thermal replication	140
10.3.2	UV replication	141
10.3.3	The entire fabrication process	143
10.4	Results	145
10.5	Conclusion	146
IV	Conclusion	149
11	Summary and perspectives	151

V	Appendix	155
A	Helpful rules for decomposing 4×4 symplectic matrices	157

Part I

Introduction

Chapter 1

Introduction and overview

Light, as a widely used signal, has many well-known advantages. Standard components are significantly smaller and lighter than components used for electrical signals. The optical signal itself has a high capacity for information. Today, based on those advantages, optical signals and components are primarily used to miniaturize complete systems and increase the speed and capacity of data flow between systems. Hence, micro and integrated optics create supporting roles in today's technological tools, including digital cameras, displays, telescopes and automobiles. Micro optics technology has opened up many new functionalities and applications that were previously unachievable [JB04]. In this study, we will outline one of these applications in atomic physics and quantum optics.

1.1 Overview - Miniaturized optics for atom detection as an application example in atomic physics

In this thesis, one project, in cooperation with the Atomchips Group at the University of Heidelberg¹, is presented as an interesting application of miniaturized optics involving deep lithography and microlens replication. In the developing field of quantum information processing, the manipulation of neutral atoms with so-called atom chips provides a new, extremely promising approach [FKS⁺02; FKC⁺00]. This concept relies on the capability of controlling magnetically trapped atoms that hover micrometers above a

¹Atomchips Group is led by Professor Jörg Schmiedmayer and has been located at the Vienna University of Technology since September 2006.

micro-structured surface that carries electric currents and charges to provide the necessary fields [LBW⁺05]. To date, integrated optical access to trapped atoms has not yet been implemented on these atom chips.

The principle for atom detection

Fig.1.1 shows one example of this type of atom chip¹. The goal of this project is to miniaturize and integrate detectors that would detect single rubidium atoms on an atom chip. Detection relies on interactions between atoms and light, i.e., the absorption interaction between light and atoms. While atoms absorb light, a light beam is significantly attenuated

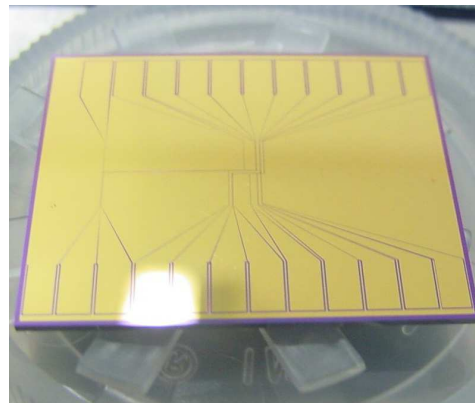


Figure 1.1: Gold, evaporated on a passive silicon substrate, constitutes the heart of a so-called atom chip.

by atoms. When applying this method, even small amounts of atoms can be easily detected. However, this method fails if only one single atom is present. In this case, the attenuation of the light beam is much too small to be measurable. To detect single atoms, the following trick may be used: placing the atom between two highly reflecting mirrors. These mirrors form an optical resonator, where light is reflected back and forth. Although the attenuation of the light beam in the presence of one atom is small between two consecutive reflections, a large effect results after many reflections. An important step is the on-chip detection of single atoms that can be achieved using an optical fiber resonator [HKH⁺03]. To place the atom inside the cavity, it is possible to cut the fiber into two pieces and place the atom in the fiber gap [Wil07]. A pair of fibers constitutes the fiber resonator, with a gap in the middle. Incoming light to the cavity comes from a piece of single-mode fiber. If the magnetically trapped atoms are located in the gap, interaction between the light and atoms causes a reduction in light exiting out of the cavity. Consequently, single atoms are detected. To complete the process, we need an easy method for mounting and aligning an optical fiber-based resonator on the flat surface of an atom chip with ultra high precision. In the first and basic approach, fibers form a Fabry-Perot type resonator (Fig. 1.2) and are mounted in a superstructure fabricated from an SU-8 resist that provides positioning and alignment accurately and

¹This image is from <http://www.physi.uni-heidelberg.de/physi/atph/atomchip2/atomchip?page=BECI1>

easily. These fibers can easily be inserted by hand and are automatically aligned with sub-micrometer precision.

To mount fibers on the atom chip, a lithographically patterned photoresist, called SU-8, is used. SU-8 is an epoxy-based, chemically amplified, solvent-developed negative resist that is typically patterned using 365-436 nm UV aligners.

Its specific properties facilitate the production of thick structures with smooth, nearly vertical sidewalls [RPF⁺]. Because of its high mechanical, chemical, and thermal stability, polymerized SU-8 is used to fabricate a wide range of micro components, including optical planar waveguides, which allows for achieves outstanding thermal stability and controllable numerical apertures; mechanical parts, such as micro gears for engineering applications; micro fluidic systems; and micro reactors for biochemical processing [RPF⁺]. In this project, the SU-8 structures are used to hold fibers. The finesse of the resonator strongly depends on losses introduced through misalignment.

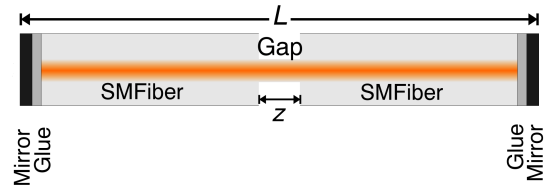


Figure 1.2: A fiber-based Fabry-Perot resonator, including a gap in the middle as the detection zone.

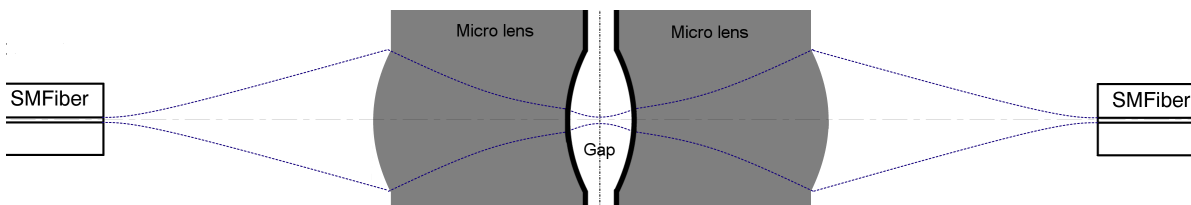


Figure 1.3: A micro confocal resonator. A pair of meniscus micro lenses is introduced. The facing concave sides are coated with a dielectric mirror and constitute a micro confocal cavity. The convex sides focus the light from the fiber so that at the location of the mirror, the wavefront of light has the same curvature radius as the mirror surface itself. By means of focusing, the light field inside the micro cavity has a small spot size; by matching the wavefront and mirror surface, the coupling efficiency of light into the cavity is also improved.

To improve the sensitivity of detection, the second approach applies a confocal cavity (Fig. 1.3). A pair of meniscus micro lenses is introduced. The facing concave sides are coated with a dielectric mirror and constitute a micro confocal cavity [Wic06]. The convex sides focus the light from the fiber so that at the location of the mirror, the wavefront of light has the same curvature radius as the mirror surface itself. By focusing, the light field inside the micro cavity has a small spot size; by matching the wavefront and

mirror surface, the coupling efficiency of light into the cavity is also improved. The small light field diameter in the detection zone can increase detection probability. However, focussing optics, i.e., micro lenses, must be integrated into the detection system. The replication technique is an easy and cost-efficient solution for fabricating meniscus micro lenses, .

Design and analysis of micro optical systems and their components

As previously mentioned, the SU-8 alignment structures are fabricated using UV-deep lithography. To analyze the deep lithographic processes, the correct and efficient modeling of light propagation is required. The second part of this study deals with some key aspects of light propagation for modeling optical deep lithography. Before beginning the discussion on scalar light propagation, a method for synthesizing optical systems is first introduced. It is implemented to solve the inverse design problem of micro optical systems. It is assumed that a desired relationship between input and output light rays is devised using an ABCD-matrix. The ultimate desired outcome is a minimal optical system consisting of only lenses and pieces of free-space propagation. Similar decompositions have been previously studied [Ars80; NS82; MA83; AM83; PB97; Cas81; SM98; AS94; Wol04; BA06], but have lacked an attempt at minimality. The main results of this chapter show that general lossless one-dimensional optical systems can be synthesized using a maximum of four elements, while two-dimensional optical systems can be synthesized using six elements at most.

For light propagation in thick resist, mask structures under consideration are large enough to ignore polarization effects. Thus, a scalar theory may be applied to simulate mask diffraction. For scalar fields, a key aspect is finding an adequate value for exposure energy. The energy flux in scalar fields is most commonly replaced by the square modulus of the scalar field, whereas the vector character of the energy flux is neglected. In Chapter 3, the validity replacing the vectorial energy flux is proven. Based on Maxwell's equations, the definition of the energy flux in scalar fields is given. This definition agrees with the Poynting vector. Various classical scalar diffraction theories are then taken into consideration. Energy flow, resulting from the correct energy flux, shows that energy conservation is held in the wave field, calculated using one of these scalar diffraction theories. However, most scalar theories do not achieve the consistency of the energy flux behind a thin optical element, due to the abrupt multiplication from

thin element approximation. One interesting and comforting fact is that all considered scalar diffraction theories apply the Fourier transformation. From Parseval's Theorem, the sum of the square modulus remains constant. In the author's opinion, this is why the energy flux is commonly calculated using the square modulus.

The next key aspect is light propagation in absorbing media. Optical lithography uses light to transform a pattern from a mask to photoresist. Photoresist is a light-sensitive material. During the lithographic process, it strongly absorbs light emitting from an aligner. However, the generally used scalar diffraction theory only supports the analysis of mask diffraction in non-absorbing media with real refractive indices. With an absorbing medium, the mathematical handling of mask diffraction requires more than merely setting the corresponding complex refractive index in the diffraction formula. Chapter 4 begins with Maxwell's equations and shows how the conventional plane wave expansion can be modified and then applied when investigating scalar mask diffraction in absorbing photoresists. Modified plane wave expansion is not the same as an inductive hypothesis, where the only thing that must be considered is setting the complex refractive index in traditional plane wave expansion. Furthermore, an approximated form allows the enhanced plane wave expansion to be reduced to a simple and efficient numerical implementation with complex calculations.

Another key aspect is the incoherent light propagation in resists. In optical lithography, a conventional way for improving exposure efficiency and illumination homogeneity is using a spatially incoherent light source. How can the image quality behind a mask be investigated? While most mask structures in presented applications are much larger than the applied wave length, applying the scalar plane wave expansion with Fresnel's approximation is sufficient for investigating the image quality behind the mask. However, the plane wave expansion with Fresnel's approximation is only applicable to coherent light sources. To solve this problem, in Chapter 6, conventional plane wave expansion with Fresnel's approximation is extended to spatial incoherent illuminating sources. To realistically model incoherent diffraction, a simple method is introduced in Chapter 5 to characterize the spatial incoherence of the illuminating source.

Chapter 7 presents a phase reconstruction method for measuring two-dimensional micro phase elements. Unlike interferometric methods, this tomographic method does not require a reference wave. Hence, it can be used to characterize light sources and wave fields. The amplitude and phase recovery of optical fields using tomographic methods

employing Wigner- or ambiguity functions have been extensively demonstrated for one-dimensional functions. For two-dimensional light distributions, the associated Wigner- or ambiguity functions are four-dimensional, posing several problems. In the same chapter, one-dimensional optical operators are presented, which allow a new concept when reconstructing arbitrary two-dimensional distributions using only the ambiguity function theory for one-dimensional functions. Here, one dimension (y) of the two-dimensional complex light source is considered at each x -position as a set of one-dimensional functions and is reconstructed using the ambiguity function. Additionally, based on the internal redundancy of the ambiguity function, the efficiency of this method is further improved. To minimize noise in measurements, a useful algorithm for phase reconstructions is introduced. At the end of this chapter, a reconstruction of a phase element, a micro lens array, is also presented.

Experimental results

The final part of this thesis deals with experimental results. Chapter 8 describes details for the alignment structures of the fiber resonator, including the design of fiber alignment structures, the loss mechanisms of the fiber resonator and the fabrication process of alignment structures. While the finesse of the resonator strongly depends on losses introduced by misalignment, the measured finesse is a suitable indicator of the quality of SU-8 alignment structures. In Chapter 9, the measured finesse indicates that the SU-8 superstructures are of high quality.

Replication technologies, such as UV-embossing, injection molding and hot embossing, become increasingly attractive for high quality production at low costs. During the second approach to atom detection, the replication technique is applied to fabricate micro meniscus lenses with one plane-convex micro lens-array as the stamp. To enable this process, two different replication techniques are used: the thermal and ultraviolet (UV) molding processes. Chapter 10 also gives complete details on the enhanced micro cavity used for atom detection, including the design of the micro cavity, replication processes and the interferometric results of the replicated micro lenses.

Part II

Design and Analysis of Micro Optical Systems and their Components

Chapter 2

Optical system design based on ray transfer matrices

The properties of first order optical systems are paraxially described through a ray transfer matrix, also called the ABCD-matrix. In a typical problem of optical analysis, one is given a sequence of optical elements and is required to find a relationship between the input and output light rays. Here, we consider the inverse problem: the synthesis of optical systems. It is assumed that a desired relationship between the input and output light rays is given through an ABCD-matrix. A minimal optical system consisting of only lenses and pieces of free space propagation is sought. Similar decompositions have been studied before [Ars80; NS82; MA83; AM83; PB97; Cas81; SM98; AS94; Wol04; BA06], but have lacked an attempt to find minimality. The main results of this chapter show that general lossless one-dimensional optical systems can be synthesized using a maximum of four elements, while two-dimensional optical systems can be synthesized using six elements at most. This design tool is helpful for minimizing an existing optical system.

2.1 Introduction

In many applications, such as system optimization or optical setups involving Gaussian beam propagation, ray transfer matrices (ABCD-matrices) that describe the relationship between paraxial entrance rays (or Gaussian beams) and exit rays (or Gaussian beams) are used as a first order approximation for system analysis. In these cases, the system is

defined and the system ABCD-matrix is calculated using elementary matrices. Matrix decomposition [Ars80; NS82; MA83; AM83; PB97; Cas81; SM98; AS94; Wol04; BA06] deals with the inverse process, where a desired system ABCD-matrix is given and the corresponding optical setup must be determined.

Several matrix decomposition methods have been used for this purpose. The LDU-decomposition [Ars80; NS82; MA83; AM83; PB97; Cas81; Wol04] is naturally suited for first-order optical systems, since the elementary operations of lens transition and propagation are naturally triangular matrices. D-matrices in this decomposition are diagonal matrices, or non-isotropic magnifiers, i.e., a different scale factor is applied to each coordinate. A modified Iwasawa-decomposition [SM98; AS94; Wol04; BA06] involving magnifiers and orthosymplectic systems has been extensively studied because of its uniqueness and mathematical properties.

In this chapter, we first present a general overview of various triangular decompositions, such as LDU-, QR-, QL-, LQ-, and RQ-decompositions, and their implementation using optical elements. From this viewpoint, the Iwasawa decomposition can be regarded as a QL- or LQ-decomposition.

During the design phase of optical systems, it is useful and practical to develop a required linear system using as few optical elements as possible. Therefore, the main focus of this chapter is to present a minimal decomposition of an arbitrary, lossless first-order optical system using only two elementary operations: lens transition (L) and propagation (P). According to [SMS85], any symplectic 4x4 matrix can be realized through a sequence of L- and P-matrices. Furthermore, restricting the decomposition of feasible optical transformations is desired. For *feasible optical*, minimal decomposition, admissible propagation operators are restricted to propagation over isotropic and positive distances. An anisotropic propagation describes the case where propagation distances in x- and y-directions are different. Although such an operator might be attainable through suitable optics, it is excluded from the list of elementary operations. This is different for anisotropic lenses, which are commonly known as astigmatic lenses and are considered here as an elementary operation. In this chapter, a method deriving the minimal decomposition for one-dimensional (1D) and two-dimensional (2D) optics is described. In addition, we demonstrate that any four-dimensional ABCD-matrix can be realized using a maximum of six optical elements.

2.2 One-dimensional optics

This section begins with the simple case: decomposition of ray transfer matrices for 1D optical systems. In paraxial optics, a light ray is characterized by its lateral position x from the optical axis (z) and by the parameter s , which is the sine of the propagation angle with respect to the optical axis. Any first order optical 1D system can be described using a real ray transformation matrix \mathbf{M} , or ABCD-matrix. Exit ray parameters are linearly dependent on entrance ray parameters, conveniently written in the following matrix form:

$$\begin{pmatrix} r_o \\ s_o \end{pmatrix} = \mathbf{M} \begin{pmatrix} r_i \\ s_i \end{pmatrix} = \begin{pmatrix} A & B \\ C & D \end{pmatrix} \begin{pmatrix} r_i \\ s_i \end{pmatrix}. \quad (2.1)$$

Since \mathbf{M} represents a linear transformation within the phase space, the phase space volume (Lagrange invariant) is preserved through this operation. Therefore, any physical transfer matrix must be symplectic, i.e., it must have a unit determinant of $|\mathbf{M}| = 1$.

The ABCD-matrix can also be used for another class of problems involving Gaussian beam propagation through paraxial optical systems. If the ABCD-matrix for the optical system is given, the relationship between the input and output Gaussian beam parameters may be obtained using the so-called ABCD law. In this case, a Gaussian beam is characterized using the $1/e$ amplitude spot radius w and the phase front curvature radius R . These quantities are combined to form a complex beam parameter q , given as,

$$\frac{1}{q} = \frac{1}{R} - \frac{i\lambda}{\pi w^2}, \quad (2.2)$$

where λ is the wavelength. If the relations of w and R for simple propagations

$$w = w_0 \sqrt{1 + \left(\frac{z}{z_0}\right)^2} \quad R = z \left[1 + \left(\frac{z}{z_0}\right)^2\right] \quad (2.3)$$

are inserted into Eq. 2.2, it is easy to see that the complex parameter q has an alternative expression:

$$q = z + iz_0. \quad (2.4)$$

Here, $z_0 = \frac{\pi w_0^2}{\lambda}$ is denoted as the Rayleigh range and w_0 as the beam waist. The positive location of waist z means that the beam waist is located before the observation point, while negative z means that the beam waist is located after the observation point. For the radius of the phase-front curvature R , the definition of its sign is analogous to the sign of the waist location: positive R means that the center of the phase-front curvature is located before the observation point and vice versa. The dependence of the input Gaussian beam q_i and the output Gaussian beam q_o is given by ABCD-matrix entries of the optical system:

$$q_o = \frac{Aq_i + B}{Cq_i + D}. \quad (2.5)$$

To use the 2×2 ABCD-matrix, Gaussian beams and optical systems in this section must be rotationally symmetric.

2.2.1 Commonly used optical components

Relevant optical components considered here are represented by the following matrices,

$$\mathbf{L}(f) = \begin{pmatrix} 1 & 0 \\ -\frac{1}{f} & 1 \end{pmatrix}, \quad \mathbf{P}(z) = \begin{pmatrix} 1 & z \\ 0 & 1 \end{pmatrix}, \quad \mathbf{S}(m) = \begin{pmatrix} m & 0 \\ 0 & \frac{1}{m} \end{pmatrix} \quad (2.6)$$

where matrix $\mathbf{L}(f)$ denotes a lens transition with the focal length f , $\mathbf{P}(z)$ denotes a propagation with a distance of z and $\mathbf{S}(m)$ is a scaling operation with a scale factor of m . In this section, light propagation is restricted to only positive z -values. This does not represent a loss of generality, since propagation distances with negative z can be realized by combining lenses and propagations with positive z . The focal length f in the lens matrix $\mathbf{L}(f)$ has a positive value for convex lenses and a negative value for those that are concave. Another useful operation concerns the generalized fractional Fourier transformation, defined as the following:

$$\mathbf{F}(m, \varphi) = \mathbf{S}(m)\Psi(\varphi) \quad (2.7)$$

$$\Psi(\varphi) = \begin{pmatrix} \cos(\varphi) & \sin(\varphi) \\ -\sin(\varphi) & \cos(\varphi) \end{pmatrix}, \quad (2.8)$$

Matrix Ψ describes a rotation in phase space. To realize the fractional Fourier transformation, one can use the setup described in [Loh93].

2.2.2 System realization using matrix decomposition

In this section, the following problem is considered: An ABCD-matrix is given, where its optical realization is sought using matrix decomposition. From linear algebra, a wide variety of methods for matrix decomposition is known. The most commonly used are LU- and QR-decompositions. Wolf and Bastiaans [Wol04; BA06] have employed the Iwasawa decomposition [SM98], consisting of rotation, scale and lens matrices. The Iwasawa decomposition is a special case of a QL- or LQ-decomposition.

Before divers matrix decomposition methods are considered, we will first describe the terminology used for different matrix types occurring in subsequent sections. The identity matrix is denoted by \mathbf{I} . The previously introduced phase space scale matrix $\mathbf{S}(m)$ has a determinant of one and is a special case of a diagonal matrix. Orthogonal matrix \mathbf{Q} satisfies the condition $\mathbf{Q}\mathbf{Q}^T = \mathbf{I}$, where \mathbf{Q}^T is the transposition of \mathbf{Q} . A rotation in phase space $\Psi(\varphi)$ is an orthogonal matrix. Another relevant type of matrix is the triangular matrix. If all entries on the diagonal of a triangular matrix are one, they are referred to as unit triangular matrices. In this notation, the lens matrix $\mathbf{L}(f)$ is a lower-left unit triangular matrix, while the propagation matrix $\mathbf{P}(z)$ is an upper-right unit triangular matrix.

Some commonly used mathematical decompositions are summarized in Table 2.1, together with corresponding optical operators. Additionally, the determinant is a multiplicative map, i.e., $|\mathbf{M}_1\mathbf{M}_2| = |\mathbf{M}_1||\mathbf{M}_2|$. Therefore, the diagonal matrix in each mathematical decomposition listed in Table 2.1 must be a scale matrix $\mathbf{S}(m)$. For the first six alternatives listed in Table 2.1, a scale matrix and rotation are required, which can be attained through a sequence of lenses and propagations.

In the following, realizations for a scale matrix and rotation in phase-space are given and are frequently used in Table 2.1. Because of the unique solution in Table 2.1, propagations with negative distances may be required. The realization of a propagation with a negative distance is listed in the following section.

Table 2.1: Various matrix decompositions using operators: lens \mathbf{L} , free space \mathbf{P} , scale \mathbf{S} and rotation $\mathbf{\Psi}$.

Decomposition of $\begin{pmatrix} A & B \\ C & D \end{pmatrix}$ in \mathbf{L} , \mathbf{P} , \mathbf{S} and $\mathbf{\Psi}$	
LDU decompn. for $A \neq 0$ *	$\mathbf{L}(-\frac{A}{C})\mathbf{S}(A)\mathbf{P}(\frac{B}{A})$
UDL decompn. for $D \neq 0$ *	$\mathbf{P}(\frac{B}{D})\mathbf{S}(\frac{1}{D})\mathbf{L}(-\frac{D}{C})$
QR decompn.	$\mathbf{\Psi}(\arctan(\frac{-C}{A}))\mathbf{S}(\sqrt{A^2 + C^2})\mathbf{P}(\frac{AB+CD}{A^2+C^2})$
QL decompn.	$\mathbf{\Psi}(\arctan(\frac{B}{D}))\mathbf{S}(\frac{1}{\sqrt{B^2+D^2}})\mathbf{L}(\frac{-B^2-D^2}{AB+CD})$
RQ decompn.	$\mathbf{P}(\frac{AC+BD}{D^2+C^2})\mathbf{S}(\frac{1}{\sqrt{D^2+C^2}})\mathbf{\Psi}(\arctan(\frac{-C}{D}))$
LQ or Iwasawa decompn.**	$\mathbf{L}(\frac{-A^2-B^2}{AC+BD})\mathbf{S}(\sqrt{A^2 + B^2})\mathbf{\Psi}(\arctan(\frac{B}{A}))$
In \mathbf{L} and \mathbf{P} for $B \neq 0$ ***	$\mathbf{L}(\frac{B}{1-D})\mathbf{P}(B)\mathbf{L}(\frac{B}{1-A})$
In \mathbf{L} and \mathbf{P} for $C \neq 0$ ***	$\mathbf{P}(\frac{A-1}{C})\mathbf{L}(-\frac{1}{C})\mathbf{P}(\frac{D-1}{C})$

*See [Ars80; NS82; MA83; AM83; PB97; Wol04]

**See [SM98; AS94; Wol04; BA06]

***See [AM83; Cas81]

Realizations of a scale matrix

If an optical system for a scale matrix is desired, its realization requires four elements in sequence: \mathbf{LPLP} or \mathbf{PLPL} ; the solutions of their parameters are not unique. In the following, some useful realizations are given. By use of Kepler-telescope, as described in equations 2.9 and 2.10, two lenses have the focal lengths of a and b .

$$\begin{aligned}
 \mathbf{S}\begin{pmatrix} b \\ -\frac{b}{a} \end{pmatrix} &= \begin{pmatrix} -\frac{b}{a} & 0 \\ 0 & -\frac{a}{b} \end{pmatrix} \\
 &= \begin{pmatrix} 1 & \frac{b(a+b)}{a} \\ 0 & 1 \end{pmatrix} \underbrace{\begin{pmatrix} 1 & 0 \\ -\frac{1}{b} & 1 \end{pmatrix} \begin{pmatrix} 1 & a+b \\ 0 & 1 \end{pmatrix} \begin{pmatrix} 1 & 0 \\ -\frac{1}{a} & 1 \end{pmatrix}}_{\text{Kepler-telescope}} \quad (2.9)
 \end{aligned}$$

$$\begin{aligned}
 &= \begin{pmatrix} 1 & 0 \\ -\frac{1}{b} & 1 \end{pmatrix} \underbrace{\begin{pmatrix} 1 & a+b \\ 0 & 1 \end{pmatrix} \begin{pmatrix} 1 & 0 \\ -\frac{1}{a} & 1 \end{pmatrix}}_{\text{Kepler-telescope}} \begin{pmatrix} 1 & \frac{(a+b)a}{b} \\ 0 & 1 \end{pmatrix} \quad (2.10)
 \end{aligned}$$

By using a space-lens-space imaging setup, as described in equations 2.11 and 2.12, the two propagations have the distances of a and b .

$$\begin{aligned} \mathbf{S} \begin{pmatrix} -\frac{b}{a} \\ a \end{pmatrix} &= \begin{pmatrix} -\frac{b}{a} & 0 \\ 0 & -\frac{a}{b} \end{pmatrix} \\ &= \underbrace{\begin{pmatrix} 1 & 0 \\ -\frac{a+b}{b^2} & 1 \end{pmatrix}}_{\text{lens}} \underbrace{\begin{pmatrix} 1 & b \\ 0 & 1 \end{pmatrix} \begin{pmatrix} 1 & 0 \\ -\frac{a+b}{ab} & 1 \end{pmatrix} \begin{pmatrix} 1 & a \\ 0 & 1 \end{pmatrix}}_{\text{b-f-g imaging setup}} \end{aligned} \quad (2.11)$$

$$= \underbrace{\begin{pmatrix} 1 & b \\ 0 & 1 \end{pmatrix} \begin{pmatrix} 1 & 0 \\ -\frac{a+b}{ab} & 1 \end{pmatrix} \begin{pmatrix} 1 & a \\ 0 & 1 \end{pmatrix}}_{\text{b-f-g imaging setup}} \underbrace{\begin{pmatrix} 1 & 0 \\ -\frac{a+b}{a^2} & 1 \end{pmatrix}}_{\text{lens}} \quad (2.12)$$

Each decomposition in equations 2.9 to 2.12 is not unique, since for a given m in $\mathbf{S}(m)$, there is a continuous range of solutions for a and b , satisfying $m = b/a$. It must be pointed out that all decompositions can be realized using positive a and b , resulting in a negative scale factor; in this case, all propagation distances are positive. A positive scale factor can be obtained by inverting detector plane coordinates.

Realizations of a phase-space rotation

In the event where an optical system for a phase-space rotation is desired, its realization requires three elements in sequence: **PLP** or **LPL**.

$$\begin{aligned} \mathbf{\Psi}(\varphi) &= \begin{pmatrix} \cos(\varphi) & \sin(\varphi) \\ -\sin(\varphi) & \cos(\varphi) \end{pmatrix} \\ &= \mathbf{L}\left(\frac{\sin(\varphi)}{1 - \cos(\varphi)}\right) \mathbf{P}(\sin(\varphi)) \mathbf{L}\left(\frac{\sin(\varphi)}{1 - \cos(\varphi)}\right) \end{aligned} \quad (2.13)$$

$$= \mathbf{P}\left(\frac{1 - \cos(\varphi)}{\sin(\varphi)}\right) \mathbf{L}\left(\frac{1}{\sin(\varphi)}\right) \mathbf{P}\left(\frac{1 - \cos(\varphi)}{\sin(\varphi)}\right) \quad (2.14)$$

It is clear that the above decompositions can exist only if $\sin(\varphi) \neq 0$. If $\sin(\varphi) = 0$, it results in the identity matrix \mathbf{I} for a null element or $-\mathbf{I}$ for inverting detector plane coordinates. On the other hand, if a propagation with a negative distance is required in the above equations, it can be realized using decomposition discussed in following.

Realizations of a propagation with a negative distance

For propagation with a negative distance, its realization requires three elements in sequence: **LPL**.

$$\begin{pmatrix} 1 & -z \\ 0 & 1 \end{pmatrix} = \Psi(\pi) \mathbf{L}\left(\frac{z}{2}\right) \mathbf{P}(z) \mathbf{L}\left(\frac{z}{2}\right) \quad (2.15)$$

Here, $\Psi(\pi)$ means that detector plane coordinates are inverted.

2.2.3 Minimal realization consisting of thin lenses and propagations

This section looks for the minimal optical realization of a given ABCD-matrix. Allowed matrices are lens $\mathbf{L}(f)$, propagation $\mathbf{P}(z)$ with only positive z , and the coordinate inversion matrix

$$\Psi(\pi) = \begin{pmatrix} -1 & 0 \\ 0 & -1 \end{pmatrix}. \quad (2.16)$$

Due to the restriction that matrix $\Psi(\pi)$ can only be at the entrance or exit side of the system, the introduction of $\Psi(\pi)$ does not increase the complexity of the optical system. Matrix $\Psi(\pi)$ is commutative with all matrices under multiplication. Thus, its position in decomposition is flexible. If it is placed at the system's exit, this operation requires a 180°-rotation of the optical detector. If this operation is placed at the system's entrance, the object plane must be rotated accordingly. The following presents an optical minimal decomposition procedure consisting of eight steps.

1. (test if $|\mathbf{M}| = 1$?) If $AD - BC \neq 1$, the given matrix is not a lossless ABCD-matrix - exit.
2. ($B > 0$?) If $B > 0$, the optical minimal decomposition consists of at most the three elements: **LPL**.

$$\begin{pmatrix} A & B > 0 \\ C & D \end{pmatrix} = \mathbf{L}(f_2) \mathbf{P}(z) \mathbf{L}(f_1) \quad (2.17)$$

$$\text{with } z = B, f_1 = \frac{B}{1-A}, f_2 = \frac{B}{1-D}$$

Note that if $A = 1$ (or/and $D = 1$), the right (or/and left) lens can be omitted. The optical (fractional) Fourier transformation (Eq.2.7) falls under this category in the case where $m \sin(\alpha) > 0$ and thus can be constructed using the sequence **LPL** with the following parameters:

$$z = m \sin(\alpha), f_1 = \frac{m \sin(\alpha)}{1 - m \cos(\alpha)}, f_2 = \frac{m \sin(\alpha)}{1 - m^{-1} \cos(\alpha)} \quad (2.18)$$

3. ($B < 0$?) If $B < 0$, the optical minimal decomposition consists of at most the three elements: **LPL**.

$$\begin{pmatrix} A & B < 0 \\ C & D \end{pmatrix} = \Psi(\pi) \mathbf{L}(f_2) \mathbf{P}(z) \mathbf{L}(f_1) \quad (2.19)$$

with $z = -B$, $f_1 = \frac{-B}{1+A}$, $f_2 = \frac{-B}{1+D}$

Note that if $A = -1$ (or $D = -1$), decomposition is further reduced. As a special example, propagation over a negative distance $-z < 0$ is constructed using the following:

$$\begin{pmatrix} 1 & -z \\ 0 & 1 \end{pmatrix} = \Psi(\pi) \mathbf{L}(f) \mathbf{P}(z) \mathbf{L}(f) \quad (2.20)$$

with $f = \frac{z}{2}$

For an optical (fractional) Fourier transform in Eq.2.7 with $m \sin(\alpha) < 0$, the transformation can also be constructed using **LPL** decomposition and a 180° -rotation of the optical detector. The parameters of **LPL** decomposition can be obtained using the following:

$$z = -m \sin(\alpha), f_1 = \frac{-m \sin(\alpha)}{1 + m \cos(\alpha)}, f_2 = \frac{-m \sin(\alpha)}{1 + m^{-1} \cos(\alpha)}. \quad (2.21)$$

4. ($B = 0$ and $A = D$?) If $B = 0$ and $A = D$, the optical minimal decomposition consists of only one lens.

$$\begin{pmatrix} 1 & 0 \\ C & 1 \end{pmatrix} = \mathbf{L}\left(-\frac{1}{C}\right) \quad (2.22)$$

$$\begin{pmatrix} -1 & 0 \\ C & -1 \end{pmatrix} = \Psi(\pi) \mathbf{L}\left(\frac{1}{C}\right) \quad (2.23)$$

5. ($B = 0$ and $A \neq D$ and $A < 0$ and $C < 0$?) If $B = 0$ and $A \neq D$ and $A < 0$ and $C < 0$, D must also be less than zero because $AD - BC = 1$. In this case, optical minimal decomposition consists of the three elements: **PLP**.

$$\begin{pmatrix} A < 0 & 0 \\ C < 0 & D < 0 \end{pmatrix} = \mathbf{P}(z_2) \mathbf{L}(f) \mathbf{P}(z_1) \quad (2.24)$$

with $f = -\frac{1}{C}$, $z_1 = \frac{D-1}{C}$, $z_2 = \frac{A-1}{C}$

6. ($B = 0$ and $A \neq D$ and $A > 0$ and $C > 0$?) If $B = 0$ and $A \neq D$ and $A > 0$ and $C > 0$, D must be greater than zero because $AD - BC = 1$. In this case, optical minimal decomposition consists of the three elements **PLP** with a 180° -rotation of the optical detector.

$$\begin{pmatrix} A > 0 & 0 \\ C > 0 & D > 0 \end{pmatrix} = \Psi(\pi) \mathbf{P}(z_2) \mathbf{L}(f) \mathbf{P}(z_1) \quad (2.25)$$

with $f = \frac{1}{C}$, $z_1 = \frac{D+1}{C}$, $z_2 = \frac{A+1}{C}$

7. ($B = 0$ and $A \neq D$ and $A < 0$ and $C \geq 0$?) If $B = 0$ and $A \neq D$ and $A < 0$ and $C \geq 0$, D must be less than zero because $AD - BC = 1$. In this case, optical minimal decomposition consists of the four elements: **LPLP** or **PLPL**. Parameters have more than one unique set of solutions. In the following, one solution is given for each **LPLP** and **PLPL** decomposition.

$$\begin{pmatrix} A < 0 & 0 \\ C & D < 0 \end{pmatrix} = \mathbf{L}(f_2) \mathbf{P}(z_2) \mathbf{L}(f_1) \mathbf{P}(z_1) \quad (2.26)$$

with $z_1 = 1$, $f_1 = \frac{A}{A-1}$, $z_2 = -A$, $f_2 = \frac{A^2}{1-A-CA}$

$$\begin{pmatrix} A < 0 & 0 \\ C & D < 0 \end{pmatrix} = \mathbf{P}(z_2) \mathbf{L}(f_2) \mathbf{P}(z_1) \mathbf{L}(f_1) \quad (2.27)$$

$$\text{with } f_1 = \frac{1}{1 - A - CA}, \quad z_1 = 1, \quad f_2 = \frac{A}{A - 1}, \quad z_2 = -A$$

Additionally, if $C = 0$, the given matrix is a scale matrix.

8. ($B = 0$ and $A \neq D$ and $A > 0$ and $C \leq 0$) If $B = 0$ and $A \neq D$ and $A > 0$ and $C \leq 0$, D must be greater than zero because $AD - BC = 1$. In this case, the optical minimal decomposition consists of the four elements: **LPLP** or **PLPL**. Parameters also have more than one unique set of solutions. In the following, one solution is given for each **LPLP** and **PLPL** decomposition.

$$\begin{pmatrix} A > 0 & 0 \\ C & D > 0 \end{pmatrix} = \Psi(\pi) \mathbf{L}(f_2) \mathbf{P}(z_2) \mathbf{L}(f_1) \mathbf{P}(z_1) \quad (2.28)$$

$$\text{with } z_1 = 1, \quad f_1 = \frac{A}{A + 1}, \quad z_2 = A, \quad f_2 = \frac{A^2}{1 + A - CA}$$

$$\begin{pmatrix} A < 0 & 0 \\ C & D < 0 \end{pmatrix} = \Psi(\pi) \mathbf{P}(z_2) \mathbf{L}(f_2) \mathbf{P}(z_1) \mathbf{L}(f_1) \quad (2.29)$$

$$\text{with } f_1 = \frac{1}{1 + A - CA}, \quad z_1 = 1, \quad f_2 = \frac{A}{A + 1}, \quad z_2 = A$$

Additionally, if $C = 0$, the given matrix is a scale matrix.

For a brief overview, all optical minimal decompositions discussed in this section are summarized in Table 2.2. Also, the decomposition of an arbitrary ray transfer matrix for 1D optical systems can be applied to rotational symmetric 2D optical systems. The next section will discuss the decomposition of ray transfer matrices for general non-symmetric 2D optical systems.

2.3 Extension to two-dimensional optics

Any two-dimensional first order optical system is described using a 4×4 ray transfer matrix \mathbf{M} acting on a four-component vector, containing the lateral position (x_i, y_i) and the direction components (sx_i, sy_i) of the light ray. Direction components are projections of the propagation vector on the lateral axis. The linear ray transformation is written

Table 2.2: An overview of the optical minimal decomposition for 1D optics. Here, the admissible matrix operators include lens-matrix \mathbf{L} , propagation-matrix \mathbf{P} with positive z and a coordinate inversion $\Psi(\pi)$.

Optical minimal decomposition for 1D optics		
$B > 0$	$A \neq 1$ and $D \neq 1$	\mathbf{LPL}
	$A = 1$ and $D \neq 1$	\mathbf{LP}
	$A \neq 1$ and $D = 1$	\mathbf{PL}
	$A = 1$ and $D = 1$	\mathbf{P}
$B < 0$	$A \neq 1$ and $D \neq 1$	$\Psi(\pi)\mathbf{LPL}$
	$A = 1$ and $D \neq 1$	$\Psi(\pi)\mathbf{LP}$
	$A \neq 1$ and $D = 1$	$\Psi(\pi)\mathbf{PL}$
	$A = 1$ and $D = 1$	$\Psi(\pi)\mathbf{P}$
$B = 0$	$A = D$ $A = 1$	\mathbf{L}
	$A = D$ $A = -1$	$\Psi(\pi)\mathbf{L}$
	$A < 0$ and $C < 0$	\mathbf{PLP}
	$A \neq D$ $A > 0$ and $C > 0$	$\Psi(\pi)\mathbf{PLP}$
	$A < 0$ and $C \geq 0$	\mathbf{LPLP} or \mathbf{LPLP}
	$A > 0$ and $C \leq 0$	$\Psi(\pi)\mathbf{LPLP}$ or $\Psi(\pi)\mathbf{PLPL}$

using the following form:

$$\begin{pmatrix} x_o \\ y_o \\ sx_o \\ sy_o \end{pmatrix} = \begin{pmatrix} \mathbf{A} & \mathbf{B} \\ \mathbf{C} & \mathbf{D} \end{pmatrix} \begin{pmatrix} x_i \\ y_i \\ sx_i \\ sy_i \end{pmatrix}; \text{ with } \mathbf{A}, \mathbf{B}, \mathbf{C}, \mathbf{D} \text{ as } 2 \times 2 \text{ matrices.} \quad (2.30)$$

Since \mathbf{M} represents a linear transformation in phase space, the phase space volume (Lagrange invariant) must be preserved using this operation. Therefore, any physical transfer matrix must be symplectic. A symplectic matrix \mathbf{M} must satisfy the following

equivalent relationships:

$$\mathbf{M}^T \begin{pmatrix} \mathbf{0} & \mathbf{I} \\ -\mathbf{I} & \mathbf{0} \end{pmatrix} \mathbf{M} = \begin{pmatrix} \mathbf{0} & \mathbf{I} \\ -\mathbf{I} & \mathbf{0} \end{pmatrix} \Rightarrow$$

$$\mathbf{A}^T \mathbf{C} = \mathbf{C}^T \mathbf{A}, \mathbf{B}^T \mathbf{D} = \mathbf{D}^T \mathbf{B}, \mathbf{A}^T \mathbf{D} - \mathbf{C}^T \mathbf{B} = \mathbf{I}; \quad (2.31)$$

$$\mathbf{M} \begin{pmatrix} \mathbf{0} & -\mathbf{I} \\ \mathbf{I} & \mathbf{0} \end{pmatrix} \mathbf{M}^T = \begin{pmatrix} \mathbf{0} & -\mathbf{I} \\ \mathbf{I} & \mathbf{0} \end{pmatrix} \Rightarrow$$

$$\mathbf{B} \mathbf{A}^T = \mathbf{A} \mathbf{B}^T, \mathbf{D} \mathbf{C}^T = \mathbf{C} \mathbf{D}^T, \mathbf{A} \mathbf{D}^T - \mathbf{B} \mathbf{C}^T = \mathbf{I}. \quad (2.32)$$

Viewing the relationships in equations 2.31 or 2.32, it is simple to derive that a 4×4 symplectic matrix has a maximum of ten independent parameters¹.

As mentioned in the previous section, one can also use ABCD-matrices to analyze the propagation of Gaussian beams through paraxial optical systems. However, this application is restricted to rotationally symmetric Gaussian beams and optical systems, or the Gaussian beams and optical systems with separable x- and y-functions. In this case, all sub-matrices \mathbf{A} , \mathbf{B} , \mathbf{C} , and \mathbf{D} must be diagonal. Cases using non-symmetric Gaussian beams are part of another research area and will not be discussed here. For more detailed information, Lin's and Cai's analysis concept of elliptical Gaussian beams using the tensor ABCD law² can be viewed.

2.3.1 Commonly used optical components

In the following, we give an overview of relevant optical operations considered in this section. The first three operations are considered as elementary operations used to realize the given ABCD-matrix.

¹See book [Wol04] chapter 9, page 164: *Number of independent symplectic parameters.*

²See "*The elliptical Hermite Gaussian beam and its propagation through paraxial systems,*" Yangjian Cai and Qiang Lin, Opt. Commun., vol. 207, pp 139–147; "*Elliptical flattened Gaussian beam analyzed by the tensor ABCD law,*" Qiang Lina and Yangjian Cai, Optik, vol. 113, pp 167–170; "*Propagation of elliptical Hermite Gaussian beam through misaligned optical system,*" Yangjian Cai and Qiang Lin, Opt. Commun., vol. 224, pp 13–19.

Elementary optical operations

- **Rotation matrix:** The first elementary matrix describes coordinate rotation on the lateral plane:

$$\mathbf{R}(\varphi) = \begin{pmatrix} \cos(\varphi) & \sin(\varphi) & 0 & 0 \\ -\sin(\varphi) & \cos(\varphi) & 0 & 0 \\ 0 & 0 & \cos(\varphi) & \sin(\varphi) \\ 0 & 0 & -\sin(\varphi) & \cos(\varphi) \end{pmatrix} \quad (2.33)$$

This rotation matrix has only one parameter φ . It is clear that rotation on the xy -plane is associated with a rotation concerning s_x and s_y by the same angle. Coordinate rotation is practically implemented by rotating the coming lateral coordinate.

- **Astigmatic lens:** The matrix for an astigmatic lens is written as

$$\mathbf{L}(f_x, f_y) = \begin{pmatrix} 1 & 0 & 0 & 0 \\ 0 & 1 & 0 & 0 \\ -\frac{1}{f_x} & 0 & 1 & 0 \\ 0 & -\frac{1}{f_y} & 0 & 1 \end{pmatrix} \quad (2.34)$$

with the two focal lengths of f_x and f_y . The definition of their signs is the same as in 1D optics, i.e., a positive value for convex lenses and a negative value for concave lenses.

- **Isotropic free space propagation:** An optical propagation in two-dimensional free space is described as

$$\mathbf{P}(z, z) = \begin{pmatrix} 1 & 0 & z & 0 \\ 0 & 1 & 0 & z \\ 0 & 0 & 1 & 0 \\ 0 & 0 & 0 & 1 \end{pmatrix} \quad (2.35)$$

where propagation distances in x- and y-directions must be equal and positive to be implemented in a real optical system.

In order to simplify the description of the decomposition method, one must introduce the following auxiliary operations, which can be expressed using the above three elementary operations, as described in the following sections.

Auxiliary operations

- **Generalized astigmatic lens:** A generalized astigmatic lens can be considered as an optical astigmatic lens, which is rotated by an angle φ around the optical axis. Such a lens can be developed by incorporating a sequence of operations $\mathbf{R}(-\varphi)\mathbf{L}(f_x, f_y)\mathbf{R}(\varphi)$, indicating that the lateral coordinate system is first rotated by an angle φ . Then, an astigmatic lens $\mathbf{L}(f_x, f_y)$ is applied. Finally, the coordinate system is rotated back, parallel to the original coordinate system:

$$\mathbf{L}^g(f_x, f_y, \varphi) = \begin{pmatrix} \mathbf{I} & \mathbf{0} \\ \mathbf{G} & \mathbf{I} \end{pmatrix} = \mathbf{R}(-\varphi)\mathbf{L}(f_x, f_y)\mathbf{R}(\varphi), \quad \mathbf{G} = \mathbf{G}^T. \quad (2.36)$$

The generalized astigmatic lens has three parameters, f_x , f_y and φ . The left bottom 2×2 sub-matrix \mathbf{G} is symmetric, which is an important feature for matrix decomposition.

- **Generalized propagation:** A generalized propagation operation is defined by the following matrix:

$$\mathbf{P}^g(z_x, z_y, \varphi) = \begin{pmatrix} \mathbf{I} & \mathbf{H} \\ \mathbf{0} & \mathbf{I} \end{pmatrix} = \mathbf{R}(-\varphi)\mathbf{P}(z_x, z_y)\mathbf{R}(\varphi), \quad (2.37)$$

$$\text{with } \mathbf{H} = \mathbf{H}^T, \quad \mathbf{P}(z_x, z_y) = \begin{pmatrix} 1 & 0 & z_x & 0 \\ 0 & 1 & 0 & z_y \\ 0 & 0 & 1 & 0 \\ 0 & 0 & 0 & 1 \end{pmatrix}$$

A generalized propagation matrix also has three parameters, z_x , z_y and φ , which can be arbitrarily positive or negative. The right top 2×2 sub-matrix \mathbf{H} , due to its construction, is symmetric. This again is an important feature for minimal decomposition.

- **Phase-space rotation:** A phase-space rotation is defined by the matrix:

$$\mathbf{\Psi}(\alpha_x, \alpha_y) = \begin{pmatrix} \cos(\alpha_x) & 0 & \sin(\alpha_x) & 0 \\ 0 & \cos(\alpha_y) & 0 & \sin(\alpha_y) \\ -\sin(\alpha_x) & 0 & \cos(\alpha_x) & 0 \\ 0 & -\sin(\alpha_y) & 0 & \cos(\alpha_y) \end{pmatrix} \quad (2.38)$$

with two parameters α_x and α_y . Interestingly, $\mathbf{\Psi}(\pi, \pi) = \mathbf{R}(\pi)$ indicates a 180°-rotation of lateral axes.

- **Generalized phase-space rotation:** A generalized phase-space rotation is defined by the matrix:

$$\mathbf{\Psi}^g(\alpha_x, \alpha_y, \varphi_1, \varphi_2) = \mathbf{R}(\varphi_2)\mathbf{\Psi}(\alpha_x, \alpha_y)\mathbf{R}(\varphi_1) \quad (2.39)$$

with four parameters α_x , α_y , φ_1 and φ_2 . This is an orthogonal matrix. The orthogonal matrix is essentially important for matrix decomposition.

- **Scaling:** A scaling operation is defined by the matrix:

$$\mathbf{S}(m_x, m_y) = \begin{pmatrix} m_x & 0 & 0 & 0 \\ 0 & m_y & 0 & 0 \\ 0 & 0 & \frac{1}{m_x} & 0 \\ 0 & 0 & 0 & \frac{1}{m_y} \end{pmatrix} \quad (2.40)$$

with two parameters m_x and m_y . A scale matrix has the form of a diagonal matrix, which is also very important for matrix decomposition.

- **Generalized scaling:** A generalized scaling is defined by the matrix:

$$\mathbf{S}^g(m_x, m_y, \varphi_1, \varphi_2) = \mathbf{R}(\varphi_2)\mathbf{S}(m_x, m_y)\mathbf{R}(\varphi_1) \quad (2.41)$$

with four parameters m_x , m_y , φ_1 and φ_2 . It is a block diagonal matrix, which is essential for block matrix decomposition.

2.3.2 System realization using matrix decomposition

This section seeks the optical realization for a given ABCD-matrix using mathematical matrix decompositions. For 2D optics, optical components in decomposition must be symplectic. Because normal triangular matrices are not symplectic, in this situation, block matrix decomposition is more suitable. From linear algebra, there is a wide variety of methods that can be used to determine block matrix decompositions. The most commonly used is the block LU- and QR-decompositions. Iwasawa decomposition [SM98; Wol04; BA06], consisting of rotation, scale and lens matrices, is a special case of QL- or LQ-decomposition. A summary of known decomposition methods for symplectic 4x4-matrices is given in Table 2.3.

The factoring of generalized components into their normal components and rotations used in Table 2.3 and the realizations of those normal forms are presented in Appendix A. Some useful rules for matrix production are also given in Appendix A. Those rules will be frequently used in the next section to discuss minimal optical realization, for example, combining two successive elements into one, transforming a sub-matrix to a symmetric or even a diagonal sub-matrix by use of rotation matrices, and so on.

2.3.3 Minimal realization consisting of thin lenses and propagations

This section looks for minimal optical realization of a given ABCD-matrix. Allowed matrices include lenses $\mathbf{L}(f_x, f_y)$, isotropic propagations $\mathbf{P}(z, z)$ with positive z , and rotation matrices \mathbf{R} . Sudarshan et al. [SMS85] have presented a proof that every symplectic 4×4 matrix can be synthesized using a finite number of anisotropic lenses \mathbf{L}^g and optical free propagations $\mathbf{P}(z, z)$ with $z > 0$. When finding the optical minimal decomposition for 2D optics, the determinant of sub-matrix \mathbf{B} must be considered and the following two cases must be determined: $|\mathbf{B}| \neq 0$ and $|\mathbf{B}| = 0$.

Case $|\mathbf{B}| \neq 0$

It is assumed that the given matrix \mathbf{M} is symplectic, i.e. $\mathbf{A}^T \mathbf{C} = \mathbf{C}^T \mathbf{A}$, $\mathbf{B}^T \mathbf{D} = \mathbf{D}^T \mathbf{B}$ and $\mathbf{A}^T \mathbf{D} - \mathbf{C}^T \mathbf{B} = \mathbf{I}$ are satisfied. In general, sub-matrix \mathbf{B} is not diagonal. For this decomposition procedure, \mathbf{B} should be diagonal. Therefore, a transformation operation

Table 2.3: Various matrix decompositions using operators, including generalized lens \mathbf{L}^g , generalized propagation \mathbf{P}^g , generalized scale \mathbf{S}^g , generalized rotation in phase-space $\mathbf{\Psi}^g$ and rotation \mathbf{R} .

Decomposition of $\begin{pmatrix} \mathbf{A} & \mathbf{B} \\ \mathbf{C} & \mathbf{D} \end{pmatrix}$ in \mathbf{L}^g , \mathbf{P}^g , \mathbf{S}^g and \mathbf{R}	
LDU decompn. for $ \mathbf{A} \neq 0$ *	$\begin{pmatrix} \mathbf{I} & \mathbf{0} \\ \mathbf{C}\mathbf{A}^{-1} & \mathbf{I} \end{pmatrix} \begin{pmatrix} \mathbf{A} & \mathbf{0} \\ \mathbf{0} & \mathbf{A}^{-1T} \end{pmatrix} \begin{pmatrix} \mathbf{I} & \mathbf{A}^{-1}\mathbf{B} \\ \mathbf{0} & \mathbf{I} \end{pmatrix} = \mathbf{L}^g \mathbf{S}^g \mathbf{P}^g$
UDL decompn. for $ \mathbf{D} \neq 0$	$\begin{pmatrix} \mathbf{I} & \mathbf{B}\mathbf{D}^{-1} \\ \mathbf{0} & \mathbf{I} \end{pmatrix} \begin{pmatrix} \mathbf{D}^{-1T} & \mathbf{0} \\ \mathbf{0} & \mathbf{D} \end{pmatrix} \begin{pmatrix} \mathbf{I} & \mathbf{0} \\ \mathbf{D}^{-1}\mathbf{C} & \mathbf{I} \end{pmatrix} = \mathbf{P}^g \mathbf{S}^g \mathbf{L}^g$
QR decompn.	$\begin{pmatrix} \mathbf{A}\mathbf{X}^{-1} & -\mathbf{C}\mathbf{X}^{-1} \\ \mathbf{C}\mathbf{X}^{-1} & \mathbf{A}\mathbf{X}^{-1} \end{pmatrix} \begin{pmatrix} \mathbf{X} & \mathbf{0} \\ \mathbf{0} & \mathbf{X}^{-1} \end{pmatrix} \begin{pmatrix} \mathbf{I} & \mathbf{X}^{-2}(\mathbf{A}^T\mathbf{B} + \mathbf{C}^T\mathbf{D}) \\ \mathbf{0} & \mathbf{I} \end{pmatrix} = \mathbf{\Psi}^g \mathbf{S}^g \mathbf{P}^g$ $\mathbf{X} = (\mathbf{A}^T\mathbf{A} + \mathbf{C}^T\mathbf{C})^{\frac{1}{2}}$
QL decompn.	$\begin{pmatrix} \mathbf{D}\mathbf{X}^{-1} & \mathbf{B}\mathbf{X}^{-1} \\ -\mathbf{B}\mathbf{X}^{-1} & \mathbf{D}\mathbf{X}^{-1} \end{pmatrix} \begin{pmatrix} \mathbf{X}^{-1} & \mathbf{0} \\ \mathbf{0} & \mathbf{X} \end{pmatrix} \begin{pmatrix} \mathbf{I} & \mathbf{0} \\ \mathbf{X}^{-2}(\mathbf{B}^T\mathbf{A} + \mathbf{D}^T\mathbf{C}) & \mathbf{I} \end{pmatrix} = \mathbf{\Psi}^g \mathbf{S}^g \mathbf{L}^g$ $\mathbf{X} = (\mathbf{B}^T\mathbf{B} + \mathbf{D}^T\mathbf{D})^{\frac{1}{2}}$
RQ decompn.	$\begin{pmatrix} \mathbf{I} & (\mathbf{A}\mathbf{C}^T + \mathbf{B}\mathbf{D}^T)\mathbf{X}^{-2} \\ \mathbf{0} & \mathbf{I} \end{pmatrix} \begin{pmatrix} \mathbf{X}^{-1} & \mathbf{0} \\ \mathbf{0} & \mathbf{X} \end{pmatrix} \begin{pmatrix} \mathbf{X}^{-1}\mathbf{D} & -\mathbf{X}^{-1}\mathbf{C} \\ \mathbf{X}^{-1}\mathbf{C} & \mathbf{X}^{-1}\mathbf{D} \end{pmatrix} = \mathbf{P}^g \mathbf{S}^g \mathbf{\Psi}^g$ $\mathbf{X} = (\mathbf{C}\mathbf{C}^T + \mathbf{D}\mathbf{D}^T)^{\frac{1}{2}}$
LQ or Iwasawa decompn. **	$\begin{pmatrix} \mathbf{I} & \mathbf{0} \\ (\mathbf{C}\mathbf{A}^T + \mathbf{D}\mathbf{B}^T)\mathbf{X}^{-2} & \mathbf{I} \end{pmatrix} \begin{pmatrix} \mathbf{X} & \mathbf{0} \\ \mathbf{0} & \mathbf{X}^{-1} \end{pmatrix} \begin{pmatrix} \mathbf{X}^{-1}\mathbf{A} & \mathbf{X}^{-1}\mathbf{B} \\ -\mathbf{X}^{-1}\mathbf{B} & \mathbf{X}^{-1}\mathbf{A} \end{pmatrix} = \mathbf{L}^g \mathbf{S}^g \mathbf{\Psi}^g$ $\mathbf{X} = (\mathbf{A}\mathbf{A}^T + \mathbf{B}\mathbf{B}^T)^{\frac{1}{2}}$
In \mathbf{L}^g and \mathbf{P}^g for $ \mathbf{B} \neq 0$	$\begin{pmatrix} \mathbf{I} & \mathbf{0} \\ (\mathbf{D}' - \mathbf{I})\mathbf{B}'^{-1} & \mathbf{I} \end{pmatrix} \begin{pmatrix} \mathbf{I} & \mathbf{B}' \\ \mathbf{0} & \mathbf{I} \end{pmatrix} \begin{pmatrix} \mathbf{B}'^{-1} & \mathbf{I} \\ \mathbf{B}'^{-1}(\mathbf{A}' - \mathbf{I}) & \mathbf{I} \end{pmatrix} \mathbf{R} = \mathbf{L}^g \mathbf{P}^g \mathbf{L}^g \mathbf{R}$ with $\begin{pmatrix} \mathbf{A} & \mathbf{B} \\ \mathbf{C} & \mathbf{D} \end{pmatrix} = \begin{pmatrix} \mathbf{A}' & \mathbf{B}' \\ \mathbf{C}' & \mathbf{D}' \end{pmatrix} \mathbf{R}$ and $\mathbf{B}'^T = \mathbf{B}'$
In \mathbf{L}^g and \mathbf{P}^g for $ \mathbf{C} \neq 0$	$\begin{pmatrix} \mathbf{I} & (\mathbf{A}' - \mathbf{I})\mathbf{C}'^{-1} \\ \mathbf{0} & \mathbf{I} \end{pmatrix} \begin{pmatrix} \mathbf{I} & \mathbf{0} \\ \mathbf{C}' & \mathbf{I} \end{pmatrix} \begin{pmatrix} \mathbf{I} & \mathbf{C}'^{-1}(\mathbf{D}' - \mathbf{I}) \\ \mathbf{0} & \mathbf{I} \end{pmatrix} \mathbf{R} = \mathbf{P}^g \mathbf{L}^g \mathbf{P}^g \mathbf{R}$ with $\begin{pmatrix} \mathbf{A} & \mathbf{B} \\ \mathbf{C} & \mathbf{D} \end{pmatrix} = \begin{pmatrix} \mathbf{A}' & \mathbf{B}' \\ \mathbf{C}' & \mathbf{D}' \end{pmatrix} \mathbf{R}$ and $\mathbf{C}'^T = \mathbf{C}'$

*See [AM83; Wol04]

**See [SM98; Wol04; BA06]

to \mathbf{M} must be applied, resulting in \mathbf{M}' with diagonal sub-matrix \mathbf{B}' :

$$\mathbf{M}' = \begin{pmatrix} \mathbf{A}' & \mathbf{B}' \\ \mathbf{C}' & \mathbf{D}' \end{pmatrix} = \mathbf{R}(\varphi_2) \cdot \begin{pmatrix} \mathbf{A} & \mathbf{B} \\ \mathbf{C} & \mathbf{D} \end{pmatrix} \cdot \mathbf{R}(\varphi_1), \quad \mathbf{B}'^T = \mathbf{B}'. \quad (2.42)$$

This transformation is described in Appendix A.6. Using this step, \mathbf{B}' is now a diagonal sub-matrix. \mathbf{M}' can be further decomposed into the following,

$$\mathbf{M}' = \mathbf{L}_2^g \mathbf{P}^g \mathbf{L}_1^g, \quad (2.43)$$

meaning that the theoretical minimal decomposition consists of two generalized lenses and one generalized propagation. In this decomposition,

$$\mathbf{L}_2^g = \begin{pmatrix} \mathbf{I} & \mathbf{0} \\ \mathbf{G}_2 & \mathbf{I} \end{pmatrix}, \quad \mathbf{G}_2 = (\mathbf{D}' - \mathbf{I})\mathbf{B}'^{-1} \quad (2.44)$$

$$\mathbf{P}^g = \begin{pmatrix} \mathbf{I} & \mathbf{B}' \\ \mathbf{0} & \mathbf{I} \end{pmatrix} \quad (2.45)$$

$$\mathbf{L}_1^g = \begin{pmatrix} \mathbf{I} & \mathbf{0} \\ \mathbf{G}_1 & \mathbf{I} \end{pmatrix}, \quad \mathbf{G}_1 = \mathbf{B}'^{-1}(\mathbf{A}' - \mathbf{I}). \quad (2.46)$$

In order to express this decomposition in terms of elementary optical operations, solutions found in Appendix A.7 and A.13 are used to obtain the following partial decompositions:

$$\mathbf{L}_2^g = \mathbf{R}_{31}^T \mathbf{L}_{31} \mathbf{R}_{31} \quad (2.47)$$

$$\mathbf{P}^g = \mathbf{R}_\pi \mathbf{L}_{21} \mathbf{P}_2 \mathbf{L}_{22} \mathbf{P}_2 \mathbf{L}_{21} \quad (2.48)$$

$$\mathbf{L}_1^g = \mathbf{R}_{11}^T \mathbf{L}_{11} \mathbf{R}_{11}. \quad (2.49)$$

Inserting equations 2.47, 2.48, and 2.49 into Eq. 2.43, matrix \mathbf{M}' can be decomposed into the following:

$$\mathbf{M}' = \mathbf{R}_{31}^T \mathbf{L}_{31} \mathbf{R}_{31} \mathbf{R}_\pi \mathbf{L}_{21} \mathbf{P}_2 \mathbf{L}_{22} \mathbf{P}_2 \mathbf{L}_{21} \mathbf{R}_{11}^T \mathbf{L}_{11} \mathbf{R}_{11}. \quad (2.50)$$

After applying $\mathbf{M} = \mathbf{R}(-\varphi_2)\mathbf{M}'\mathbf{R}(-\varphi_1)$, Appendix A.1 and A.3 can be used to combine succeeding rotation matrices into one rotation and to simplify two generalized lenses with an intermediate rotation into one generalized lens and one rotation. The complete decomposition can be summarized in the following,

$$\mathbf{M} = \mathbf{R}'_4 \mathbf{L}'_3 \mathbf{R}'_3 \mathbf{P}' \mathbf{L}'_2 \mathbf{P}' \mathbf{R}'_2 \mathbf{L}'_1 \mathbf{R}'_1, \quad (2.51)$$

which contains only elementary optical operations, with

$$\mathbf{P}' = \mathbf{P}_2 \quad (2.52)$$

$$\mathbf{L}'_2 = \mathbf{L}_{22} \quad (2.53)$$

$$\mathbf{R}'_4 \mathbf{L}'_3 \mathbf{R}'_3 = \mathbf{R}(-\varphi_2) \mathbf{R}_{31}^T \mathbf{L}_{31} \mathbf{R}_{31} \mathbf{R}_\pi \mathbf{L}_{21} \quad (2.54)$$

$$\mathbf{R}'_2 \mathbf{L}'_1 \mathbf{R}'_1 = \mathbf{L}_{21} \mathbf{R}_{11}^T \mathbf{L}_{11} \mathbf{R}_{11} \mathbf{R}(-\varphi_1). \quad (2.55)$$

The isotropic propagation \mathbf{P}' and the focal lengths of \mathbf{L}'_2 are immediately determined by the sub-decomposition of \mathbf{P}^g in Eq. 2.48. The focal lengths of \mathbf{L}'_1 and the rotation angles of \mathbf{R}'_1 and \mathbf{R}'_2 are easily determined from the matrix product on the right hand side of Eq. 2.55. If the following is denoted,

$$\mathbf{R}'_2 \mathbf{L}'_1 \mathbf{R}'_1 = \underbrace{\mathbf{L}_{21} \mathbf{R}_{11}^T \mathbf{L}_{11} \mathbf{R}_{11}}_{\text{combining as A.3}} \mathbf{R}(-\varphi_1) = \mathbf{L}_3^g \mathbf{R}(-\varphi_1) \quad (2.56)$$

$$\text{with } \mathbf{L}_3^g = \begin{pmatrix} \mathbf{I} & \mathbf{0} \\ \mathbf{U} & \mathbf{I} \end{pmatrix}, \text{ and } \mathbf{U} = \begin{pmatrix} u_{11} & u \\ u & u_{22} \end{pmatrix},$$

the relationship listed in Appendix A.7 can be used to obtain the parameters of \mathbf{L}'_1 , \mathbf{R}'_1 and \mathbf{R}'_2 :

$$\mathbf{R}'_1 = \mathbf{R}(\varphi'_1), \quad \varphi'_1 = \theta - \varphi_1 \quad (2.57)$$

$$\mathbf{R}'_2 = \mathbf{R}(\varphi'_2), \quad \varphi'_2 = -\theta \quad (2.58)$$

$$\mathbf{L}'_1 = \mathbf{L}(f_x, f_y) \quad (2.59)$$

with

$$f_x = \frac{-1}{u_{11} \cos^2 \theta + u_{22} \sin^2 \theta + u \sin(2\theta)} \quad (2.60)$$

$$f_y = \frac{-1}{u_{11} \sin^2 \theta + u_{22} \cos^2 \theta - u \sin(2\theta)} \quad (2.61)$$

$$\theta = \frac{1}{2} \arctan \left(\frac{2u}{u_{11} - u_{22}} \right). \quad (2.62)$$

Similarly, the focal lengths of \mathbf{L}'_3 and the rotation angles of \mathbf{R}'_3 and \mathbf{R}'_4 are determined from the matrix product on the right hand side of Eq. 2.54. If the following is denoted,

$$\mathbf{R}'_4 \mathbf{L}'_3 \mathbf{R}'_3 = \mathbf{R}(-\varphi_2) \underbrace{\mathbf{R}_{31}^T \mathbf{L}_{31} \mathbf{R}_{31} \mathbf{R}_\pi \mathbf{L}_{21}}_{\text{combining as A.3}} = \mathbf{R}(-\varphi_2 + \pi) \mathbf{L}_4^g \quad (2.63)$$

$$\text{with } \mathbf{L}_4^g = \begin{pmatrix} \mathbf{I} & \mathbf{0} \\ \mathbf{V} & \mathbf{I} \end{pmatrix}, \text{ and } \mathbf{V} = \begin{pmatrix} v_{11} & v \\ v & v_{22} \end{pmatrix}.$$

then the relationship listed in Appendix A.7 can be used to obtain the parameters of \mathbf{L}'_3 , \mathbf{R}'_3 and \mathbf{R}'_4 :

$$\mathbf{R}'_3 = \mathbf{R}(\varphi'_3), \quad \varphi'_3 = \theta \quad (2.64)$$

$$\mathbf{R}'_4 = \mathbf{R}(\varphi'_4), \quad \varphi'_4 = -\theta - \varphi_2 + \pi \quad (2.65)$$

$$\mathbf{L}'_3 = \mathbf{L}(f_x, f_y) \quad (2.66)$$

with

$$f_x = \frac{-1}{v_{11} \cos^2 \theta + v_{22} \sin^2 \theta + v \sin(2\theta)} \quad (2.67)$$

$$f_y = \frac{-1}{v_{11} \sin^2 \theta + v_{22} \cos^2 \theta - v \sin(2\theta)} \quad (2.68)$$

$$\theta = \frac{1}{2} \arctan \left(\frac{2v}{v_{11} - v_{22}} \right). \quad (2.69)$$

From Eq. 2.51, it is easy to see that a maximum of five optical elements (lens and propagation) are sufficient for decomposing this type of matrix. It is clear that this decomposition can be further reduced if any of the lens radii amount to infinity or if the generalized propagation in Eq. 2.43 is isotropic.

Case $|\mathbf{B}| = 0$

It is assumed that the given matrix \mathbf{M} is symplectic, but the determinant of the sub-matrix \mathbf{B} is zero, including the case where \mathbf{M} is identical to zero. For the decomposition procedure, three transformations are operated. Using the short form $\mathbf{R}_j = \mathbf{R}(\varphi_j)$, the first transformation is to convert \mathbf{B} to a diagonal \mathbf{B}' :

$$\mathbf{M}' = \mathbf{R}_2 \cdot \begin{pmatrix} \mathbf{A} & \mathbf{B} \\ \mathbf{C} & \mathbf{D} \end{pmatrix} \cdot \mathbf{R}_1. \quad (2.70)$$

The angles φ_1 and φ_2 are determined as described in Appendix A.6. After this step, \mathbf{M}' is further transformed to:

$$\mathbf{M}''' = \mathbf{R}_4 \mathbf{M}' \mathbf{P}(-z) \mathbf{R}_3 = \mathbf{R}_4 \mathbf{M}'' \mathbf{R}_3, \quad (2.71)$$

resulting in an invertible and diagonal sub-matrix \mathbf{B}''' . The angles φ_3 and φ_4 are determined from \mathbf{M}'' as described in Appendix A.6; the additional isotropic propagation

distance z is determined from \mathbf{M}' for three different cases: for $b'_{11} \neq 0$, $b'_{22} = 0$:

$$\mathbf{P}(-z) = \begin{pmatrix} \mathbf{I} & -z\mathbf{I} \\ \mathbf{0} & \mathbf{I} \end{pmatrix} \quad z > 0 \text{ arbitrary, but } z \neq \frac{b'_{11}}{a'_{11}}; \quad (2.72)$$

for $b'_{22} \neq 0$, $b'_{11} = 0$:

$$\mathbf{P}(-z) = \begin{pmatrix} \mathbf{I} & -z\mathbf{I} \\ \mathbf{0} & \mathbf{I} \end{pmatrix} \quad z > 0 \text{ arbitrary, but } z \neq \frac{b'_{22}}{a'_{22}}; \quad (2.73)$$

for $b'_{22} = b'_{11} = 0$:

$$\mathbf{P}(-z) = \begin{pmatrix} \mathbf{I} & -z\mathbf{I} \\ \mathbf{0} & \mathbf{I} \end{pmatrix} \quad z > 0 \text{ arbitrary.} \quad (2.74)$$

Similar steps as those found in Eq. 2.43 can be applied by decomposing the matrix \mathbf{M}''' :

$$\mathbf{M}''' = \mathbf{L}_2^g \mathbf{P}^g \mathbf{L}_1^g, \quad (2.75)$$

In this decomposition,

$$\mathbf{L}_2^g = \begin{pmatrix} \mathbf{I} & \mathbf{0} \\ \mathbf{G}_2 & \mathbf{I} \end{pmatrix}, \quad \mathbf{G}_2 = (\mathbf{D}''' - \mathbf{I})\mathbf{B}'''^{-1} \quad (2.76)$$

$$\mathbf{P}^g = \begin{pmatrix} \mathbf{I} & \mathbf{B}''' \\ \mathbf{0} & \mathbf{I} \end{pmatrix} \quad (2.77)$$

$$\mathbf{L}_1^g = \begin{pmatrix} \mathbf{I} & \mathbf{0} \\ \mathbf{G}_1 & \mathbf{I} \end{pmatrix}, \quad \mathbf{G}_1 = \mathbf{B}'''^{-1}(\mathbf{A}''' - \mathbf{I}). \quad (2.78)$$

In order to express this decomposition in terms of elementary optical operations, relationships in Appendix A.7 and A.13 are used to obtain partial decompositions:

$$\mathbf{L}_2^g = \mathbf{R}_{31}^T \mathbf{L}_{31} \mathbf{R}_{31} \quad (2.79)$$

$$\mathbf{P}^g = \mathbf{R}_\pi \mathbf{L}_{21} \mathbf{P}_2 \mathbf{L}_{22} \mathbf{P}_2 \mathbf{L}_{21} \quad (2.80)$$

$$\mathbf{L}_1^g = \mathbf{R}_{11}^T \mathbf{L}_{11} \mathbf{R}_{11}. \quad (2.81)$$

Inserting equations 2.79, 2.80, and 2.81 into Eq. 2.75, matrix \mathbf{M}''' can be decomposed into the following:

$$\mathbf{M}''' = \mathbf{R}_{31}^T \mathbf{L}_{31} \mathbf{R}_{31} \mathbf{R}_\pi \mathbf{L}_{21} \mathbf{P}_2 \mathbf{L}_{22} \mathbf{P}_2 \mathbf{L}_{21} \mathbf{R}_{11}^T \mathbf{L}_{11} \mathbf{R}_{11}. \quad (2.82)$$

After applying $\mathbf{M} = \mathbf{R}(-\varphi_2 - \varphi_4) \mathbf{M}''' \mathbf{P}(z) \mathbf{R}(-\varphi_1 - \varphi_3)$, Appendix A.1 and A.3 can be used to combine succeeding rotation matrices into one rotation and to simplify two generalized lenses with an intermediate rotation into one generalized lens and one rotation. The complete transformation into a decomposition of the form is simplified as

$$\mathbf{M} = \mathbf{R}'_4 \mathbf{L}'_3 \mathbf{R}'_3 \mathbf{P}' \mathbf{L}'_2 \mathbf{P}' \mathbf{R}'_2 \mathbf{L}'_1 \mathbf{R}'_1 \mathbf{P}(z). \quad (2.83)$$

containing only elementary optical operations, with

$$\mathbf{P}' = \mathbf{P}_2 \quad (2.84)$$

$$\mathbf{L}'_2 = \mathbf{L}_{22} \quad (2.85)$$

$$\mathbf{R}'_4 \mathbf{L}'_3 \mathbf{R}'_3 = \mathbf{R}(-\varphi_2 - \varphi_4) \mathbf{R}_{31}^T \mathbf{L}_{31} \mathbf{R}_{31} \mathbf{R}_\pi \mathbf{L}_{21} \quad (2.86)$$

$$\mathbf{R}'_2 \mathbf{L}'_1 \mathbf{R}'_1 = \mathbf{L}_{21} \mathbf{R}_{11}^T \mathbf{L}_{11} \mathbf{R}_{11} \mathbf{R}(-\varphi_1 - \varphi_3). \quad (2.87)$$

The isotropic propagation \mathbf{P}' and the focal lengths of \mathbf{L}'_2 are immediately determined using the sub-decomposition of \mathbf{P}^g in Eq. 2.80. The focal lengths of \mathbf{L}'_1 and the rotation angles of \mathbf{R}'_1 and \mathbf{R}'_2 are easily determined from the matrix product on the right hand side of Eq. 2.81. If the following is denoted

$$\mathbf{R}'_2 \mathbf{L}'_1 \mathbf{R}'_1 = \underbrace{\mathbf{L}_{21} \mathbf{R}_{11}^T \mathbf{L}_{11} \mathbf{R}_{11}}_{\text{combining as A.3}} \mathbf{R}(-\varphi_1 - \varphi_3) = \mathbf{L}_3^g \mathbf{R}(-\varphi_1 - \varphi_3) \quad (2.88)$$

$$\text{with } \mathbf{L}_3^g = \begin{pmatrix} \mathbf{I} & \mathbf{0} \\ \mathbf{U} & \mathbf{I} \end{pmatrix}, \text{ and } \mathbf{U} = \begin{pmatrix} u_{11} & u \\ u & u_{22} \end{pmatrix}.$$

then the relationship in Appendix A.7 can be used to obtain the parameters of \mathbf{L}'_1 , \mathbf{R}'_1 and \mathbf{R}'_2 :

$$\mathbf{R}'_1 = \mathbf{R}(\varphi'_1), \quad \varphi'_1 = \theta - \varphi_1 - \varphi_3 \quad (2.89)$$

$$\mathbf{R}'_2 = \mathbf{R}(\varphi'_2), \quad \varphi'_2 = -\theta \quad (2.90)$$

$$\mathbf{L}'_1 = \mathbf{L}(f_x, f_y) \quad (2.91)$$

$$\text{with } f_x = \frac{-1}{u_{11} \cos^2 \theta + u_{22} \sin^2 \theta + u \sin(2\theta)} \quad (2.92)$$

$$f_y = \frac{-1}{u_{11} \sin^2 \theta + u_{22} \cos^2 \theta - u \sin(2\theta)} \quad (2.93)$$

$$\theta = \frac{1}{2} \arctan \left(\frac{2u}{u_{11} - u_{22}} \right) \quad (2.94)$$

Similarly, the focal lengths of \mathbf{L}'_3 and the rotation angles of \mathbf{R}'_3 and \mathbf{R}'_4 are determined from the matrix product on the right hand side of Eq. 2.86. If we denote

$$\mathbf{R}'_4 \mathbf{L}'_3 \mathbf{R}'_3 = \mathbf{R}(-\varphi_2 - \varphi_4) \underbrace{\mathbf{R}_{31}^T \mathbf{L}_{31} \mathbf{R}_{31} \mathbf{R}_\pi \mathbf{L}_{21}}_{\text{combining as A.3}} = \mathbf{R}(-\varphi_2 - \varphi_4 + \pi) \mathbf{L}_4^g \quad (2.95)$$

$$\text{with } \mathbf{L}_4^g = \begin{pmatrix} \mathbf{I} & \mathbf{0} \\ \mathbf{V} & \mathbf{I} \end{pmatrix}, \text{ and } \mathbf{V} = \begin{pmatrix} v_{11} & v \\ v & v_{22} \end{pmatrix},$$

the relationship in Appendix A.7 can be used to obtain the parameters of \mathbf{L}'_3 , \mathbf{R}'_3 and \mathbf{R}'_4 :

$$\mathbf{R}'_3 = \mathbf{R}(\varphi'_3), \quad \varphi'_3 = \theta \quad (2.96)$$

$$\mathbf{R}'_4 = \mathbf{R}(\varphi'_4), \quad \varphi'_4 = -\theta - \varphi_2 - \varphi_4 + \pi \quad (2.97)$$

$$\mathbf{L}'_3 = \mathbf{L}(f_x, f_y) \quad (2.98)$$

$$\text{with } f_x = \frac{-1}{v_{11} \cos^2 \theta + v_{22} \sin^2 \theta + v \sin(2\theta)} \quad (2.99)$$

$$f_y = \frac{-1}{v_{11} \sin^2 \theta + v_{22} \cos^2 \theta - v \sin(2\theta)} \quad (2.100)$$

$$\theta = \frac{1}{2} \arctan \left(\frac{2v}{v_{11} - v_{22}} \right) \quad (2.101)$$

From Eq. 2.83, it can be determined that a maximum of six optical elements (lens and propagation) are sufficient for decomposing this type of matrix. It is clear that this decomposition can be further reduced if any of the lens radii in this decomposition amount to infinity or if the generalized propagation in Eq. 2.75 is isotropic.

2.4 Conclusion

This chapter has presented a method for decomposing an arbitrary, lossless first-order optical system described by a ray-transfer matrix using only feasible optical operations. The considered elementary operations include lens transition, isotropic propagation over

positive distances and coordinate rotation. The described method provides decomposition with as few elements as possible. In this chapter, it has been found that a general lossless 1D-optical system can be synthesized using a maximum of four optical elements, while a general lossless 2D-optical system can be synthesized using a maximum of six optical elements.

Chapter 3

Investigating energy flow in scalar wave fields

While considered mask structures for the alignment structures are large enough to allow one to ignore polarization effects, succeeding chapters apply only scalar theories to estimate the light propagation in photoresists. For modeling the exposure process, the energy flow in photoresist must be determined. A review of literature dictates that the energy flux in scalar fields is commonly replaced by the square modulus, whereas, the vector character of the energy flux is neglected. In this chapter, the validity of replacing the vectorial energy flux using the square modulus is proven. It begins with the ideas of Born and Wolf [BW99], based on Maxwell's equations. From this, we conclude that the energy flux in scalar fields is a product of the complex conjugate of scalar fields and its divergence. The definition of energy flux is verified by comparing it with the Poynting-vector and the square modulus in two special cases, i.e., the standing wave and the interference of two plane waves. This comparison shows that the definition of energy flux given by Born and Wolf [BW99] agrees with the Poynting-vector, while the square modulus does not. Various classical scalar diffraction theories are then taken into consideration. The energy flow resulting from the Born and Wolf's definition shows that energy conservation is held in the half space (typically $z > 0$) at the right of the interface plane ($z = 0$). However, the energy flow does not remain continuous at $z = 0$, due to the abrupt multiplication of thin element approximation. One interesting and comforting fact is that by viewing Parseval's theorem, the square modulus of scalar fields remains continuous. This may be why the energy flux is commonly calculated using the

square modulus when one of the mentioned scalar theories is applied, rather than Born and Wolf's definition.

3.1 Introduction and motivation

The electromagnetic wave is represented by two vectors: the complex electric vector \mathbf{E} and the complex magnetic vector \mathbf{H} . If both vectors are known, the amount of energy crossing a unit area per second normal to the direction of \mathbf{E} and \mathbf{H} is represented by the real Poynting-vector $\mathbf{S} = \Re \{\mathbf{E} \times \mathbf{H}^*\}$. Since optical waves have high frequency, in order of $10^{15} s^{-1}$, one cannot observe instantaneous values of rapidly oscillating quantities, only the time-averaged quantities taken over a time interval. The time-averaged Poynting-vector is given in Eq.3.1. From it, the averaged total flux of energy (more precisely, the flux of power) through any surface can be obtained using the integral in outlined in Eq.3.2. The direction of $d\mathbf{A}$ is its normal vector. Generally, the power flow in the optical axis is the chief point of interest. \mathbf{A} is then the xy -plane, sometimes part of xy -plane, i.e., the core of an optical fiber.

$$\langle \mathbf{S} \rangle = \frac{1}{2} \Re \{ \mathbf{E}(\mathbf{r}, t) \times \mathbf{H}^*(\mathbf{r}, t) \} \quad (3.1)$$

$$P = \int_A \langle \mathbf{S} \rangle \cdot d\mathbf{A} \quad (3.2)$$

The length of the average Poynting-vector is designated by the intensity of the electromagnetic wave:

$$I = |\langle \mathbf{S} \rangle|. \quad (3.3)$$

For a plane wave, the intensity can also be obtained by applying the following equation:

$$I = |\langle \mathbf{S} \rangle| = \frac{1}{2} \sqrt{\frac{\epsilon \epsilon_0}{\mu \mu_0}} |\mathbf{E}|^2. \quad (3.4)$$

Since the directions of the Poynting-vector and the surface normal are not identical everywhere, for example, in Fig.3.1, $I dA$ and $\mathbf{S} \cdot d\mathbf{A}$ can also give different values. Hence, for the correct estimation of an energy flow, the vectorial character of the Poynting-vector is of importance.

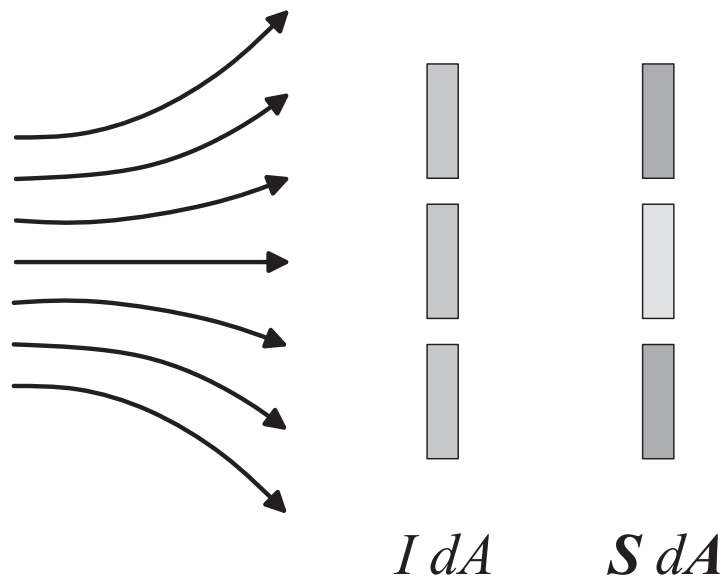


Figure 3.1: Due to the fact that $I dA \neq \mathbf{S} \cdot d\mathbf{A}$, the vectorial character of the Poynting-vector is important when calculating the power flow through a surface.

Viewing the paraxial case, the inclination of a local ray to the optical axis is so small that the $\cos \theta$ from the $\mathbf{S} \cdot d\mathbf{A} = I dA \cos \theta$ can be approximated as $\cos \theta \approx 1$. The flux of power can then be calculated using $I dA$.

Using non-paraxial scalar theories, including the Kirchhoff diffraction theory, Debye integral or the plane wave expansion, the inclination of a local ray towards the optical axis can be up to 90 degrees. Clearly, in this case, one must determine the vectorial energy flux before calculating the power flow through a surface. The sought vector should correspond with the Poynting-vector in vectorial electromagnetic fields. However, a review of literature indicates that no intensive discussion how to calculate the energy flux from a scalar field $u(\mathbf{r}, t)$ have been conducted. In addition, energy is handled simply by using the square of the modulus, $|u|^2$. The square modulus will be discussed in a later section. The determined conclusion is that the square modulus is not always correct for calculating energy flow.

To determine the correct formula for finding the energy flux of a scalar field, one appendix from *Principles of Optics* by Born and Wolf is addressed. Additionally, this derivation is extended to a definition of energy flux in media with complex refractive indices.

3.2 Scalar field flux according to Born/Wolf

The content for this short section can be found in Appendix XI of *Principles of Optics* by Born and Wolf. To give a comprehensive description of the following sections, the derivation of Born/Wolf is briefly repeated. $R(\mathbf{r}, t)$ is a real field in a sources-free region. It satisfies the wave equation

$$\nabla^2 R(\mathbf{r}, t) - \frac{n^2}{c^2} \ddot{R}(\mathbf{r}, t) = 0, \quad (3.5)$$

with n the real refractive index. Multiplying this equation by $\partial R/\partial t$ gives the following equation

$$\dot{R}(\mathbf{r}, t) \left\{ \nabla^2 R(\mathbf{r}, t) - \frac{n^2}{c^2} \ddot{R}(\mathbf{r}, t) \right\} = 0. \quad (3.6)$$

If elementary differential calculus is applied, the above equation implies the following

$$\nabla \mathbf{F}(\mathbf{r}, t) + \dot{W}(\mathbf{r}, t) = 0, \quad (3.7)$$

where

$$\mathbf{F}(\mathbf{r}, t) = -\dot{R} \nabla R, \quad (3.8)$$

$$W(\mathbf{r}, t) = \frac{1}{2} \left[\frac{n^2}{c^2} \dot{R}^2 + (\nabla R)^2 \right]. \quad (3.9)$$

The form of Eq.3.7 is a continuity equation and suggests that the scalar quantity $W(\mathbf{r}, t)$ may be regarded as energy density, with the vector quantity $\mathbf{F}(\mathbf{r}, t)$ as the energy flux vector of the field. If Eq.3.7 is integrated throughout any finite domain V bounded by a closed surface A , using Gauss's theorem, the following formula is obtained:

$$\oint\!\!\!\oint_A \mathbf{F}(\mathbf{r}, t) \cdot d\mathbf{A} = -\frac{d}{dt} \iiint_V W(\mathbf{r}, t) dV. \quad (3.10)$$

The left-hand side of Eq.3.10 may be interpreted as representing the rate at which energy leaves volume V through boundary surface A . The right-hand side may be interpreted as the rate at which energy contained in volume V decreases. Thus, Eq.3.10 expresses the law of conservation of energy in a (real) scalar wave field, $R(\mathbf{r}, t)$. And in a medium

with the real refractive index n . Eq.3.7 may be regarded as the differential form of this law.

3.3 Generalizing the energy flux for media with complex refractive indices

The absorption of photoresist causes energy loss. In the area of optical research, absorbing media can be described using complex refractive indices. This section discusses the energy conservation law for media with complex refractive indices. This approach is in principle similar to the Born/Wolf approach. It begins with a complex field allowing the complex refractive index to be directly used in the wave equation.

A complex scalar field $\phi(\mathbf{r}, t)$ satisfies the wave equation

$$\nabla^2 \phi(\mathbf{r}, t) - \frac{\hat{n}^2}{c^2} \ddot{\phi}(\mathbf{r}, t) = 0, \quad (3.11)$$

where $\hat{n} = n + i\kappa$ is the complex refractive index. Obviously, the complex conjugate of the above equation must also be valid:

$$\nabla^2 \phi^*(\mathbf{r}, t) - \frac{\hat{n}^{*2}}{c^2} \ddot{\phi}^*(\mathbf{r}, t) = 0. \quad (3.12)$$

In this case, to constitute a real field from a complex field, Eq.3.11 is multiplied with the complex conjugate of $\partial\phi/\partial t$, while Eq.3.12 with $\partial\phi/\partial t$. Finally, the sum of both multiplications is derived, which yields the following:

$$\dot{\phi}^* \left(\nabla^2 \phi - \frac{\hat{n}^2}{c^2} \ddot{\phi} \right) + \dot{\phi} \left(\nabla^2 \phi^* - \frac{\hat{n}^{*2}}{c^2} \ddot{\phi}^* \right) = 0 \quad (3.13)$$

$$\dot{\phi}^* \nabla^2 \phi + \dot{\phi} \nabla^2 \phi^* - \dot{\phi}^* \frac{\hat{n}^2}{c^2} \ddot{\phi} - \dot{\phi} \frac{\hat{n}^{*2}}{c^2} \ddot{\phi}^* = 0. \quad (3.14)$$

By using the chain rule of derivative in the above equation, the following can be obtained:

$$\begin{aligned} & \nabla(\dot{\phi}^* \nabla \phi) - \nabla \dot{\phi}^* \nabla \phi + \nabla(\dot{\phi} \nabla \phi^*) - \nabla \dot{\phi} \nabla \phi^* \\ & - \frac{n^2 - \kappa^2}{c^2} \frac{\partial}{\partial t} (\dot{\phi}^* \dot{\phi}) - \frac{2i n \kappa}{c^2} (\dot{\phi}^* \ddot{\phi} - \dot{\phi} \ddot{\phi}^*) = 0 \end{aligned}$$

$$\nabla \underbrace{(\dot{\phi}^* \nabla \phi + \dot{\phi} \nabla \phi^*)}_{\text{energy flux } \mathbf{F}} = \frac{\partial}{\partial t} \underbrace{\left(|\nabla \phi|^2 + \frac{n^2 - \kappa^2}{c^2} |\dot{\phi}|^2 \right)}_{\text{energy density } \dot{W}} + \underbrace{\frac{2in\kappa}{c^2} (\dot{\phi}^* \ddot{\phi} - \dot{\phi} \ddot{\phi}^*)}_{\text{absorption } \dot{W}_A}, \quad (3.15)$$

where the energy flux

$$\mathbf{F} = -(\dot{\phi}^* \nabla \phi + \dot{\phi} \nabla \phi^*), \quad (3.16)$$

the energy density

$$W = |\nabla \phi|^2 + \frac{n^2 - \kappa^2}{c^2} |\dot{\phi}|^2, \quad (3.17)$$

and the time-based derivative of the absorbed energy

$$\dot{W}_A = \frac{2in\kappa}{c^2} (\dot{\phi}^* \ddot{\phi} - \dot{\phi} \ddot{\phi}^*) \quad (3.18)$$

are absolute real functions. When the field is monochromatic, $\phi(\mathbf{r}, t)$ can be separated into a function $u(\mathbf{r}, \omega)$ which depends only on \mathbf{r} and an exponential function, which depends only on t :

$$\phi(\mathbf{r}, t) = u(\mathbf{r}, \omega) e^{-i\omega t}. \quad (3.19)$$

After inserting Eq. 3.19 into Eq. 3.15, the differential form of the energy conservation law can be specialized as

$$\nabla \underbrace{\left(\frac{\omega}{2} \Im(u^* \nabla u) \right)}_{\mathbf{F}} = -\frac{\partial}{\partial t} \underbrace{\left(\frac{1}{4} |\nabla u|^2 + \frac{1}{4} (n^2 - \kappa^2) k_0^2 |u|^2 \right)}_{W \text{ is not dependent on time}} - \underbrace{n\kappa k_0^2 \omega |u|^2}_{\dot{W}_A}, \quad (3.20)$$

where \Im denotes the imaginary part and k_0 is the wave number for the vacuum. The energy flux, energy density and the time-based derivative of absorbed energy are now related to u :

$$\mathbf{F} = \left(\frac{\omega}{2} \Im(u^* \nabla u) \right) \quad (3.21)$$

$$W = \left(\frac{1}{4} |\nabla u|^2 + \frac{1}{4} (n^2 - \kappa^2) k_0^2 |u|^2 \right) \quad (3.22)$$

$$\dot{W}_A = n\kappa k_0^2 \omega |u|^2. \quad (3.23)$$

Eq. 3.23 shows that local absorbed energy in the photoresist is proportional to the modulus square of field amplitude, $|u|^2$. Since energy density W depends only on u , which does not depend on time t , obviously, $\frac{\partial}{\partial t}W$ results in zero. The differential form of energy conservation can then be written in terms of \mathbf{F} and \dot{W}_A :

$$\nabla \mathbf{F} = -\dot{W}_A. \quad (3.24)$$

If we integrate this equation throughout any finite domain V bounded by a closed surface A and use Gauss' theorem, the corresponding integral form is obtained:

$$\begin{aligned} \oiint_A \mathbf{F}(\mathbf{r}, t) \cdot d\mathbf{A} &= - \iiint_V \dot{W}_A dV \\ &= - \iiint_V n\kappa k_0^2 \omega |u|^2 dV. \end{aligned} \quad (3.25)$$

The left-hand side of the equation can be interpreted as energy leaving volume V through boundary surface A . The right-hand side can be interpreted as absorbed energy in volume V . Thus, Eq.3.25 offers an alternative analysis of the absorption or gain in the given medium. It is observed that if $n\kappa \neq 0$, there is a loss (or gain) of energy in the photoresist. If n or κ is zero, the last integral in Eq.3.25 vanishes. In this case, the divergence of the energy flux is zero, i.e., in observed media, energy remains constant:

$$\oiint_A \mathbf{F}(\mathbf{r}, t) \cdot d\mathbf{A} = 0 \quad \text{if } \kappa = 0. \quad (3.26)$$

3.4 Two examples comparing energy flux, the Poynting-vector and $|u|^2$

To demonstrate that the \mathbf{F} -vector is an adequate parameter for calculating the energy flow in scalar fields, this section will provide two simple examples. The \mathbf{F} -vector in scalar fields will be compared with the Poynting-vector from vectorial fields. Due to the fact that the square of the modulus $|u|^2$ is often used to calculate energy flow, the \mathbf{F} -vector will also be compared with $|u|^2$. In both examples, the considered waves are

monochromatic.

3.4.1 Standing wave

The first example considers a standing wave, created by two plane waves with the same amplitudes but opposite directions of propagation. To ensure the comparison between scalar and vector fields, polarizations are generally specified using variables ϕ_1 and ϕ_2 (Fig.3.2). In the case of $\phi_1 = \phi_2$, the \mathbf{H} -fields from two single plane waves have opposite polarizations; therefore, they compensate each other. In this special case, the Poynting-vector is certainly zero. The next subsection will show that the Poynting-vector is zero for all polarizations, and not just for this particular case.

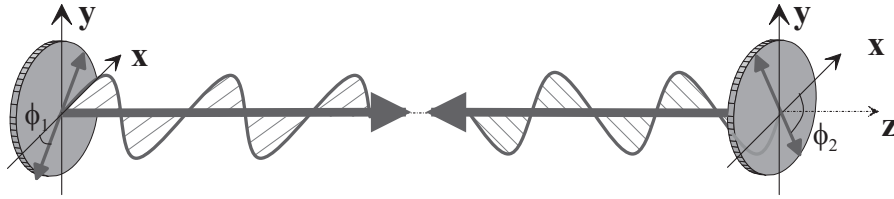


Figure 3.2: *The standing wave from two plane waves with the same amplitudes, but opposite directions of propagation: ϕ_1 and ϕ_2 are the angles between oscillation directions of the \mathbf{E} -fields and x -axis.*

The Poynting-vector in the vectorial theory

As shown in Fig.3.2, the vectorial \mathbf{E} -field of a standing wave created by two plane waves with the same amplitudes but opposite directions of propagation can be written as the following:

$$\mathbf{E}(x, y, z) = \begin{pmatrix} \cos(\phi_1) \\ \sin(\phi_1) \\ 0 \end{pmatrix} e^{ikz} + \begin{pmatrix} \cos(\phi_2) \\ \sin(\phi_2) \\ 0 \end{pmatrix} e^{-ikz}. \quad (3.27)$$

From Maxwell's equations, the \mathbf{H} -field can be obtained from the \mathbf{E} -field, as shown in the following:

$$\mathbf{H}(x, y, z) = \frac{1}{\mu_0 \mu_i \omega} \nabla \times \mathbf{E}(x, y, z)$$

$$= \frac{n}{\mu_0 \mu c} \left\{ \begin{pmatrix} -\sin(\phi_1) \\ \cos(\phi_1) \\ 0 \end{pmatrix} e^{ikz} + \begin{pmatrix} \sin(\phi_2) \\ -\cos(\phi_2) \\ 0 \end{pmatrix} e^{-ikz} \right\} \quad (3.28)$$

When both \mathbf{H} - and \mathbf{E} -fields are inserted into the Poynting-vector, the following is obtained:

$$\begin{aligned} \langle \mathbf{S}(x, y, z) \rangle &= \frac{1}{2} \Re \{ \mathbf{E}(x, y, z) \times \mathbf{H}^*(x, y, z) \} \\ &= \frac{n}{\mu_0 \mu c} \Re \left\{ \begin{pmatrix} 0 \\ 0 \\ \cos(\phi_1 - \phi_2) \end{pmatrix} i \sin(2kz) \right\} \\ &= 0. \end{aligned} \quad (3.29)$$

This results in a zero value for arbitrary polarizations. This result is obvious in a physical sense: since the amount of energy which flows in the positive z -direction is equal to the amount of energy flowing in the negative z -direction, the net flow is zero.

F-vector in scalar theory

Ignoring polarization effects, the scalar field of a standing wave created by two plane waves with the same amplitudes but opposite directions of propagation can be written as:

$$u(x, y, z) = e^{ik_z z} + e^{-ik_z z}. \quad (3.30)$$

By inserting u in the \mathbf{F} -vector (3.21), zero is obtained:

$$\begin{aligned} \mathbf{F}(x, y, z) &= \frac{\omega}{2} \Im \{ u^*(x, y, z) \nabla u(x, y, z) \} \\ &= \frac{\omega}{2} \Im \left\{ - \begin{pmatrix} 0 \\ 0 \\ 1 \end{pmatrix} 2k \sin(2kz) \right\} \\ &= 0 \end{aligned} \quad (3.31)$$

Therefore, in the case of a standing wave, there is an agreement between the Poynting- and \mathbf{F} -vectors.

$|u|^2$ in scalar theory

The square modulus from the given scalar standing wave is calculated as the following:

$$|u(x, y, z)|^2 = 4 \cos^2(kz). \quad (3.32)$$

The square of the modulus is not zero. This indicates that the square modulus of scalar fields is not an appropriate value for calculating energy flux, even though the square of the modulus is often used as the local magnitude for determining energy flow per time and volume.

3.4.2 Interference of two plane waves

This second example considers interference created by two plane waves with the same amplitudes, where their propagation directions form an angle with respect to the z -axis (Fig.3.3). To ensure a comparison between scalar and vector fields, the polarizations of the \mathbf{E} -field are in y -direction.

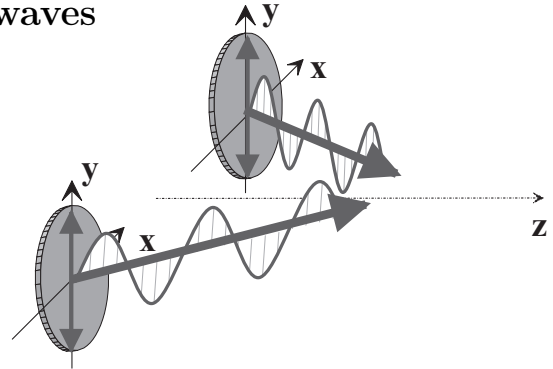


Figure 3.3: Two plane waves interfering with each other.

The Poynting-vector in vectorial theory

As shown in Fig.3.3, the vectorial \mathbf{E} -field of this interference created by two plane waves can be written as the following:

$$\mathbf{E}(x, y, z) = \begin{pmatrix} 0 \\ 1 \\ 0 \end{pmatrix} e^{ik_x x + ik_z z} + \begin{pmatrix} 0 \\ 1 \\ 0 \end{pmatrix} e^{-ik_x x + ik_z z} \quad (3.33)$$

Substituting the \mathbf{E} -field in Maxwell's equations, the following vectorial \mathbf{H} -field is obtained:

$$\begin{aligned}\mathbf{H}(x, y, z) &= \frac{1}{\mu_0 \mu i \omega} \nabla \times \mathbf{E}(x, y, z) \\ &= \frac{1}{\mu_0 \mu \omega} \left[\begin{pmatrix} -k_z \\ 0 \\ k_x \end{pmatrix} e^{ik_x x + ik_z z} + \begin{pmatrix} -k_z \\ 0 \\ -k_x \end{pmatrix} e^{-ik_x x + ik_z z} \right].\end{aligned}\quad (3.34)$$

As both \mathbf{E} and \mathbf{H} fields are available, the Poynting-vector can be calculated as:

$$\begin{aligned}\langle \mathbf{S}(x, y, z) \rangle &= \frac{1}{2} \Re \{ \mathbf{E}(x, y, z) \times \mathbf{H}^*(x, y, z) \} \\ &= \frac{2k_z \cos^2(k_x x)}{\mu_0 \mu \omega} \begin{pmatrix} 0 \\ 0 \\ 1 \end{pmatrix}.\end{aligned}\quad (3.35)$$

The above equation indicates that the Poynting-vector depends on k_z . This means that the larger the off-axis angle of the propagation direction to the z -axis, the less the magnitude of the Poynting-vector. This is due to the fact that more energy flows in the x -direction. Energy flowing in the x -direction will be completely equated because the two plane waves have opposite k_x .

F-vector in scalar theory

The scalar field for interference created by two plane waves can be written as:

$$u(x, y, z) = e^{ik_x x + ik_z z} + e^{-ik_x x + ik_z z}.\quad (3.36)$$

Substituting u in the \mathbf{F} -vector shows its dependence on k_z .

$$\begin{aligned}\mathbf{F}(x, y, z) &= \frac{\omega}{2} \Im \{ u^*(x, y, z) \nabla u(x, y, z) \} \\ &= 2\omega k_z \cos(k_x x) \begin{pmatrix} 0 \\ 0 \\ 1 \end{pmatrix}\end{aligned}$$

In the case of interference for two plane waves, an agreement also exists between the Poynting- and \mathbf{F} -vectors, except for absolute constants such as ω , μ_0 , and μ .

$|u|^2$ in scalar theory

The square modulus from the given scalar interference is calculated as the following:

$$|u(x, y, z)|^2 = 4 \cos^2(k_x x) \quad (3.37)$$

The square of the modulus has no dependence on k_z . This again indicates that the square modulus for scalar fields is not an appropriate value for calculating energy flux.

3.4.3 Summary and conclusion

This section summarizes all \mathbf{S} , \mathbf{F} and $|u|^2$ in the two examples shown in Table 3.1. Both examples show that the \mathbf{F} -vector agrees with the Poynting-vector. Moreover, it means that the \mathbf{F} -vector is an adequate value for calculating energy flow in scalar fields. Although the square of the modulus is often used to determine energy flow per time and per volume, the two examples show that it is not proportional to the magnitude of the Poynting-vector. Therefore, it is incorrect to calculate energy flow using $|u|^2$.

Table 3.1: Comparison of the \mathbf{F} -vector, Poynting-vector, and intensity from the square of the modulus.

	$\langle \mathbf{S} \rangle = \frac{1}{2} \Re \{ \mathbf{E} \times \mathbf{H}^* \}$	$\mathbf{F} = \frac{\omega}{2} \Im \{ u^* \nabla u \}$	$I = u ^2$
Standing wave	0	0	$4 \cos^2(kz)$
Interference	$\frac{2k_z \cos^2(k_x x)}{\mu_0 \mu \omega} \mathbf{e}_z$	$2\omega k_z \cos(k_x x) \mathbf{e}_z$	$4 \cos^2(k_x x)$
Summary		$\mathbf{F} \propto \langle \mathbf{S} \rangle$	$ u ^2 \not\propto \langle \mathbf{S} \rangle$

3.5 Energy conservation in various scalar theories

In this section, energy conservation will be checked for various scalar theories. It begins with a simple case involving only one plane wave, followed by scalar light propagation using the plane wave expansion, Rayleigh-Sommerfeld diffraction, Kirchhoff diffraction, and Debye scalar diffraction. For a plane at $z = 0$, the wave field or its derivative in z -direction is supposedly given. From this, distribution in the half space $z > 0$ can

be calculated. Observations of energy conservation concentrate on the energy flow in z -direction in the region of $z > 0$.

3.5.1 Single plane wave

For a single plane wave,

$$u(\mathbf{r}) = u_0 e^{i\mathbf{k}\cdot\mathbf{r}}, \quad (3.38)$$

energy flux flows in the same direction as k -direction, or the direction of propagation:

$$\begin{aligned} \mathbf{F}(\mathbf{r}) &= \frac{\omega}{2} \Im \{ u^*(\mathbf{r}) \nabla u(\mathbf{r}) \} \\ &= \frac{\omega}{2} \Im \{ u_0^* e^{-i\mathbf{k}\cdot\mathbf{r}} \cdot u_0 \cdot i\mathbf{k} e^{i\mathbf{k}\cdot\mathbf{r}} \} \\ &= \frac{\omega}{2} \mathbf{k} |u_0|^2. \end{aligned} \quad (3.39)$$

Its length is constant and proportional to the frequency, wave number and square modulus of the plane wave. Energy flow in z direction can be written as

$$P_z(z) = \iint_{-\infty}^{+\infty} \mathbf{F}(x, y, z) \cdot \mathbf{e}_z dx dy = \frac{\omega}{2} |u_0|^2 \mathbf{k} \cdot \mathbf{e}_z = \frac{\omega}{2} |u_0|^2 k \cos \vartheta, \quad (3.40)$$

with ϑ as the angle between the direction of the \mathbf{k} -vector and the z -axis. In $P_z(z)$, the subscript z indicates energy flowing in the z -direction; the input parameter z in parentheses indicates the z -position.

3.5.2 Plane wave expansion based on the continuity of u

If a complex field distribution at $z = 0$ is known as $u(x, y, 0)$, its various spatial Fourier components can be identified as plane waves traveling in different directions away from that plane. The propagation of $u(x, y, 0)$ from the plane $z = 0$ to a parallel plane at nonzero distance $z > 0$ can be calculated by adding the contributions of these plane waves and taking into account phase shifts during propagation [Goo96]. Light propaga-

tion in a medium with a real refractive index is considered in the following equation:

$$\begin{aligned}
\tilde{u}(k_x, k_y, 0) &= \iint_{-\infty}^{+\infty} u(x, y, 0) \cdot e^{-i(k_x x + k_y y)} dx dy \\
u_I(x, y, z > 0) &= \iint_{-\infty}^{+\infty} \tilde{u}(k_x, k_y, 0) \cdot e^{i(k_x x + k_y y)} e^{i z k_z} \frac{dk_x dk_y}{(2\pi)^2} \\
\text{with } k_z &= \sqrt{n^2 k_0^2 - k_x^2 - k_y^2}.
\end{aligned} \tag{3.41}$$

Here, this plane wave expansion from $u(x, y, 0)$ is called PWEL, or the first diffraction formula of plane wave expansion [Sta86, Chapter 4.1.1].

A statement concerning how much energy flows through a lateral plane at $z > 0$ will now be given:

$$\begin{aligned}
P_z(z > 0) &= \iint_{-\infty}^{+\infty} \mathbf{F}(x, y, z) \cdot \mathbf{e}_z dx dy = \frac{\omega}{2} \Im \left\{ \iint_{-\infty}^{+\infty} u_I^*(x, y, z) \frac{\partial u_I(x, y, z)}{\partial z} dx dy \right\} \\
&= \frac{\omega}{2} \iint_{-\infty}^{+\infty} |\tilde{u}(k_x, k_y, 0)|^2 \cdot k_z \frac{dk_x dk_y}{(2\pi)^2}
\end{aligned} \tag{3.42}$$

This equation can be readily understood if each plane wave is observed. Each plane wave has a contribution, depending on its intensity of $|\tilde{u}(k_x, k_y, 0)|^2$ and the z component of its wave number, k_z . $P_z(z > 0)$ does not depend on the z location. This fact indicates that plane wave expansion satisfies energy conservation in the region $z > 0$ in the following manner: If energy flows through two infinite and parallel planes and remains the same, energy conservation is fulfilled solely because the field located at an infinitely large distance from the optical axis generally equals zero. (see Fig.3.4).

3.5.3 Plane wave expansion based on the continuity of $\partial u / \partial z$

Next, we consider the boundary-value problem in which the complex normal derivative $\partial u(x, y, z) / \partial z$ in the field of the plane $z = 0$ is known instead of $u(x, y, 0)$. The diffractive

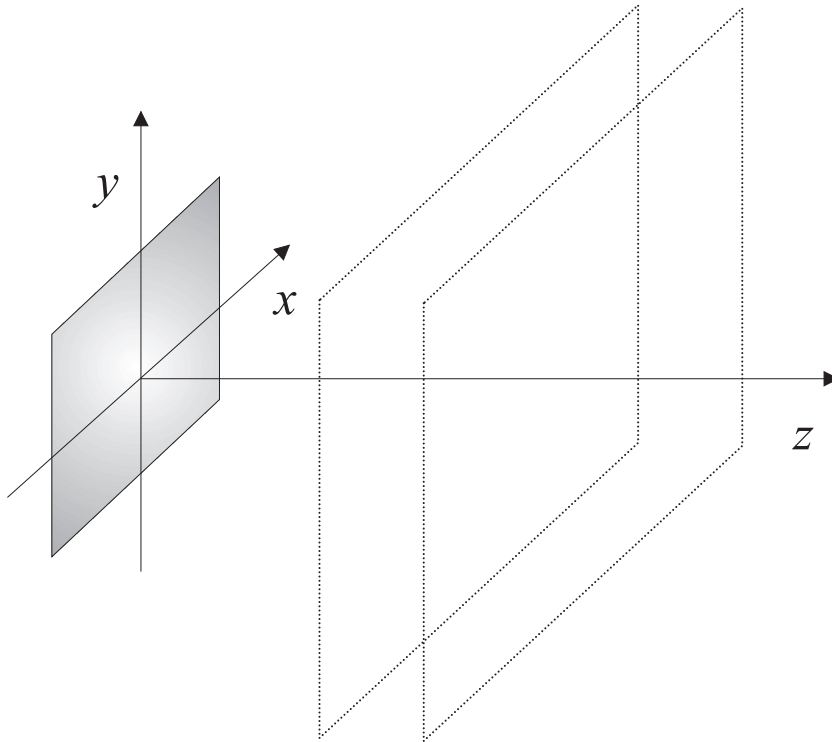


Figure 3.4: Two infinite and parallel planes.

field $u(x, y, z)$ in plane $z > 0$ can be calculated using the following¹:

$$\begin{aligned}
 \tilde{u}'(k_x, k_y, 0) &= \iint_{-\infty}^{+\infty} \frac{\partial u(x, y, z)}{\partial z} \Big|_{z=0} \cdot e^{-i(k_x x + k_y y)} dx dy \\
 u_{II}(x, y, z > 0) &= \iint_{-\infty}^{+\infty} \frac{\tilde{u}'(k_x, k_y, 0)}{i k_z} \cdot e^{i(k_x x + k_y y)} e^{i z k_z} \frac{dk_x dk_y}{(2\pi)^2} \\
 \text{with } k_z &= \sqrt{n^2 k_0^2 - k_x^2 - k_y^2}.
 \end{aligned} \tag{3.43}$$

Plane wave expansion from $\frac{\partial u(x, y, z)}{\partial z} \Big|_{z=0}$ is called PWEII, or the second diffraction formula of plane wave expansion.

A statement will now be given concerning how much energy flows through the lateral

¹See [Sta86, Chapter 4.1.1, equation 4.9b],

plane at $z > 0$:

$$\begin{aligned}
P_z(z > 0) &= \iint_{-\infty}^{+\infty} \mathbf{F}(x, y, z) \cdot \mathbf{e}_z dx dy = \frac{\omega}{2} \Im \left\{ \iint_{-\infty}^{+\infty} u_{II}^*(x, y, z) \frac{\partial u_{II}(x, y, z)}{\partial z} dx dy \right\} \\
&= \frac{\omega}{2} \iint_{-\infty}^{+\infty} \frac{|\tilde{u}'(k_x, k_y, 0)|^2}{k_z} \frac{dk_x dk_y}{(2\pi)^2}. \tag{3.44}
\end{aligned}$$

Again, energy flowing through two infinite and parallel planes at $z > 0$ remains the same. Therefore, energy conservation is maintained. With a real refractive index, there should be no loss of energy in the half zone right of the boundary.

3.5.4 Kirchhoff diffraction

The first Rayleigh-Sommerfeld diffraction integral shown in Eq.3.45 solves the boundary-value problem in which u is known in plane $z = 0$; the second Rayleigh-Sommerfeld diffraction integral shown in Eq.3.46 solves the boundary-value problem in which $\partial u/\partial z$ is known in the plane $z = 0$. The Kirchhoff diffraction integral (Eq.3.47) equals just half the sum of the first and second Rayleigh-Sommerfeld diffraction integrals.

$$u_I(x, y, z) = -\frac{1}{2\pi} \iint_{-\infty}^{+\infty} u(x', y', 0) \frac{\partial}{\partial z} \left(\frac{e^{ikr}}{r} \right) dx' dy' \tag{3.45}$$

$$u_{II}(x, y, z) = -\frac{1}{2\pi} \iint_{-\infty}^{+\infty} \frac{e^{ikr}}{r} \left[\frac{\partial}{\partial z'} u(x', y', z') \right]_{z'=0} dx' dy' \tag{3.46}$$

$$\begin{aligned}
u_K(x, y, z) &= \frac{1}{2} (u_I(x, y, z) + u_{II}(x, y, z)) \tag{3.47} \\
\text{with } r &= \sqrt{(x - x')^2 + (y - y')^2 + z^2}
\end{aligned}$$

According to [Wey19], a spherical wave can also be interpreted as a bundle of plane waves, consisting of possible evanescent waves (Eq.3.48):

$$\frac{e^{ikr}}{r} = \frac{i}{2\pi} \iint_{-\infty}^{+\infty} \frac{e^{i\mathbf{k}\cdot\mathbf{r}}}{k_z} dk_x dk_y \tag{3.48}$$

$$\text{with } \mathbf{r} = (x - x', y - y', z)^T, \quad \mathbf{k} = (k_x, k_y, k_z)^T, \quad k_z = \sqrt{n^2 k_0^2 - k_x^2 - k_y^2}.$$

If the Weyl formula is inserted into Rayleigh-Sommerfeld diffraction integrals, the first Rayleigh-Sommerfeld diffraction shown in Eq.3.45 is equivalent to the PWEI shown in Eq.3.41; the second Rayleigh-Sommerfeld diffraction shown in Eq.3.46 is equivalent to the PWEII shown in Eq.3.43 as well. Therefore, the Kirchhoff diffraction becomes half the sum of PWEI and PWEII.

Now, a statement will be given concerning how much energy flows through the lateral plane at $z > 0$. Since the equivalence of PWEI and Rayleigh-Sommerfeld I, as well as PWEII and Rayleigh-Sommerfeld II, is known, the following can be determined:

$$\begin{aligned}
P_z(z > 0) &= \iint_{-\infty}^{+\infty} \mathbf{F}(x, y, z) \cdot \mathbf{e}_z dx dy \\
&= \frac{\omega}{8} \Im \left\{ \iint_{-\infty}^{+\infty} [u_I^*(x, y, z) + u_{II}^*(x, y, z)] \left[\frac{\partial u_I(x, y, z)}{\partial z} + \frac{\partial u_{II}(x, y, z)}{\partial z} \right] dx dy \right\} \\
&= \frac{\omega}{8} \iint_{-\infty}^{+\infty} |\tilde{u}(k_x, k_y, 0)|^2 \cdot k_z + \frac{|\tilde{u}'(k_x, k_y, 0)|^2}{k_z} + \\
&\quad 2 \cdot \Im \{ \tilde{u}^*(k_x, k_y, 0) \tilde{u}'(k_x, k_y, 0) \} \frac{dk_x dk_y}{(2\pi)^2}. \tag{3.49}
\end{aligned}$$

Again, it can be readily seen that there is no loss of energy in the zone right of the boundary, since $P_z(z > 0)$ does not depend on the z -position. With the real refractive index in the region $z > 0$, total energy should remain constant in this region.

3.5.5 Debye approximation

The Debye approximation, shown in Eq. 3.50¹, is often used to analyze light distribution near the focal point. This approximation indicates that the field near the focal point is a superposition of plane waves with the same amplitudes. Propagation directions of plane waves are inside the geometrical cone formed by drawing straight lines stemming from the focal point through the edge of the aperture.

$$u_D(x, y, z) = \frac{-i}{\lambda} \iint_{Aperture} e^{ik(s_x x + s_y y + s_z z)} \frac{1}{s_z} ds_x ds_y \tag{3.50}$$

¹In [SS81], the integral of the Debye approximation is over (k_x, k_y) instead of (s_x, s_y) , where $(k_x, k_y) = (k \cdot s_x, k \cdot s_y)$.

The Debye integral can also be generalized for superposing plane waves consisting of different amplitudes $a(s_x, s_y)$ [WL81]:

$$u_{DG}(x, y, z) = \frac{-i}{\lambda} \iint_{\text{Aperture}} a(s_x, s_y) \cdot e^{ik(s_x x + s_y y + s_z z)} \frac{1}{s_z} ds_x ds_y. \quad (3.51)$$

After inserting the scalar field u_{DG} from the Debye approximation in the \mathbf{F} -vector, a statement about how much energy flows through the lateral plane at z can now be given:

$$\begin{aligned} P_z(z > 0) &= \iint_{-\infty}^{+\infty} \mathbf{F}(x, y, z) \cdot \mathbf{e}_z dx dy = \frac{\omega}{2} \Im \left\{ \iint_{-\infty}^{+\infty} u^*(x, y, z) \frac{\partial u(x, y, z)}{\partial z} dx dy \right\} \\ &= \frac{\omega k}{2} \iint_{\text{Aperture}} |a(s_x, s_y)|^2 \frac{1}{s_z} ds_x ds_y. \end{aligned} \quad (3.52)$$

This shows that from the Debye integral, energy flowing through the xy -plane depends on the numeric aperture, regardless of how large aperture radii are. As long as $P_z(z)$ does not depend on the z location, energy conservation is also fulfilled for the Debye integral. If plane waves have constant amplitudes, $a(s_x, s_y) = 1$, the energy flowing through a lateral plane results in a compact form:

$$\begin{aligned} P_z(z > 0) &= \frac{\omega k}{2} \iint_{\text{Aperture}} \frac{1}{s_z} ds_x ds_y \\ &= \omega k \pi (1 - \sqrt{1 - NA^2}) \text{ for a circular aperture} \end{aligned} \quad (3.53)$$

3.6 Conditions for energy conservation behind a thin optical element

In this section, we consider a thin element with transmission function $t(x, y)$, located at $z = 0$ as shown in Fig. 3.5. Generally, the incident wave is $u_i(x, y, z < 0) = e^{ikz}$. Observations concentrate on energy flow in the z -direction in the region of $z \geq 0$. Using thin element approximation, the scalar field $u(x, y, z)$ and its derivative immediately at

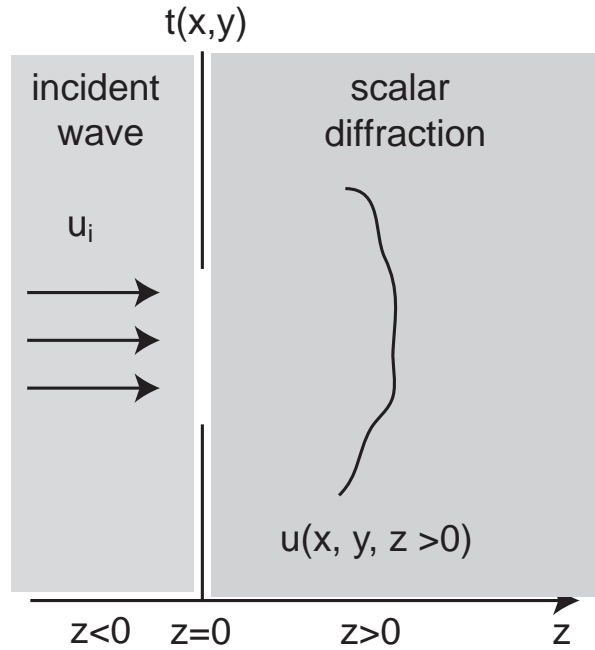


Figure 3.5: Illustration of the nomenclature used at interfaces.

$z = 0$ satisfy:

$$\lim_{z \rightarrow 0^-} u_i(x, y, z) \cdot t(x, y) = t(x, y) \quad (3.54)$$

$$\lim_{z \rightarrow 0^-} \frac{\partial u_i(x, y, z) \cdot t(x, y)}{\partial z} = ik \cdot t(x, y) \quad (3.55)$$

Energy flowing through the lateral plane at $z = 0$ equal the following:

$$\frac{\omega}{2} \Im \left\{ \iint_{-\infty}^{+\infty} u^*(x, y, 0) \frac{\partial u(x, y, z)}{\partial z} \Big|_{z=0} dx dy \right\} = \frac{\omega k}{2} |t(x, y)|^2. \quad (3.56)$$

It will be seen that the energy flux is continuous, if, and only if, both u and $\partial u / \partial z$ are continuous for $z \geq 0$. For a smooth u , it and its divergence are evidently continuous. For example, single plane waves are smooth functions; hence, the energy flux remains continuous in the region described by plane waves. The reason why plane waves are usually used to factorize an arbitrary wave field is that plane waves are the simplest solution for the wave equation. Furthermore, the linearity of Maxwell's equations allow the decomposition into plane waves.

Now, the physical senses of these two continuities will be outlined. Scalar theories

neglect not only the vectorial character of wave fields, but also take only one scalar field into account instead of both electric and magnetic fields. Following Maxwell's equations, both electric and magnetic fields should remain continuous in the tangential direction. Additionally, electric and magnetic fields are rigidly coupled through Maxwell's equations. Therefore, the continuities of u and $\partial u/\partial z$ merely imply the continuities of tangential components for both electric and magnetic fields. For the vectorial theory, one mono-frequent electric (or magnetic) field can be obtained using the curl of another. A curl is a derivative in space. Generally, the scalar field u is supposed to be completely continuous in scalar theory. Compared with the vectorial theory, the completely continuous u means that u is transversal. Transversal u is in y (or/and x) direction. In this case, $\partial u/\partial z$ is the only tangential component in the curl of u . Thus, if both u and its derivative $\partial u/\partial z$ remain continuous in the region at $z \geq 0$, energy conservation will be fulfilled.

For $z > 0$, previous sections have proven that energy conservation is held for all considered scalar theories. Next, we will only investigate whether the one-side limit of $u(x, y, z)$ as z approaches 0 from the right ($z > 0$) is $t(x, y)$, while the one-side limit of $\partial u(x, y, z)/\partial z$ as z approaches 0 from the right ($z > 0$) is $ik \cdot t(x, y)$. Here, we will only take PEWI into consideration.

If the complex field distribution at $z = 0$ is known as $u(x, y, 0) = t(x, y)$, from Eq. 3.40 energy flowing through a lateral plane at $z > 0$ will now be given:

$$P_z(z > 0) = \frac{\omega}{2} \iint_{-\infty}^{+\infty} |\tilde{t}(k_x, k_y)|^2 \cdot k_z \frac{dk_x dk_y}{(2\pi)^2} \quad (3.57)$$

This is constant for all $z > 0$, but its one-side limit as z approaches 0 from the right ($z > 0$) is not equal to Eq. 3.56. To find out the reason for this non-continuous energy flow at $z = 0$, we will check one-side limits of $u_I(x, y, z)$ and $\partial u_I(x, y, z)/\partial z$. As the name indicates, PEWI is based on the continuity of u . However, setting $z = 0$ in the derivative $\partial u_I/\partial z$ yields

$$\lim_{z \rightarrow 0^+} \frac{\partial u_I(x, y, z)}{\partial z} = \iint_{-\infty}^{+\infty} ik_z \cdot \tilde{t}(k_x, k_y) \cdot e^{izk_z} \frac{dk_x dk_y}{(2\pi)^2}. \quad (3.58)$$

The derivative would equal $ik \cdot t(x, y)$ only if the term ik_z inside the integration is

replaced by ik , which is generally not satisfied. Hence, the derivative $\partial u/\partial z$ is not continuous at $z = 0$.

Since $k_z < k$, energy flow in the right space for $z > 0$ (Eq. 3.57) is generally less than $\frac{\omega k}{2} |t(x, y)|^2$ at $z = 0$. The reason for this incontinuity is the abrupt multiplication of incident wave with transmission function $t(x, y)$ at $z = 0$. This decrement is due to the fact that energy at $z = 0$ flows only in z -direction; at $z > 0$, it flows in all directions. Thus, when we concern ourselves with only energy flowing in z -direction, at $z > 0$, it is only a part of the total energy which flows through the xy -plane at $z = 0$.

For other scalar diffraction theories, energy flow in the z -direction also remains non-continuous at $z = 0$. There are summarized in the Table 3.2, and are not proven in detail.

Table 3.2: One-side limits of u and $\partial u/\partial z$ as z approaches 0 from right ($z > 0$) for divers scalar diffraction theories.

	$\lim_{z \rightarrow 0^+} u = t(x, y)$	$\lim_{z \rightarrow 0^+} \partial u/\partial z = ik \cdot t(x, y)$	$\lim_{z \rightarrow 0^+} u ^2 = t(x, y) ^2$
PWE I	true	false	true
PWE II	false	true	true
RS I	true	false	true
RS II	false	true	true
Kirchhoff	false	false	true
Debye*	false	false	false

*Interface locates at $z = -f$

Consequences of incontinuities at the interface plane

Because of their simplicity, scalar diffraction theories mentioned in the previous section are popular in optics research fields. Therefore, it is practical to find an alternative value to replace the \mathbf{F} -vector. Scalar diffraction theories are a sort of approximation based only on one scalar field, instead of on vectorial electric and magnetic fields. Therefore, an alternative value for energy flux is not so critical. All above-mentioned scalar theories have one commonality - the application of the Fourier transformation. Parseval's theorem ensures that the sum of the square modulus remains continuous¹, which can be simply proven. Derivations for all previously-mentioned scalar diffraction theories will not be listed here.

¹Since the Debye theory does not use complete inverse Fourier transformation, Parseval's theorem can not be applied. Consequently, there is no continuity for the sum of $|u|^2$.

Consequently, if one of the above scalar theories is used, the continuity of energy flux is violated behind thin optical elements, but the square modulus remains continuous. To solve the problem of energy conservation, the square modulus is often taken as local energy flow.

3.7 Conclusion

The energy flux in scalar fields is not as trivial as that found in vector fields. Based on the idea of Born/Wolf, the definition of energy flux in complex scalar fields is given. This definition could also be used for an absorbing medium, i.e., its refractive index is complex. The validity of the given definition is proven by comparing it with the Poynting-vector in two simple problems. Following this, various classical scalar diffraction theories are taken into consideration, showing that energy conservation is well-observed in the right half zone. To ensure the continuity of the energy flux, boundary conditions for not only the scalar field, but also its derivative, must be continuous. However, these two boundary conditions are not met in the region of $z = 0$ when the thin element approximation is used. Interesting and also comforting is that if the square modulus is taken as local energy flow, energy conservation will be held in the region of $z = 0$. This is simply because all mentioned scalar diffraction theories apply the Fourier transformation, and Parseval theorem ensures continuity in the sum of the square modulus. In the author's opinion, this is why the square modulus is often considered to be the energy flux and is also often used to check energy conservation between the given scalar field and calculated scalar fields.

Chapter 4

Coherent mask diffraction in absorbing photoresists

Optical lithography uses light to transform a pattern from a mask into a photoresist. A photoresist is a light-sensitive material. During the lithographic process, it absorbs light emitted from the aligner. However, the generally used scalar diffraction theory supports only the analysis of mask diffraction in non-absorbing media, which possess real refractive indices. To transform mask structures in such a thick resist as SU-8 alignment structures for a fiber resonator, absorption is significant. Therefore, one should investigate its impact on final lithographic products. It can be determined from the previous chapter, that local absorption is related to the square modulus of local field amplitude - $n\kappa k_0^2 \omega |u|^2$; this chapter shows how the conventional plane wave expansion can be modified and applied to the investigation of scalar mask diffraction in absorbing photoresists, which, in this case, possess complex refractive indices. Based on Maxwell's equations, modified plane wave expansion supporting the analysis of mask diffraction in absorbing materials is not an inductive hypothesis: one can only replace the real refractive index in traditional plane wave expansion with a complex number. Furthermore, an approximated form allows enhanced plane wave expansion to be simplified to an efficient numerical implementation with complex calculations.

4.1 Introduction

In research fields, including optical lithography, optical storage and surface plasmon analysis, high NA diffraction in the presence of absorption is an essential topic for theoretical analysis. The particular interest of this chapter is UV deep lithography, where during exposure, light propagating into a photoresist is patterned by the mask structure and strongly absorbed by the photoresist. By doing so, the mask pattern is transformed into a thick resist layer of over $100\ \mu\text{m}$. In order to obtain height distribution inside the resist, absorption should be considered during mask diffraction [SC02]. While mask structures under consideration are large enough to allow one to ignore polarization effects, it is assumed that a scalar theory may be applied to simulate mask diffraction.

For the non-paraxial treatment of light propagation in homogeneous media, Kirchhoff- and Rayleigh-Sommerfeld diffraction integrals [Goo96] are two commonly used scalar diffraction theories. In these two theories, diffraction problems are treated using a superposition of spherical waves. This treatment has a rich history that can be traced back to Huygens' principle, developed in 1690. A more simple and practical approach based on the representation of a scattered field as an angular spectrum of plane waves has been independently suggested by several authors [Hön52; Sch42; LW55]. By means of the Weyl's plane wave expansion of a spherical wave [Wey19], the equivalent of the angular spectrum representation and the Rayleigh-Sommerfeld first diffraction formula has been demonstrated [Bou54; Lal68; She67]. Because plane wave expansion is a description of the Fourier domain, the propagation of coherent light is treated simply by multiplying a phase factor. Due to the availability of fast Fourier transformation algorithms, plane wave expansion is ideal for the numerical treatment of scalar non-paraxial light propagation [DH97].

Another classic diffraction study is the treatment of focusing, which solves the problem of obtaining a field not only on the focal plane, but for all points in the vicinity of the focus. It has the same history: first, Lommel's treatment employed spherical wave representations for the focused field. Later, Debye reexamined the focusing problem using an expansion in terms of plane waves. As a vectorial treatment for focusing, the Debye approximation has been extended by several authors [Wol59; TVLB95]. Since the Debye integral is also a description of the Fourier domain, its numerical treatment is rather simple and fast. The Debye approximation can also be extended for imaging

problems, as long as the diameter of the image is small. Exact conditions for the validity of this treatment have been given by Wolf and Li [WL81]. As alternative treatments for analyzing polarization effects of focusing, the stationary phase method presented by Born and Wolf [BW99] and the Hopkins theory [Hop77; FMR96; FM97] are also commonly used.

With respect to absorption, a classical treatment for a single plane wave can be found in [BW99]. For a plane wave in homogeneous media, based on the Beer-Lambert law¹, intensity exponentially decreases in the propagation direction. If an off-axis plane wave passes through an interface from a non-absorbing medium (for example, air) into an absorbing medium (for example, a photoresist), the propagation and descent direction of light will be different; the magnitude of the k-vector in the absorbing medium is no longer constant. Born and Wolf [BW99] have referred to this wave as an "inhomogeneous wave". For their treatment, not only does the index of refraction become complex, but the propagation angles and, hence, the components of the k-vector, become complex quantities as well. These three complex quantities cause difficulties for numerical implementation.

Flagello and Milster [FMR96; FM97] are two often cited references, where plane wave expansion and matrix formalism for the treatment of thin film have been used to analyze vectorial mask diffraction in thin multi-layer resists. Matrix formalism is applied to each plane wave from plane wave expansion. The total vectorial electromagnetic field within the resist is calculated using the summation of all plane waves. When taking absorption into consideration, matrix entries are estimated using the complex refractive index of a resist. The advantage of this method is that reflection could be considered using the matrix formalism. Bollepalli et al. [BKC98] describe a computational algorithm used to model image formation in x-ray lithography based on plane wave expansion. The absorption of a resist is considered part of the transmission function. The value of absorption is estimated using the Beer-Lambert law with a fixed wave number for all plane waves. Ramakrishna and Armour [RA03] compare propagating and evanescent light waves found in absorbing media with the behavior of electrons in the presence

¹According to www.wikipedia.org, the Beer-Lambert law was discovered by Pierre Bouguer before 1729. It is often misattributed to Johann Heinrich Lambert, who cited Bouguer's "*Essai d'Optique sur la Gradation de la Lumiere*," (Claude Jombert, Paris, 1729), and even quoted from it in his work, "*Photometria*" written in 1760. Much later, in 1852, August Beer extended the exponential absorption law to include the concentration of solutions to the absorption coefficient.

of inelastic scattering. An interesting observation is that the imaginary part of the dielectric constant primarily results in the exponential decay of a propagating wave and a phase shift for an evanescent wave. Additionally, the imaginary part of the potential causes an additional scattering which can dominate and actually prevent the absorption of the wave for large enough values. Oughstun [Oug98] demonstrates that in a dispersive, attenuated medium, the estimated wave field obtained from plane wave expansion is a superposition of both homogeneous and inhomogeneous plane waves. As in [BW99], Oughstun deploys complex quantities for all indices of refraction and propagation angles and components of the k -vector. In the research field of laser modeling, symmetry between absorption and amplification is applied [Ram04; JLS99].

The following, based on Maxwell's equations, begins with the propagation of an electromagnetic plane wave across an interface created by two different homogeneous media with general indices. For an interface with a non-absorbing medium and an absorbing resist, observations of inside the absorbing resist reveal an interesting inverse relationship between the z -component of the wave vector and the attenuation coefficient. The derivation of Born and Wolf using the concept of a complex direction vector is introduced, but it does not provide clear evidence for this inverse relationship. The advantage of this inverse relationship is that a useful approximated form of plane wave expansion can be proposed for absorbing media. The approximated plane wave expansion enables a simple and efficient numerical implementation for mask diffraction. A comparison with the exact solution shows that an approximation has sufficient accuracy for off-axis angles up to 90° and κ -values up to 0.03. Finally, a numerical example, focusing into an absorbing medium, is presented. The three-dimensional shape of the focal intensity is significantly influenced by absorption.

4.2 Electromagnetic plane waves in media with complex refractive indices

When treating electromagnetic plane waves in media with a complex index of refraction, the SI-system is used. Since many publications on this subject are based on the Gaussian system, some steps for treating metal optics found in [BW99] will be repeated to clarify

the nomenclature. The first two Maxwell equations are

$$\nabla \times \mathbf{E} = -\dot{\mathbf{B}} \quad (4.1)$$

$$\nabla \times \mathbf{B} = \mu\mu_0 (\sigma\mathbf{E} + \epsilon\epsilon_0\dot{\mathbf{E}}). \quad (4.2)$$

The electric permittivity $\epsilon_0\epsilon$ consists of a dimensionless part ϵ and the permittivity ϵ_0 of free space. Likewise, the magnetic permeability $\mu_0\mu$ consists of a dimensionless part μ , which is typically close to unity and a magnetic permeability μ_0 for the vacuum. σ is the specific conductivity for the medium. The assumption of homogeneous media and a strictly monochromatic wave in form $\mathbf{E} \cdot \exp(-i\omega t)$ results in the following wave equation for absorbing media:

$$\Delta\mathbf{E} + \mu\mu_0 (\omega^2\epsilon_0\epsilon + i\omega\sigma) \mathbf{E} = 0. \quad (4.3)$$

If the relationship $\epsilon_0\mu_0 = 1/c^2$ is applied, the above equation can be written as

$$\Delta\mathbf{E} + \hat{n}^2 k_0^2 \mathbf{E} = 0, \quad (4.4)$$

with the vacuum wave number $k_0 = \omega/c$. A complex index of refraction \hat{n} can arise from a finite conductivity, as in metals, and(or) from a phase shift between the polarization and the electric field, as in absorbing glasses or polymers, resulting in a complex dielectric constant. Independent of this situation, one can write the complex index of refraction as

$$\hat{n}^2 = (n + i\kappa)^2 \quad (4.5)$$

with n as the real index of refraction and κ as the extinction constant. If \hat{n}^2 is denoted as

$$\hat{n}^2 = A + iB, \quad (4.6)$$

it follows

$$n^2 = \frac{1}{2} \left(\sqrt{A^2 + B^2} + A \right) \quad (4.7)$$

$$\kappa^2 = \frac{1}{2} \left(\sqrt{A^2 + B^2} - A \right), \quad (4.8)$$

showing the close relationship between n and κ . The general solution of the wave equation in media with complex indices of refraction is

$$\mathbf{E}(\mathbf{r}) = \mathbf{E}_0 \exp(ik_0 \hat{n} \mathbf{s} \cdot \mathbf{r}), \quad (4.9)$$

which represents a plane wave. This wave is attenuated along the direction of propagation \mathbf{s} , as long as the unit vector \mathbf{s} is a real quantity. In this case, the surfaces of the constant phase and constant amplitude are parallel, as depicted in Fig. 4.1a.

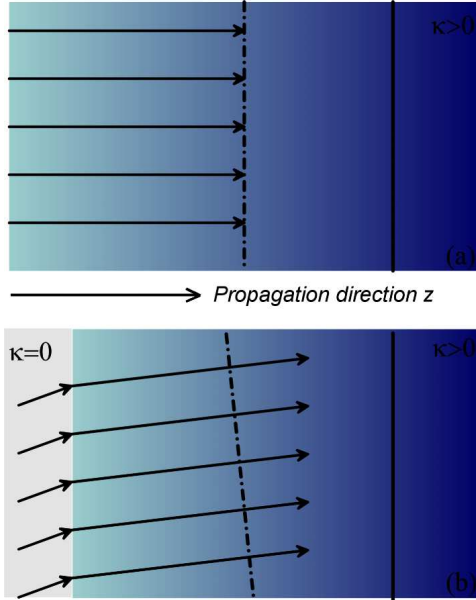


Figure 4.1: The propagation of the plane wave in absorbing media with $\kappa > 0$. The surfaces of the constant phase and amplitude are described respectively using dashes and solid lines. (a) Electromagnetic plane waves in absorbing media. (b) The off-axis electromagnetic plane waves behind an absorbing interface.

4.3 Electromagnetic plane wave at an absorbing interface

If one considers an interface at $z = 0$ with a real refractive index of n_1 for $z < 0$ and a complex refractive index of $\hat{n}_2 = n + i\kappa$ for $z > 0$, the continuity of the tangential components of the electric and magnetic fields would not be maintained as long as \mathbf{s}_2 is a real quantity. Here, \mathbf{s}_1 and \mathbf{s}_2 are the unit direction vectors in media 1 and 2. As a simple description, it is assumed that \mathbf{s}_1 and \mathbf{s}_2 propagate in the x - z -plane. In [BW99],

Snell's law requires

$$n_1 s_{1x} = \hat{n}_2 \hat{s}_{2x} \quad (4.10)$$

resulting in a complex unit vector $\hat{\mathbf{s}}_2$, which satisfies

$$\hat{n}_2 \hat{s}_{2z} = \sqrt{\hat{n}_2^2 - (n_1 s_{1x})^2}. \quad (4.11)$$

Born and Wolf [BW99] also state that the z -component of the complex direction vector \mathbf{s}_2 is represented in its polar form

$$\hat{s}_{2z} = q (\cos \phi + i \sin \phi). \quad (4.12)$$

Equation 4.9 can then be written in the following form

$$\mathbf{E}(\mathbf{r}) = \mathbf{E}_0 \exp(i(k_x x + k_z z)) \exp(-\gamma_z z) \quad (4.13)$$

showing that the z -component of the propagation vector in medium 2 has both oscillatory and attenuation parts. The resulting wave, unlike the standard wave in Fig. 4.1a, has a constant amplitude surface, which is parallel to the surface of the constant phase (see Fig. 4.1b). The real-valued propagation factors, according to [BW99], are related by the following equations:

$$k_x = n_1 k_0 s_{1x} \quad (4.14)$$

$$k_z = q k_0 (n \cos \phi - \kappa \sin \phi) \quad (4.15)$$

$$\gamma_z = q k_0 (\kappa \cos \phi + n \sin \phi). \quad (4.16)$$

This representation shows that $k_x^2 + k_z^2$ is no longer constant. It also indicates a certain relationship between attenuation part γ_z and oscillatory part k_z , but this representation obscures the important fact that k_z is inversely proportional to γ_z , which is a main observation of this chapter.

The following will show that $\gamma_z \propto 1/k_z$. Instead of representing the z -component of

the propagation vector, as in Eq. 4.12, from Eq. 4.11, it follows that

$$\hat{n}_2 \hat{s}_{2z} = \sqrt{\xi} = \frac{1}{k_0} (k_z + i\gamma_z). \quad (4.17)$$

From the complex $\xi = a + ib = r(\cos \phi + i \sin \phi)$, it is obvious that

$$\sqrt{\xi} = \sqrt{r} \left(\cos \frac{\phi}{2} + i \sin \frac{\phi}{2} \right) \quad (4.18)$$

and

$$\Re(\sqrt{\xi}) \Im(\sqrt{\xi}) = r \sin \frac{\phi}{2} \cos \frac{\phi}{2} = \frac{b}{2}. \quad (4.19)$$

Thus, the following is obtained

$$\Im(\sqrt{\xi}) = \frac{1}{2} \frac{\Im(\xi)}{\Re(\sqrt{\xi})}. \quad (4.20)$$

Using $\xi = \hat{n}_2^2 - (n_1 s_{1x})^2$ from Eq. 4.11 and identifying the real and imaginary parts of Eq. 4.17, it follows that

$$\gamma_z = n\kappa k_0^2 \frac{1}{k_z} \quad (4.21)$$

clearly showing that attenuation and propagation parts are inversely proportional to each other. The propagation part can also be solved, resulting in

$$k_z = k_0 \sqrt{\frac{r+a}{2}} \quad (4.22)$$

with

$$a = n^2 - \kappa^2 - \frac{k_x^2}{k_0^2} \quad (4.23)$$

$$b = 2n\kappa \quad (4.24)$$

$$r = \sqrt{a^2 + b^2} = \sqrt{\left(n^2 - \kappa^2 - \frac{k_x^2}{k_0^2} \right)^2 + 4n^2\kappa^2}. \quad (4.25)$$

By inserting all quantities for r and a , the following is obtained:

$$k_z^2 = \frac{(n^2 - \kappa^2)k_0^2 - k_x^2 + \sqrt{[(n^2 - \kappa^2)k_0^2 - k_x^2]^2 + 4n^2\kappa^2k_0^4}}{2}. \quad (4.26)$$

Without restricting propagation on the x - z -plane, the following equation is given for a three-dimensional case:

$$k_z^2 = \frac{(n^2 - \kappa^2)k_0^2 - k_x^2 - k_y^2 + \sqrt{[(n^2 - \kappa^2)k_0^2 - k_x^2 - k_y^2]^2 + 4n^2\kappa^2k_0^4}}{2}. \quad (4.27)$$

An alternative approach is obtained if the process begins with Eq.4.13, i.e., where it is assumed that the wave in medium 2 must have the following form

$$\mathbf{E}(\mathbf{r}) = \mathbf{E}_0 \exp [i(k_x x + k_y y + (k_z + i\gamma_z) z)] \quad (4.28)$$

and the x - and y - parts of the exponents are real, satisfying the continuity of the electric field at the interface. The z -component has the most general form. This field must satisfy the monochromatic wave equation for a medium with a complex refractive index:

$$\Delta \mathbf{E} + \hat{n}_2^2 k_0^2 \mathbf{E} = 0. \quad (4.29)$$

Equating real and imaginary parts immediately leads to the following two equations

$$-k_x^2 - k_y^2 - k_z^2 + \gamma_z^2 = (n^2 - \kappa^2)k_0^2 \quad (4.30)$$

$$\gamma_z k_z = n\kappa k_0^2. \quad (4.31)$$

Eq. 4.31 already contains the desired relationship of Eq. 4.21.

In the following, a useful approximation for equations 4.21 and 4.27 will be derived. Realizing that the attenuation length of intensity, i.e., the length z_e , where intensity drops to e^{-1} , is related to the imaginary part of the refractive index by $\kappa = \frac{k_z}{2nk_0^2 z_e}$, an upper bound for κ in resists or glass can be given. If it is assumed that $z_e > 1\mu m$,

$n = 1.7$ and $\lambda = 365nm$, the corresponding upper bound is around 0.02. In this case,

$$k_z = \sqrt{n^2 k_0^2 - k_x^2 - k_y^2} \quad (4.32)$$

$$\gamma_z = \frac{\kappa k_0}{\sqrt{1 - \frac{k_x^2 + k_y^2}{n^2 k_0^2}}}, \quad (4.33)$$

which represent a very accurate approximation for equations 4.21 and 4.27.

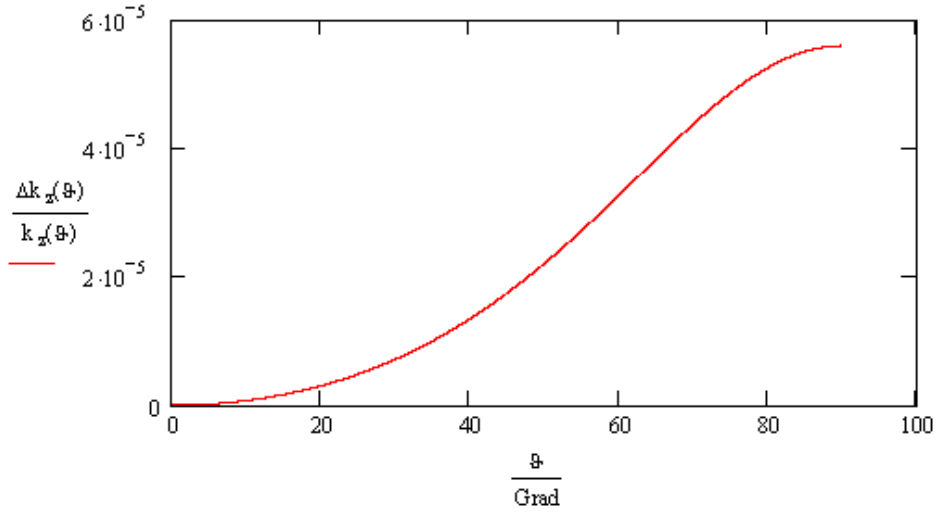


Figure 4.2: Relative error in the approximation, i.e., the difference between approximated k_z (Eq. 4.33) and exact k_z (Eq. 4.27) in relation to exact k_z as a function of the incident angle.

In Fig. 4.2, the relative difference between approximated k_z (Eq. 4.33) and exact k_z (Eq. 4.27) is shown as functions of the incident angle $\vartheta_i = \arcsin\left(\sqrt{s_{1x}^2 + s_{1y}^2}\right)$ for $\kappa = 0.02$. Even in this highly absorptive case of $z_e = 1\mu m$, the relative error over all angles is below 0.006%. Thus, for a usual resist with an attenuation length above $10\mu m$, Eq. 4.33 represents a sufficiently good approximation.

With the approximated k_z and γ_z , the off-axis electromagnetic plane waves for $z > 0$ can be written as

$$\begin{aligned} \mathbf{E}(\mathbf{r}) = & \mathbf{E}_0 \exp(i(k_x x + k_y y)) \exp\left(iz\sqrt{n^2 k_0^2 - k_x^2 - k_y^2}\right) \\ & \exp\left(-\frac{\kappa k_0}{\sqrt{1 - \frac{k_x^2 + k_y^2}{n^2 k_0^2}}} z\right). \end{aligned} \quad (4.34)$$

4.4 Non-paraxial light propagation in absorbing media

Plane wave expansion is an accurate and fast method for calculating the diffraction of an arbitrary scalar wave field. It is assumed that the scalar wave field $u(x, y, z = 0) = u_0(x, y)$ is known. $u_0(x, y)$ might be a transmission function of a binary amplitude mask. The plane wave expansion is given by the Fourier transformation of the electric field at $z = 0$:

$$\tilde{u}_0(k_x, k_y) = \iint_{-\infty}^{+\infty} u_0(x, y) \exp[-i(k_x x + k_y y)] dx dy. \quad (4.35)$$

Consequently, the scalar wave field at $z = 0$ is a linear superposition:

$$u_0(x, y) = \left(\frac{1}{2\pi}\right)^2 \iint_{-\infty}^{+\infty} \tilde{u}_0(k_x, k_y) \exp[i(k_x x + k_y y)] dk_x dk_y. \quad (4.36)$$

The exponential part can be considered as a plane wave at $z = 0$

$$\exp[i(k_x x + k_y y + k_z z)]. \quad (4.37)$$

\tilde{u}_0 can be considered as a weighting factor for the linear superposition. For any monochromatic plane wave in a dielectric medium, the field at $z > 0$ is completely determined by the field distribution at $z = 0$, since the Ewald condition $|\mathbf{k}| = nk_0$ determines k_z as a function of k_x and k_y .

For a plane wave in an absorbing medium, the Ewald condition is substituted using Eq. 4.26 and the plane wave must be replaced by an inhomogeneous wave:

$$\exp[i(k_x x + k_y y + (k_z + i\gamma_z) z)], \quad (4.38)$$

which, at $z = 0$, is identical to the exponent in Eq. 4.36. Since Eq. 4.36 represents a linear superposition, the field for $z > 0$ must be given as the following:

$$u(x, y, z) = \left(\frac{1}{2\pi}\right)^2 \iint_{-\infty}^{+\infty} \tilde{u}_0(k_x, k_y) \exp[i(k_x x + k_y y + (k_z + i\gamma_z) z)] dk_x dk_y. \quad (4.39)$$

For Eq. 4.21, light propagation in absorbing media can finally be expressed as:

$$u(x, y, z) = \left(\frac{1}{2\pi}\right)^2 \iint_{-\infty}^{+\infty} \tilde{u}_0(k_x, k_y) \exp(ik_z z) \exp\left(-\frac{zn\kappa k_0^2}{k_z}\right) \exp[i(k_x x + k_y y)] dk_x dk_y, \quad (4.40)$$

or in $(\nu, \mu) = \frac{1}{2\pi}(k_x, k_y)$, as:

$$u(x, y, z) = \iint_{-\infty}^{+\infty} \tilde{u}_0(\nu, \mu) \exp(ik_z z) \exp\left(-\frac{zn\kappa k_0^2}{k_z}\right) \exp[i2\pi(x\nu + y\mu)] d\nu d\mu, \quad (4.41)$$

where k_z can be taken from Eq. 4.27 in its exact form or from Eq. 4.33 in its approximate form. This approximated integral for absorbing media

$$u(x, y, z) = \iint_{-\infty}^{+\infty} \tilde{u}_0(\nu, \mu) \exp\left(i\frac{z2\pi n}{\lambda} \cos\theta\right) \exp\left(-\frac{z\kappa 2\pi}{\lambda \cos\theta}\right) \exp[i2\pi(x\nu + y\mu)] d\nu d\mu, \quad (4.42)$$

with $\cos\theta = \sqrt{1 - \frac{(\nu^2 + \mu^2)\lambda^2}{n^2}}$

has a visual form, where plane wave expansion for non-absorbing media is augmented by an exponential decay; the decay constant is inversely proportional to the off-axis angle of the wave vector.

4.5 An example of light propagation in absorbing media in the presence of a lens

The perfect focussing lens converts an incident plane wave into a spherical wave around the focal point. Ideally, this lens is a phase object with the following transmissions function:

$$t(x, y) = \exp\left(i\frac{2\pi n}{\lambda} \sqrt{f^2 + x^2 + y^2}\right) \quad (4.43)$$

where f is the focus length, and λ is the wave length. This section presents results for the numerical computation of a perfect spherical lens with $f = 150\mu\text{m}$ and $NA = 0.3334$

and an image field of 2048×2048 pixels, where the pixel size is $0.039\mu m \times 0.039\mu m$. Figures 4a and 4b show the amplitude distribution and real part distribution of the lens. The amplitude (Fig. 4c) distribution at the focal plane is computed for non-absorbing media (dashed curve) and absorbing media (solid curve) with an equal real part $\Re(\tilde{n})$, shown one-dimensionally flowing in a radial direction. When comparing amplitude distribution, there is a wider FWHM, but a weaker oscillation in absorbing media versus non-absorbing media. Figures 4d and 4e illustrate the amplitude distribution on the principal axis for non-absorbing and absorbing media.

4.6 Paraxial light propagation in absorbing media

For the paraxial case $\sqrt{k_x^2 + k_y^2} \ll |\hat{n}k_0|$, the following approximation could be further applied in plane wave expansion:

$$e^{iz\sqrt{\hat{n}k_0^2 - k_x^2 - k_y^2}} = e^{iz\hat{n}k_0\sqrt{1 - \frac{k_x^2 + k_y^2}{\hat{n}k_0^2}}} \approx e^{iz\hat{n}k_0\left(1 - \frac{k_x^2 + k_y^2}{2\hat{n}k_0^2}\right)}. \quad (4.44)$$

The well known Fresnel approximation of light propagation in absorbing media can then be written in the following form

$$\begin{aligned} u(x, y, z) &= \exp\left(i\hat{n}\frac{2\pi z}{\lambda}\right) \iint_{-\infty}^{+\infty} \tilde{u}_0(k_x, k_y) \exp\left[-iz\frac{k_x^2 + k_y^2}{2\hat{n}k_0}\right] \exp[i(xk_x + yk_y)] \frac{dk_x dk_y}{(2\pi)^2} \\ &= \exp\left(i\hat{n}\frac{2\pi z}{\lambda}\right) \iint_{-\infty}^{+\infty} \tilde{u}_0(\nu, \mu) \exp\left[-i\frac{\hat{n}^*}{|\hat{n}|^2}\pi\lambda z(\nu^2 + \mu^2)\right] \\ &\quad \exp[i2\pi(x\nu + y\mu)] d\nu d\mu, \end{aligned} \quad (4.45)$$

where the real refractive index in the ordinary Fresnel approximation is exactly replaced with a complex number. Furthermore, if $\kappa \ll n$, the Fresnel approximation of light propagation is approximated to

$$\begin{aligned} u(x, y, z) &= \exp\left(i\hat{n}\frac{2\pi z}{\lambda}\right) \iint_{-\infty}^{+\infty} \tilde{u}_0(\nu, \mu) \exp\left[-i\frac{\pi\lambda z}{n}(\nu^2 + \mu^2)\right] \\ &\quad \exp[i2\pi(x\nu + y\mu)] d\nu d\mu, \end{aligned} \quad (4.46)$$

because $\frac{1}{\hat{n}} = \frac{n - i\kappa}{|\hat{n}|^2} \approx \frac{1}{n}$.

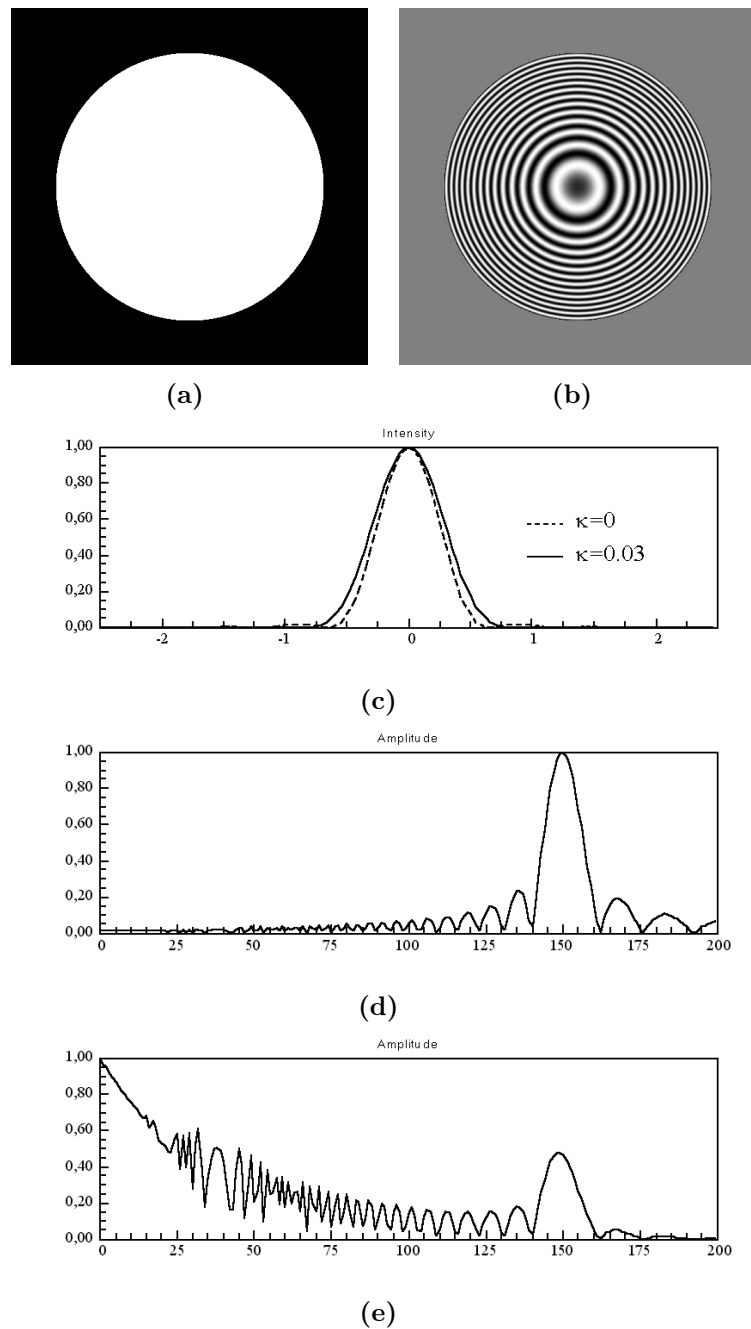


Figure 4.3: The results of the numerical computation for the perfect spherical lens. (a) The amplitude distribution of the perfect spherical lens. (b) The real part of the lens. (c) The radial amplitude distribution at the focal plane in non-absorbing media with $\tilde{n} = 1.7$ (dashed curve) and in absorbing media with $\tilde{n} = 1.7 + 0.03i$ (solid curve). Both amplitude curves are normalized. (d) The normalized amplitude distribution on the principal axis for non-absorbing media with $\tilde{n} = 1.7$. (e) The normalized amplitude distribution on the principal axis for absorbing media with $\tilde{n} = 1.7 + 0.03i$.

4.7 Conclusion

The main observation of this chapter is an inverse relationship between the z-component of the wave-vector and the attenuation coefficient in the z-direction, behind an absorbing interface from an off-axis plane wave. This conclusion assists in the development of a plane wave expansion integral for absorbing media. With the realistic assumption of $\kappa \ll n$ this integral can be approximated as a simple representation.

Chapter 5

Characterizing the angular spectrum of a light source using an optical Fourier operator

The spectral, spatial characteristics of illumination play a role of utmost importance during computer simulation of lithographic processes. This chapter considers conventional UV radiation using a mercury vapor lamp. Its spectral characteristics are well-known: the emission spectrum is in the near-UV wavelength range of 365 nm (i-line), 405 nm (h-line) and 434 nm (g-line). The angular spectrum of the luminous region will be characterized, which is strongly related to the spatial incoherence of the mercury lamp. Here, a simple optical Fourier operator is applied to derive the angular spectrum of the luminous region. The results of this chapter will be applied as a given specification function in the treatment of partially spatial incoherent mask diffraction in Chapter 6.

5.1 Introduction

Most lithographic illumination systems involve a spatially incoherent source to obtain a large and homogenous luminous region with high radiant energy. The spatially incoherent source extends over one or more dimensions, on which each point radiates a beam, which is incoherent with respect to the other points. However, all points radiate the same known frequency spectrum in the near-UV wavelength range of 365 nm (i-line),

405 nm(h-line) and 434 nm (g-line). In practice, the primary illumination source extends only in lateral directions and is located on the focal plane of a condenser. Extension on the longitudinal axis is very small in relation to extensions in lateral directions and can be approximated as a point on the z-axis with a sufficient promise for accuracy. The light of the source is collimated by a condenser to a set of plane waves (see the above figure). Such assumptions for the primary source are also the preconditions needed to create a wide and homogenous luminous region behind the condenser.

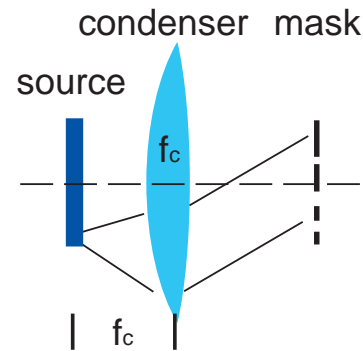


Figure 5.1: *2D light source lies on the focus plane.*

Since the primary light source is located on the focal plane of the condenser, each illuminating point creates a plane wave with a fixed propagation direction and amplitude in the region behind the condenser. Here, the amplitude distribution is dependent on the propagation directions of single plane waves. This amplitude distribution, also known as the angular spectrum of plane waves, is an important specification for a light source. It is necessary for investigating mask diffraction, if the plane wave expansion is to be applied. The propagation direction of a single plane wave is indicated by the location of the illuminating point. For example, if the primary light source consists of only one point, it creates only one plane wave; the corresponding angular amplitude spectrum has only one non-zero value, $A(\alpha_0, \beta_0)$. The input parameter (α_0, β_0) depends on the lateral position of the primary source, while the value of $A(\alpha_0, \beta_0)$ indicates the amplitude of the plane wave.

The advantage of an angular spectrum is that during the later treatment of mask diffraction, it is simple to interpret single plane waves as illuminating light on the mask allowing for conventional coherent diffraction theories to still be used to obtain intensity distributions. Finally, all contributions from single plane waves will be superimposed to estimate the total intensity distribution behind the mask. Hence, deriving the angular spectrum of a luminous region is an initial step for modelling mask diffraction that will be discussed in the following chapters.

5.2 Fourier transformation and angular spectrum

The previous section explained the relationship between one plane wave and one point on the angular spectrum. They have a one-to-one correspondence, which means that if one is known, the other can be easily obtained. For Fourier optics, the inverse Fourier transformation of the complex field distribution $u(x, y)$

$$u(x, y) = \iint_{-\infty}^{+\infty} \tilde{u}(\nu, \mu) e^{2\pi i(x\nu + y\mu)} d\nu d\mu \quad (5.1)$$

can be regarded as a decomposition of $u(x, y)$ into a collection of $\tilde{u}(\nu, \mu) e^{2\pi i(x\nu + y\mu)}$. The constituent part of decomposition can be respectively regarded as a plane wave with a complex amplitude of $\tilde{u}(\nu, \mu)$ and a spatial frequency of (ν, μ) , corresponding with the propagation direction. Thus, the Fourier decomposition of $u(x, y)$ is plane waves decomposition. With the introduction of substitutions $\nu = \frac{\alpha}{\lambda}$ and $\mu = \frac{\beta}{\lambda}$, plane wave decomposition can be formed as

$$A(\alpha, \beta) = \tilde{u} \left(\frac{\alpha}{\lambda}, \frac{\beta}{\lambda} \right) \quad (5.2)$$

$$u(x, y) = \frac{1}{\lambda^2} \iint_{-\infty}^{+\infty} A(\alpha, \beta) e^{\frac{2\pi}{\lambda} i(x\alpha + y\beta)} d\alpha d\beta \quad (5.3)$$

$$A(\alpha, \beta) = \iint_{-\infty}^{+\infty} u(x, y) e^{-\frac{2\pi}{\lambda} i(x\alpha + y\beta)} dx dy. \quad (5.4)$$

$A(\alpha, \beta)$ is the required angular amplitude spectrum of a light field $u(x, y)$ that follows the condenser. This relationship has been explained most eloquently by Goddman [Goo96]. Eq. 5.2 indicates that with an optical Fourier operator, the angular spectrum of plane waves can be specified.

In other words, the angular spectrum of plane waves results from the arrangement of the condenser and the primary light source: the primary light source is located on the focal plane of the condenser. Because of this arrangement, the light field behind the condenser is the Fourier transformation of the primary light source¹. The relationship

¹This entails the Fourier transformation being multiplied with a phase function. The treatment of mask diffraction that will be discussed in Chapter 6 uses intensity superposition. Consequently, the phases of single plane waves play no role after intensity is calculated.

between the modulus of the angular spectrum and the primary source can be derived as the following:

$$|u_s(x_s, y_s)| = \lambda f_c \left| A\left(\frac{x_s}{f_c}, \frac{y_s}{f_c}\right) \right|, \quad (5.5)$$

$$\text{or } I_s(x_s, y_s) = \lambda^2 f_c^2 \left| A\left(\frac{x_s}{f_c}, \frac{y_s}{f_c}\right) \right|^2. \quad (5.6)$$

5.3 Measurement setup

As previously proposed, to obtain an angular spectrum, an optical Fourier operator constituted by a lens and camera located on the focal plane of the lens is used. Together with the condenser, it becomes an inverse imaging system of the primary light source and, therefore, the source $u_s(x_s, y_s)$ or the angular spectrum $A(\alpha, \beta)$ can be specified on the camera. Fig. 5.2 shows the setup needed to obtain the angular spectrum of the luminous region that follows the condenser.

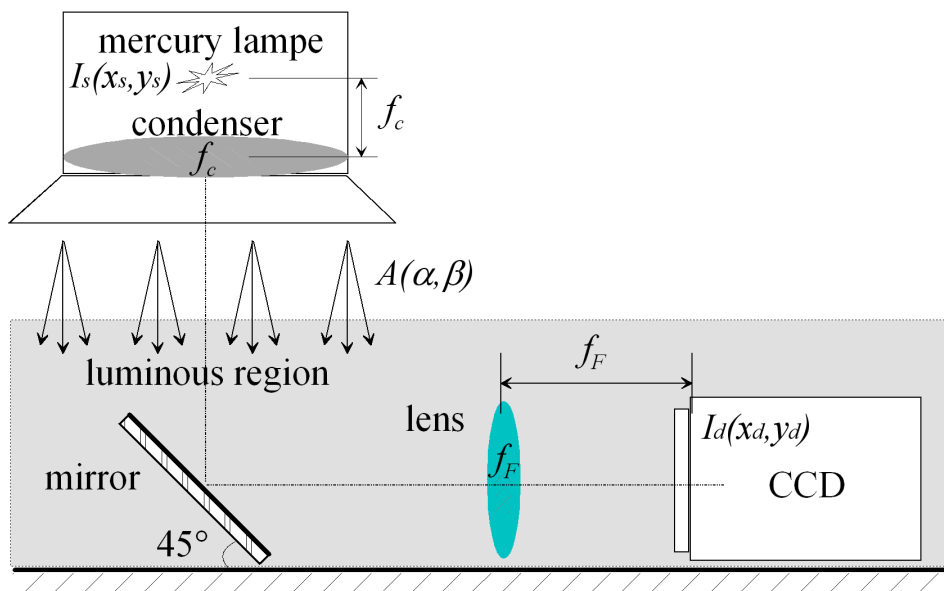


Figure 5.2: The Fourier setup to measure the angular spectrum of the luminous region from a UV mask aligner, as illustrated in the shaded box.

Combining the illumination system of the mask aligner and the optical Fourier setup, the abstract completed optical system is illustrated in Fig.5.3. This optical system images the 2D primary source $I_s(x_s, y_s)$ into a captured CCD-picture $I_d(x_d, y_d) =$

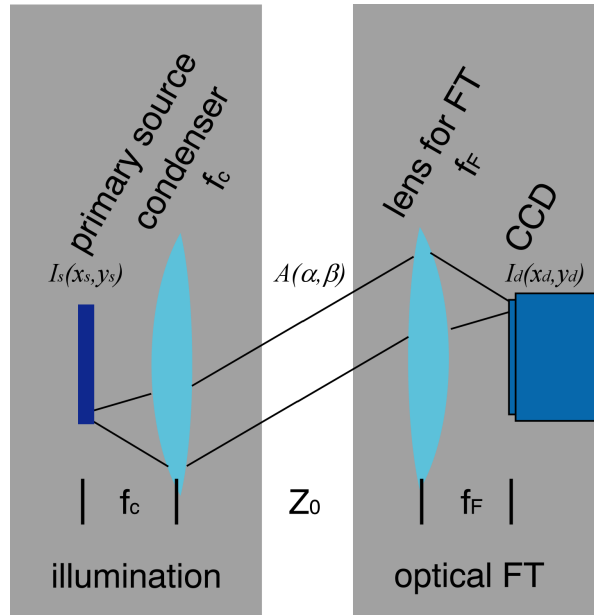


Figure 5.3: The illumination system and optical setup form an imaging system.

$\frac{f_F^2}{f_c^2} I_s(-\frac{x_d f_c}{f_F}, -\frac{y_d f_c}{f_F})$. One question may arise. If the captured image on CCD $I_d(x_d, y_d)$ is dependent on the employed lens in the Fourier system, the subsequent mask diffraction must also be dependent on the employed lens. This dependence should be avoided when employing modeling. How can this dependence be eliminated? The answer involves the angular spectrum. The calculated angular spectrum does not depend on the employed lens in the optical Fourier operator. This is why we analyze the angular spectrum. The relationship between the 2D camera picture $I_d(x_d, y_d)$ and the angular amplitude spectrum $A(\alpha, \beta)$ is

$$I_d(\alpha f_F, \beta f_F) = \lambda^2 f_F^2 |A(\alpha, \beta)|^2. \quad (5.7)$$

5.3.1 Adjusting the lens in the optical Fourier operator

This subsection will discuss how the distance between the lens and CCD-camera in the optical Fourier system can be adjusted to determine the appropriate focal length. It is known that an object at an infinite distance can be imaged onto the focal plane of a lens. This property of the lens allows for the adjustment of the CCD-camera until a perfectly sharp image of the object located at an infinite distance is obtained. This begs the question of what value can be regarded as infinite for the distance of object? Here,

the answer can be found in geometrical optics.

The distance between the lens and CCD-camera has been adjusted so that the image of the object located at distance g is perfectly sharp, illustrated in Fig.5.4a. Now, the actual distance between the lens and CCD-camera is $f + \Delta b$, meaning that there is a misalignment of Δb , compared with the desired camera distance of f . With a distance of $f + \Delta b$, the angular spectrum may be measured. The effect of Δb is that a slightly unfocused picture is captured, as shown in Fig.5.4b. If aberration w caused by defocus is

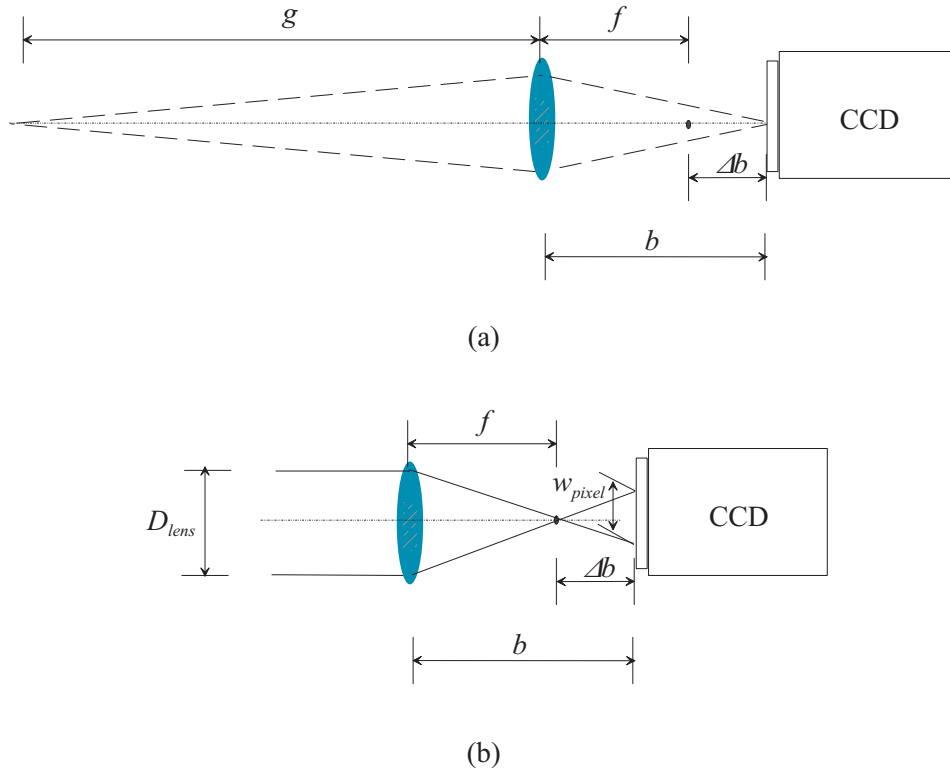


Figure 5.4: (a) Adjustment of distance b to f with a misalignment of Δb . (b) The effect of misalignment Δb on the CCD-picture.

less than the pixel-width of the CCD-camera, in respect to its accuracy, the longitudinal shift of Δb has no effect on the measured angular spectrum. Hence, the allowed Δb can be calculated as:

$$\frac{D_{lens}}{f} = \frac{w}{\Delta b} \quad \text{and} \quad w \leq w_{pixel} \quad \Rightarrow \quad \Delta b \leq \frac{f w_{pixel}}{D_{lens}}. \quad (5.8)$$

From the formula for imaging, the allowed object distance g for the adjustment of the

focal length between the lens and CCD can be derived as the following:

$$\frac{1}{f} = \frac{1}{g} + \frac{1}{b} \Rightarrow g = f + \frac{f^2}{\Delta b}$$

$$g \geq f + \frac{fD_{lens}}{w_{lens}} \quad (5.9)$$

Here, a lens with a focal length of $40mm$ and a diameter of $25mm$ is used. The pixel size of the CCD-camera is $6.75\mu m$. From the equation above, the allowed object distance needed to adjust the camera is around $150m$.

5.3.2 Measured angular spectrum

Using the previously mentioned lens and camera, the angular spectrum of the employed UV-mask aligner is measured. The result is shown in Fig. 5.5. The maximal incident angle in the horizontal direction amounts to $\alpha_{max} = \pm 2.3^\circ$, and the maximal incident angle in respect to the optical axis amounts to $\theta_{max} = \pm\sqrt{\alpha^2 + \beta^2} = \pm 3.3^\circ$.

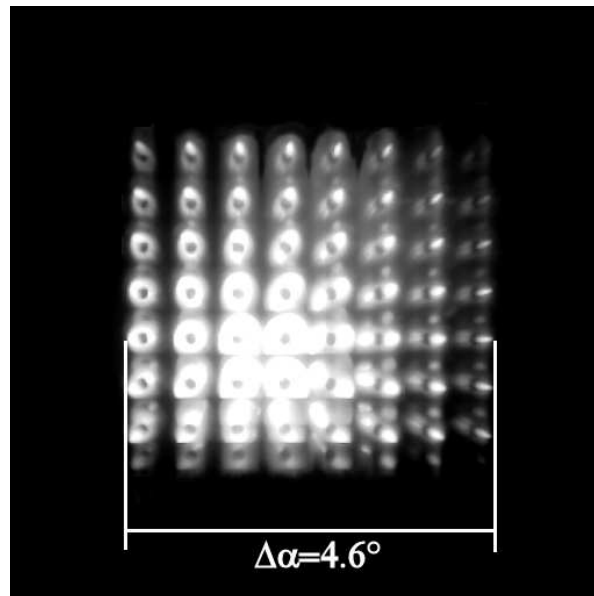


Figure 5.5: *The angular spectrum of the employed UV-mask aligner.*

5.4 Conclusion

For a conventional UV-mask aligner, the relationship between the spatial incoherence of a primary mercury lamp and the angular spectrum of its luminous region behind the condenser is first introduced. A simple optical Fourier operator is proposed to determine the angular spectrum. The measured angular spectrum will be used in Chapter 6 to model incoherent mask diffraction.

Chapter 6

Partially coherent mask diffraction

In order to obtain a highly efficient and large homogeneous luminous region, mask aligners, generally used for optical lithography, emit a partially spatial incoherent illumination for masks. To model mask diffraction with partially spatial incoherent illumination, one should investigate its impact on final lithographic products. As previously mentioned, considered mask structures for alignment structures are large enough to allow one to ignore polarization effects. This chapter applies Fresnel diffraction when analyzing the three-dimensional intensity distribution behind a lithographic mask. Chapter 4 previously demonstrated that light propagation with Fresnel approximation in absorbing media can be treated by replacing the real refractive index with the corresponding complex refractive index. However, the conventional Fresnel approach is valid only for fully coherent illumination. Based on measurement results outlined in chapter 5, mask illumination involves a number of plane waves totally incoherent to each other. Conventional Fresnel diffraction is then used for each plane wave, allowing the total intensity distribution behind the mask to be estimated by summing responses for each single plane wave. By doing so, a lateral intensity distribution derived at a distance behind the mask becomes a convolution of a mask's transmission function with the angle spectrum of the illumination. Additionally, the second operand is scaled by the distance between the mask and the observed lateral plane. A comparison of experimental results and numerical implementations shows that the developed method is reliable. Furthermore, this method can be extended to a more general situation with a polychromatic two-dimensional primary volume source.

6.1 Introduction

For deep lithography, an analysis of three-dimensional intensity distribution behind a lithographic mask is helpful for simulating and understanding photoresist performance. For the sake of efficiency, traditional illumination sources for UV-mask aligners are normally widespread. Another advantage of introducing a widespread source is improving uniformity in the luminous region across an entire mask using a suitable illumination system. Here, the scalar Fresnel approximation is applied to simulate mask diffraction. However, the conventional Fresnel approximation is only for calculating coherent mask diffractions.

With respect to an incoherent or partially coherent illumination source, Hopkins, a pioneer in this research field, developed the first theory [Hop77], and applied it to the analysis of an image plane for projection lithography. SU-8 alignment structures for the fiber resonator are fabricated using contact lithography. Modeling mask diffraction in contact lithographic processes should enable one to analyze three-dimensional intensity distribution behind lithographic masks. To solve this problem, this chapter extends conventional Fresnel approximation, already compatible with three-dimensional mask diffraction, to an incoherent illumination of the mask. As mentioned in Chapter 5, the strength of all single plane waves spread in the luminous region can be determined using the angular spectrum. For each plane wave, three-dimensional intensity distribution behind masks is estimated using Fresnel diffraction. Total intensity distribution behind the mask can then be calculated by summing intensities from all single plane waves. By doing so, conventional Fresnel diffraction is extended to spatially incoherent illumination.

Before beginning a discussion on incoherent light diffraction, it is first necessary to describe a commonly used illumination system for lithographic mask aligners, illustrated in Fig. 6.1. This illumination system can also be specified as the Köhler illumination. A major advantage of the Köhler illumination system is that it enables the nearly uniform illumination of masks from spatially widespread sources. Using the collector, the primary light source is imaged onto the aperture diaphragm, where a secondary source is formed. The light illuminating the lithographic mask is partially coherent, since each single point on the secondary source coherently contributes to all points on the mask; at the same time, each point on the mask obtains incoherent contributions from

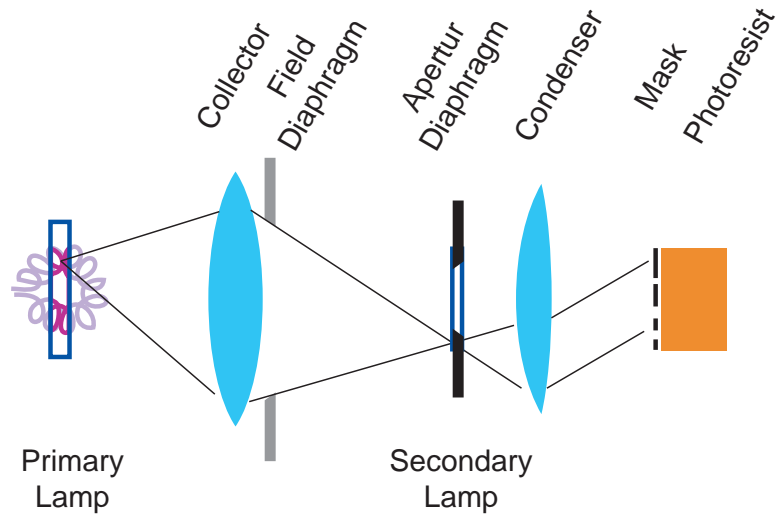


Figure 6.1: *The setup of Köhler illumination applied by a mask aligner.*

all points on the secondary source. To determine partially coherent light diffraction behind the mask, it is easier to go back to the primary or secondary source. For both, contributions from all points are totally incoherent. The complete field distribution from all contributions can be calculated using the summation of intensities; each contribution from a single point on the source can be determined using conventional coherent diffraction. Scalar diffraction using the Fresnel approximation is sufficiently accurate for determining intensity contribution behind a considered mask. Due to the fact that the secondary source is only an optical image of the primary source, to simplify the observation, the primary source will be neglected in the following discussion, with the assumption that the only source is located on the front focal plane of the condenser (Fig. 6.2).

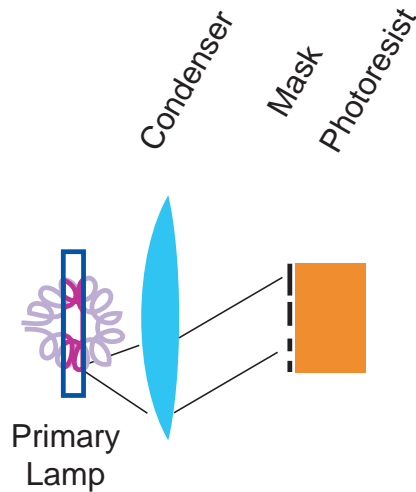


Figure 6.2: *The simplified illumination system applied by a mask aligner.*

diffraction at position z behind the mask:

$$\tilde{u}_{Z_0+z}(\nu, \mu; x_s, y_s) = e^{\frac{2\pi i \hat{n} z}{\lambda}} \tilde{u}_{Z_0^+}(\nu, \mu; x_s, y_s) e^{-\frac{\pi i \lambda z}{\hat{n}}(\nu^2 + \mu^2)}. \quad (6.4)$$

The subscript Z_0+z in $\tilde{u}_{Z_0+z}(\nu, \mu; x_s, y_s)$ is relabeled as z , to note the longitudinal position of z behind the mask. By using the inverse Fourier transformation, the amplitude distribution in (x, y) is obtained and shown as the following,

$$u_z(x, y; x_s, y_s) = \frac{|u_s(x_s, y_s)|}{\lambda f_c} \underbrace{e^{i\Phi} e^{-2\pi i \frac{x x_s + y y_s}{\lambda f_c}}}_{\text{phase}} e^{-i \frac{\pi z}{\lambda \hat{n} f_c^2} (x_s^2 + y_s^2)} u_{m,z} \left(x + \frac{x_s z}{\hat{n} f_c}, y + \frac{y_s z}{\hat{n} f_c} \right) \quad (6.5)$$

$$\text{with } u_{m,z}(x, y) = e^{\frac{2\pi i \hat{n} z}{\lambda}} \iint_{-\infty}^{+\infty} \tilde{u}_m(\nu, \mu) e^{-\frac{\pi i \lambda z}{\hat{n}}(\nu^2 + \mu^2)} e^{2\pi i(x\nu + y\mu)} d\nu d\mu. \quad (6.6)$$

Since every two different points on the source plane radiate incoherent light, cumulative light distribution behind the mask should be the summation of intensity distributions from all single points for the source:

$$\begin{aligned} I_z(x, y) &= \sum_{(x_s, y_s)} I_z(x, y; x_s, y_s) \\ &= \iint_{-\infty}^{+\infty} \left| \frac{u_s(x_s, y_s)}{\lambda f_c} e^{i\Phi} e^{-2\pi i \frac{x x_s + y y_s}{\lambda f_c}} e^{-i \frac{\pi z}{\lambda \hat{n} f_c^2} (x_s^2 + y_s^2)} u_{m,z} \left(x + \frac{x_s z}{\hat{n} f_c}, y + \frac{y_s z}{\hat{n} f_c} \right) \right|^2 dx_s dy_s. \end{aligned}$$

For $\kappa \ll n$ in $\hat{n} = n + i\kappa$, the square modulus $\left| e^{-i \frac{\pi z}{\lambda \hat{n} f_c^2}} \right|^2 \approx 1$. Hence, the summation of intensity distributions from all single points in the source may be simplified as

$$\begin{aligned} I_z(x, y) &= \iint_{-\infty}^{+\infty} \frac{I_s(x_s, y_s)}{\lambda^2 f_c^2} I_{m,z} \left(x + \frac{x_s z}{\hat{n} f_c}, y + \frac{y_s z}{\hat{n} f_c} \right) dx_s dy_s \\ &= \frac{|\hat{n}|^2}{\lambda^2 z^2} I_s \left(-\frac{x \hat{n} f_c}{z}, -\frac{y \hat{n} f_c}{z} \right) \underbrace{*}_{\text{convolution}} I_{m,z}(x, y), \end{aligned} \quad (6.7)$$

$$\text{with } I_{m,z}(x, y) = \left| e^{\frac{2\pi i \hat{n} z}{\lambda}} \iint_{-\infty}^{+\infty} \tilde{u}_m(\nu, \mu) e^{-\frac{\pi i \lambda z}{\hat{n}}(\nu^2 + \mu^2)} e^{2\pi i(x\nu + y\mu)} d\nu d\mu \right|^2 \quad (6.8)$$

$$I_s(x_s, y_s) = |u_s(x_s, y_s)|^2. \quad (6.9)$$

Here, $*$ denotes the convolution operation. Eq. 6.7 indicates that intensity distribution determined behind the mask is a sort of intensity convolution between the source and the mask. The source $I_s(-\frac{x\hat{n}f_c}{z}, -\frac{y\hat{n}f_c}{z})$ is scaled by the focal length of condenser f_c and distance z . The next question is how $I_s(x_s, y_s)$ can be characterized. Since the light from a source is collimated by the condenser, causing a number of plane waves behind the condenser, the angular spectrum of plane waves can be used to specify $I_s(x_s, y_s)$ as the following:

$$I_s(x_s, y_s) = \lambda^2 f_c^2 \left| A\left(\frac{x_s}{f_c}, \frac{y_s}{f_c}\right) \right|^2. \quad (6.10)$$

After inserting this into the convolution formula in Eq. 6.7, intensity distribution behind the mask is obtained and can be then written as the following:

$$\begin{aligned} I_z(x, y) &= \iint_{-\infty}^{+\infty} \left| A\left(\frac{x_s}{f_c}, \frac{y_s}{f_c}\right) \right|^2 I_{m,z}\left(x + \frac{x_s z}{\hat{n}f_c}, y + \frac{y_s z}{\hat{n}f_c}\right) dx_s dy_s \\ &= \frac{|\hat{n}|^2 f_c^2}{z^2} \left| A\left(-\frac{x\hat{n}}{z}, -\frac{y\hat{n}}{z}\right) \right|^2 * I_{m,z}(x, y). \end{aligned} \quad (6.11)$$

By using the convolution theorem, convolution in space can be efficiently implemented by multiplying the frequency domain.

$$\tilde{I}_z(\nu, \mu) = \frac{|\hat{n}|^2 f_c^2}{z^2} \tilde{R}(\nu, \mu) \tilde{I}_{m,z}(\nu, \mu), \quad (6.12)$$

$$\text{with } \tilde{R}(\nu, \mu) = \iint_{-\infty}^{+\infty} \left| A\left(-\frac{x\hat{n}}{z}, -\frac{y\hat{n}}{z}\right) \right|^2 e^{-2\pi i(x\nu + y\mu)} dx dy \quad (6.13)$$

$$\text{and } \tilde{I}(\nu, \mu) = \iint_{-\infty}^{+\infty} I(x, y) e^{-2\pi i(x\nu + y\mu)} dx dy. \quad (6.14)$$

6.2.1 An example of a light source with a Gaussian profile

In this section, we consider a numeric example for mask diffraction in air ($\hat{n} = 1$), illuminated by a spatially incoherent source with a Gaussian intensity profile. This Gaussian source is completely different from the Gaussian beam emanating from a laser. The Gaussian beam from a laser possesses a fixed phase relationship between two different points. The reason why a spatially incoherent source with a Gaussian shape is taken

into consideration is because the width of the source, a decisive parameter for incoherent diffraction, can be simply modified.

The mask applied to the example is shown at the left of Fig.6.4. Two widths of the incoherent Gaussian sources include $\sigma_1 = 100\mu m$ and $\sigma_2 = 300\mu m$, shown respectively at the center and to the right of Fig.6.4. Incoherent light propagation behind the mask is estimated for two different distances and is compared with coherent light propagation. Numerical results are given in figures 6.5 and 6.6, respectively, for distances $z_1 = 1000\mu m$ and $z_2 = 4000\mu m$. The left images show coherent diffractions; middle images are incoherent diffractions illuminated by the Gaussian source with the small radius σ_1 ; images to the right are incoherent diffractions illuminated by the Gaussian source with a large radius of σ_2 .

As noted in the previous section, incoherent diffraction is a quasi convolution of coherent diffraction $I_{m,z}(x, y)$ and the intensity angular spectrum of plane waves, shown in Eq. 6.11. Convolution causes the blurring of $I_{m,z}(x, y)$ by the angular spectrum. The strength of blurring effects depends on the width of $A(-\frac{x}{z}, -\frac{y}{z})$ scaled by $1/z$. Hence, when $1/z$ is very large, in other words a very small z , the scaled angular spectrum $A(-\frac{x}{z}, -\frac{y}{z})$ has a very small width, similar to the coherent diffraction of mask $I_{m,z}(x, y)$ convolved with a delta-function. The convolution of a function with the delta-function results in the function itself. It implies that if the propagation distance z is very small, coherent diffraction dominates. On the other hand, if the width of the source itself is very small, coherent diffraction dominates even over a large distances z . A comparison of numerical results also confirms this statement, showing that the blurring effects are slighter if one observes the last two images in figures 6.5 and 6.6 upwards or to the left.

6.2.2 Experimental verification

In practice, the primary illumination source can be approximated by extending lateral directions only and is located on the focal plane of the condenser. The extension of the longitudinal axis is very small, compared to the extension of lateral directions. Thus, the longitudinal axis extension can be approximated as punctual with sufficient accuracy.

By using the setup detailed in Chapter 5, the employed UV-mask aligner has an angle spectrum of up to 4.6° . To verify incoherent mask diffraction, the intensity distribution $I_z(x, y)$ at z behind the mask is presented in a positive thin photoresist AZ4562 with a thickness of $h_0 \approx 10\mu m$. The photoresist AZ4562 is usually used for

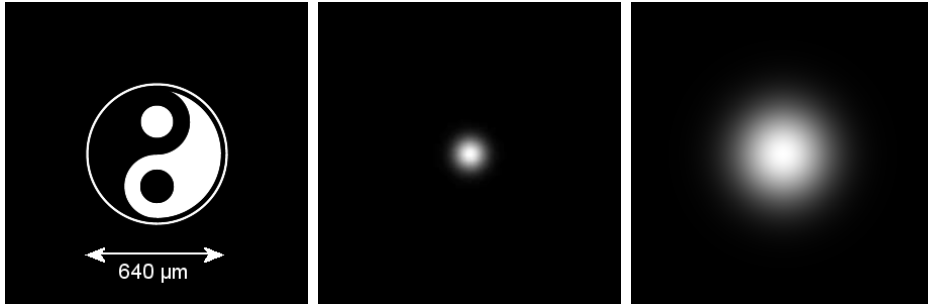


Figure 6.4: *Left: Lithographic mask. Middle: Narrow Gaussian source with $\sigma_1 = 100\mu\text{m}$. Right: Wide Gaussian source with $\sigma_2 = 300\mu\text{m}$.*



Figure 6.5: *Diffraction at $z_1 = 1000\mu\text{m}$ behind the mask. Left: Coherent diffraction. Middle: Incoherent diffraction using the narrow Gaussian source. Right: Incoherent diffraction using the wide Gaussian source.*

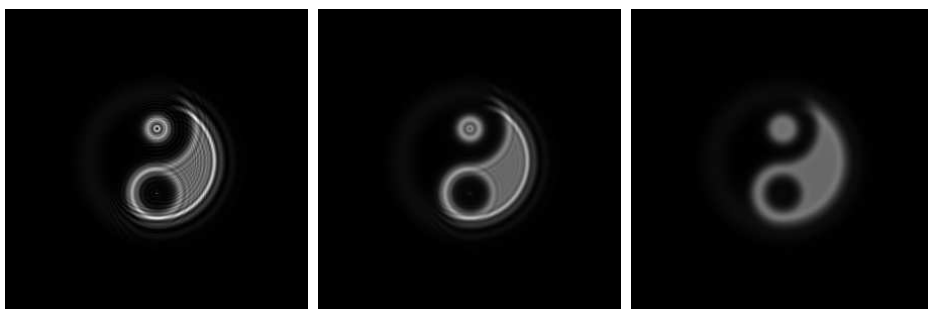
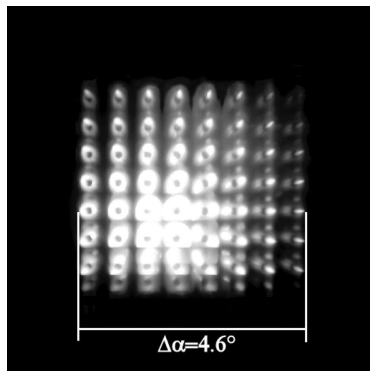
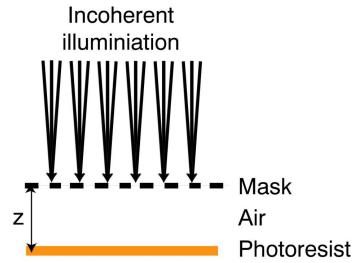


Figure 6.6: *Diffraction at $z_1 = 4000\mu\text{m}$ behind the mask. Left: Coherent diffraction. Middle: Incoherent diffraction using the narrow Gaussian source. Right: Incoherent diffraction using the wide Gaussian source.*



(a)



(b)

Figure 6.7: (a) The angle spectrum of a mask aligner; (b) Exposure of a photoresist under a given intensity.

grayscale lithography. Following development, a height distribution $h(x, y)$ is formed in the photoresist. Height distribution is a proper inverse mapping of intensity distribution $h(x, y) = h_0 - \alpha_0 I_z(x, y)$. Since the medium behind the mask is air, intensity distribution should be calculated using $\hat{n} = 1$. The principle of this experimental verification is illustrated in Fig.6.7.

The mask used in this experiment is given in Fig.6.8. Following the lithographic process, the patterned photoresist is placed under an interferometer and inspected for height distribution by means of an interferogram with an off-axis plane wave as a reference wave. Interferogram measurements are compared with the artificial interferogram obtained using numeric calculations. Measured and calculated interferograms are shown in figures 6.9 and 6.10, respectively, for diffractions at two different z -positions behind the mask. This comparison shows agreement between the height distribution from the experiment and intensity distribution obtained from numerical calculations.

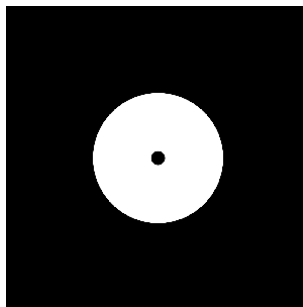


Figure 6.8: The mask for experimental verification.

One noticeable difference is the softer slopes of interferograms obtained through numerical calculations compared to the experiment. This is most likely due to the pho-

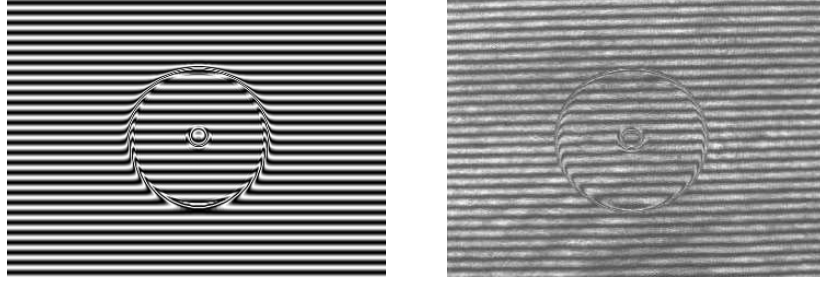


Figure 6.9: Comparison of calculated intensity and measured interferogram at $z = 90\mu\text{m}$. Left: Calculated. Right: Measured.

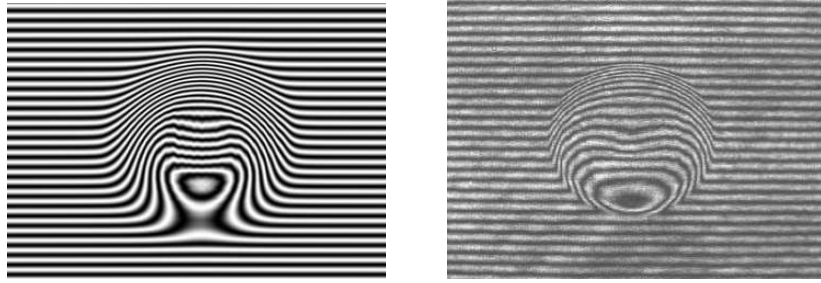


Figure 6.10: Comparison of calculated intensity and measured interferogram at $z = 1230\mu\text{m}$. Left: Calculated. Right: Measured at $z = 1230\mu\text{m}$. Left: Calculated. Right: Measured.

toresist's non-linear behavior during the lithographic process, i.e., non-linear behavior during exposure and development. Except for this difference, agreement found among measured results with numerical simulations indicates that assumed two-dimensional sources are in fact close to realistic outcomes.

6.3 Generalization to polychromatic illumination sources

A mercury vapor lamp has several main peaks in the near-UV spectrum. The wavelengths at 365 nm (i-line), 405 nm (h-line) and 434 nm (g-line) are relevant to optical lithography, whereas other wavelengths are filtered away. It is assumed that $S(\omega)$ is known as the spectrum of the polychromatic illumination source. By introducing another integral over a wavelength, intensity distribution behind the mask can be determined for the polychromatic light source:

$$I_z(x, y) = \int_{-\infty}^{+\infty} S\left(\frac{2\pi c}{\lambda}\right) \iint_{-\infty}^{+\infty} \left| A\left(\frac{x_s}{f_c}, \frac{y_s}{f_c}\right) \right|^2 I_{m,z}\left(x + \frac{x_s z}{\hat{n} f_c}, y + \frac{y_s z}{\hat{n} f_c}, \lambda\right) dx_s dy_s d\lambda, \quad (6.15)$$

with

$$I_{m,z}(x, y) = \left| e^{\frac{2\pi i \hat{n}z}{\lambda}} \iint_{-\infty}^{+\infty} \tilde{u}_m(\nu, \mu) e^{-\frac{\pi i \lambda z}{\hat{n}}(\nu^2 + \mu^2)} e^{2\pi i(x\nu + y\mu)} d\nu d\mu \right|^2. \quad (6.16)$$

Coherent mask diffraction for convolution must be estimated for each wavelength. By doing so, Fresnel diffraction can be extended to an illumination using a polychromatic two-dimensional primary volume source.

6.4 Conclusion

Based on angular spectrum representation, the mask can be considered illuminated through a number of totally incoherent plane waves. The Fresnel approximation is used to calculate intensity distribution caused by a single plane wave, while total intensity distribution behind the mask is determined by summing responses for each single plane wave. This method indicates that intensity distribution is a sort of convolution of a mask's transmission function and the angle spectrum of illumination. By using the convolution theorem, incoherent mask diffraction can be simply implemented by multiplying the frequency domain. A comparison of experimental results and numerical implementations shows that this developed method is reliable. Finally, the method is extended to a more general situation - illumination using a polychromatic two-dimensional primary volume source.

Chapter 7

Optical system for phase reconstruction with phase space representations

Concerning phase retrieval, optical components can be simply measured using an interferometer; however, optical wave fields require a coherent reference wave. This chapter introduces a tomographic method without the requirement of a reference wave. Tomographic methods employing Wigner- or ambiguity functions (WD/AF) have been extensively demonstrated for one-dimensional (1D) functions. For 2D light distributions, the associated WD/AF is 4D, posing several problems. In this chapter, two 1D optical operators are presented, which allows for the reconstruction of arbitrary 2D distributions using only the AF theory for 1D functions. Here, one dimension (y) of the two-dimensional complex light field is considered at each x -position as a set of one-dimensional functions and is reconstructed using the ambiguity function. Additionally, based on the internal redundancy of the ambiguity function, the efficiency of this method is further improved. This chapter also shows that phase reconstruction errors can be minimized by incorporating an appropriate algorithm. At end of this chapter, experimental data illustrating the efficient reconstruction of a refractive micro lens array is presented.

7.1 Introduction

Because optical detectors only record the intensity of an optical field and not the phase, a complex amplitude recovery of optical fields has been of great interest since the development of modern optics. Various approaches can be coarsely grouped into interferometric and non-interferometric methods. Interferometric methods, including classical interferometry and classical and digital holography, always require a coherent reference wave, high spatial resolution and a rigid and clean optical setup. To relax some of these requirements, non-interferometric methods have been considered. One important advantage of non-interferometric methods is that reconstruction is based on intensity measurements of the propagated light field. These intensity distributions are generally smoother than interference patterns. Thus, requirements for spatial resolution are generally much lower, compared to interferometric measurements. In literature, several types of non-interferometric methods have been developed.

Gradient-based methods are one of the earliest non-interferometric methods, including the Foucault Knife-Edge test [Fou59], the Hartmann-Shack wave front sensor [SP71], phase retrieval based on Teague's intensity transport equation [Tea83; Str84; GRN95; GN96] and the Ragazzoni pyramid wave front sensor [Rag96]. Another group of non-interferometric methods uses an iterative approach. The Gerchberg-Saxton algorithm [GS72; ZMD96] and the Fienup algorithm [Fie78; Fie79; Fie80] are two of the best-known iterative algorithms involving iterative forward and backward Fourier transformations between the spatial and Fourier domain, replacing the calculated modulus with the measured modulus in each domain. A similar method was recently proposed by Pedrini [POZ05; PO06], replacing the Fourier transformation with a Fresnel transformation.

Phase-space tomography employing the Wigner- or ambiguity functions is another attractive non-interferometric class of methods for phase retrieval. Using the rotation of phase space, fractional Fourier transformation methods were first employed by Lohmann[Loh93]. Tomographic methods using WD have been proposed for 2D signals [RBM94] and demonstrated for 1D signals [MBC⁺95]. Later Tu and Tamura [TT97b] argued that phase-space methods based on AF are simpler than equivalent methods based on WD. To reconstruct a 2D complex wave, Tu and Tamura [TT97a] propose a simple optical setup that includes two cylindrical lenses oriented along two perpendicular axes in a plan perpendicular to the propagation axis. This method has been verified through

numerical simulation. A more efficient reconstruction of 2D complex wave fields with special symmetry has been demonstrated for the rotationally symmetric case presented by Dragoman et al. [DDB02a; DDB02b].

Recently, we introduced a very efficient method for recovering 2D complex wave fields [LB03]. Since we decompose 2D intensity distribution into 1D intensity scans, only the AF theory for 1D distributions is required. Reconstruction operations are performed for one dimension while the other dimension is considered as a series of parallel optical channels. To implement this reconstruction method, 1D optical operators have been realized. In section 7.3, this new approach is introduced and verified for general 2D complex signals through numerical simulation. This chapter refers to this method as a complete AF reconstruction (CAFR), since the complete AF is reconstructed using intensity measurements.

Since the phase-space consists of spatial and frequency coordinates, its representation of a 2D-signal is four-dimensional (4D), increasing the amount of data that must be measured or stored. Nevertheless, these 4D phase-space representations contain the same information as corresponding 2D wave fields. This illustrates that phase-space representations must be highly redundant. Recently, Dragoman [Dra03; Dra05] and Testorf [Tes05] have pointed out that a section of the Wigner distribution (or an equivalent to AF) is sufficient for recovering the complex amplitude. More interesting, Semichaevsky and Testorf [ST04] have expressed the intensity transport equation in view of the Wigner distribution function and AF. The redundancy investigation in section 7.4 is similar to Dragoman's ideas. In short, it is observed that the complete AF can be estimated using its one segment. For phase recovery, an algorithm for minimizing phase errors in the same section is represented. Finally, experimental results of a 2D phase element will also be presented.

7.2 Definition and properties of the ambiguity function

Equations 7.1 and 7.2 show two equivalent AF definitions for a complex 1D function, where $\tilde{u}(\nu)$ is the Fourier transformation of $u(x)$. Complex conjugation is denoted by $*$. Equations 7.3 and Eq.7.4 are definitions of the Fourier and inverse Fourier transforma-

tions, used in this thesis.

$$A(\nu', x'; u) = \int_{-\infty}^{+\infty} u(x + \frac{x'}{2})u^*(x - \frac{x'}{2})e^{-2\pi i x \nu'} dx \quad (7.1)$$

$$A(\nu', x'; u) = \int_{-\infty}^{+\infty} \tilde{u}(\nu + \frac{\nu'}{2})\tilde{u}^*(\nu - \frac{\nu'}{2})e^{2\pi i x \nu'} d\nu \quad (7.2)$$

$$\tilde{u}(\nu) = \int_{-\infty}^{+\infty} u(x)e^{-2\pi i x \nu} dx \quad (7.3)$$

$$u(x) = \int_{-\infty}^{+\infty} \tilde{u}(\nu)e^{2\pi i x \nu} d\nu \quad (7.4)$$

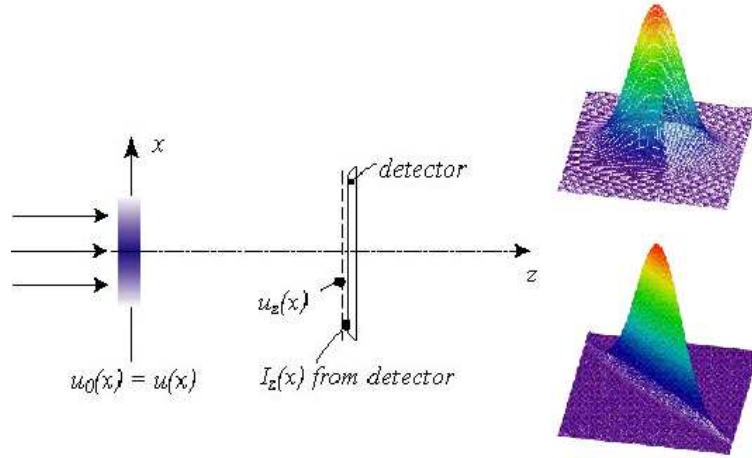


Figure 7.1: *Left: $|u_z(x)|^2$ at one z location; Top right: Ambiguity function; Bottom right: One line in the ambiguity function through the origin*

AF is a phase-space representation of a complex signal $u(x)$. The first property of AF (Eq. 7.5) that enables phase retrieval using intensity measurements is that the Fourier transformation of intensity distribution of the Fresnel transformation (Eq. 7.6 and Fig.7.1) corresponds to one line through the origin in the AF. The angle between this line and the frequency axis depends on the z -position, with z as the propagation

axis.

$$\int_{-\infty}^{+\infty} u_z(x)u_z^*(x)e^{-2\pi i x \nu'} dx = A(\nu', -z\lambda\nu'; u) \quad (7.5)$$

$$\text{with } u_z(x) = \int_{-\infty}^{+\infty} \tilde{u}(\nu)e^{-\pi i \lambda z \nu^2} e^{2\pi i x \nu} d\nu \quad (7.6)$$

By measuring $u_z(x)u_z^*(x)$ for a set of different locations z in the propagation direction, the full AF can be reconstructed with appropriate border conditions (Fig. 7.2).

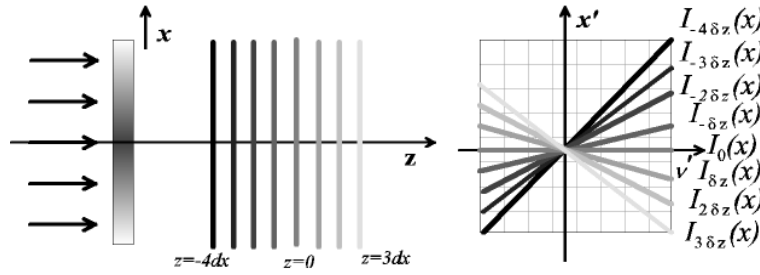


Figure 7.2: Reconstruction of the ambiguity function from intensity measurements for a set of z positions.

Finally, from AF, $\hat{u}(x)$ is reconstructed, which is the original 1D signal multiplied by an unknown complex constant $u^*(0)$:

$$\hat{u}(x) = u(x)u^*(0) = \int_{-\infty}^{+\infty} A(\nu, x; u)e^{\pi i x \nu} d\nu. \quad (7.7)$$

Since only the complex amplitude distribution is of interest, one unknown complex factor is usually irrelevant. The presence of $u^*(0)$ in Eq. 7.7 indicates that this reconstruction method doesn't work if $u^*(0)$ is zero, indicating $\hat{u}(x) = 0$. By applying suitable shifts, this restriction can be avoided.

In practical propagation situations, only intensities at z -locations less than one maximal z_{max} can be measured. These intensities correspond to a partial angular section of AF. One extreme situation is the achievement of the vertical line in AF, $A(x', \nu' = 0)$, which corresponds with the measurement at $z = \infty$. For measurements calculating the remaining section of AF, another property of AF is used:

$$A(x', -\nu'; u) = A(\nu', x'; u). \quad (7.8)$$

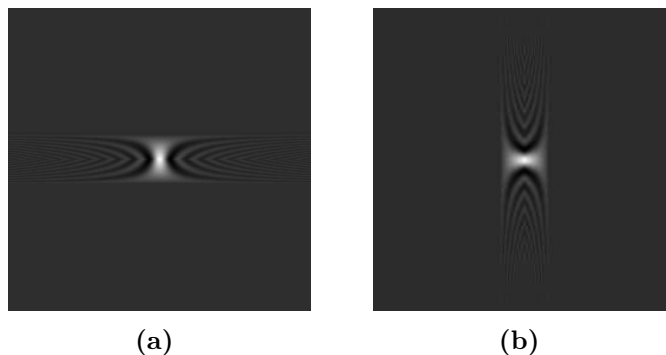


Figure 7.3: The FT results in a 90° rotation of AF. x' is vertical and ν' is horizontal. a) AF (modulus) of a rectangle function. b) AF (modulus) of the sinc-function, Fourier transformed from the same rectangular function.

In other words, the FT results in a 90° rotation of AF, allowing for the measurement, for instance, $|\tilde{u}(\nu)|^2$ at $z = 0$ instead of $|u_\infty(x)|^2$ at $z = \infty$, to obtain the vertical line $A(\nu' = 0, x')$. To illustrate this property, AFs for a rectangular function and its FT are shown together in Fig. 7.3.

7.3 Reconstruction method

To enable the use of this reconstruction method for 2D complex signals, two optical systems for a 1D-propagator and a 1D-Fourier-propagator have been developed, which realize the 1D propagation of 2D input signals and their Fourier transformations. If the y -axis is the affected axis of the 1D operator, as shown in Fig. 7.4, each column in the camera picture at z is the intensity of the 1D Fresnel propagation (for 1D-propagator) or 1D FT then Fresnel propagation (for 1D-Fourier-propagator) from the same column of the input signal. Equation 7.9 expresses the 1D Fresnel propagation of a 2D input signal in a mathematical form.

$$\begin{aligned} \tilde{u}_z(\nu; x_i) &= \tilde{u}_0(\nu; x_i) e^{-\pi i \lambda z \nu^2} \\ \text{with } \tilde{u}(\nu; x_i) &= \int_{-\infty}^{+\infty} u(y; x_i) e^{-2\pi i y \nu} dy. \end{aligned} \quad (7.9)$$

In Eq. 7.9, $u(y; x_i)$ is a column of the 2D-function $u(x, y)$ at $x = x_i$.

From intensity measurements for a series of different positions for z , all i -th columns of 2D camera pictures are collected and then used to reconstruct AF for the i -th column

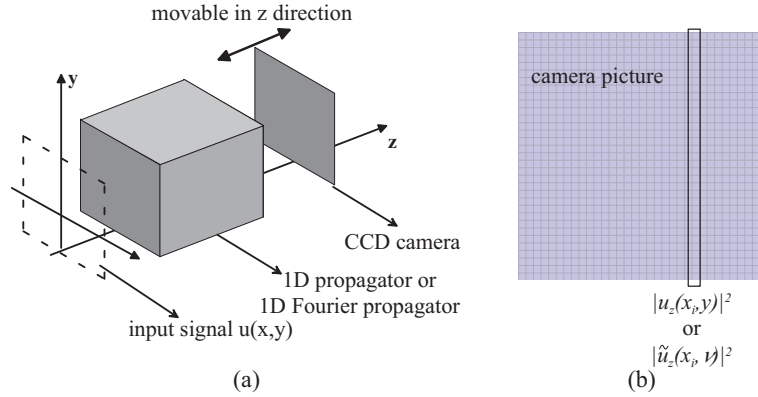


Figure 7.4: (a) 1D propagation operator with respect to the y -axis. The x -axis is imaged. (b) Camera picture.

of the input signal using Eq. 7.7, written as the following:

$$\hat{u}_c(y; x_i) = u^*(x_i, 0)u(x_i, y) = \int_{-\infty}^{+\infty} A_c(\mu, y; u(x_i, y)) e^{\pi i y \mu} d\mu. \quad (7.10)$$

In Eq. 7.10, $\hat{u}_c(y; x_i)$ is a column reconstruction at $x = x_i$; $A_c(\mu, y; u(x_i, y))$ is the AF of the original column-function $u(x_i, y)$ for the same x_i . This process is repeated for all columns $i = 0..N - 1$. Because columns are independently reconstructed, these unknown constants are different for each column. To determine $u^*(x_i, 0)$, the input distribution (or the optical setup) is rotated by 90° around the optical axis z , so that the 1D propagator now acts with respect to x . This measurement procedure is repeated. Thus, all rows may be reconstructed. Row reconstruction provides $u_r(x; y_j)$ for a series $j = 0..N - 1$ of rows, again with unknown complex factors:

$$\hat{u}_r(x; y_j) = u^*(0, y_j)u(x, y_j) = \int_{-\infty}^{+\infty} A_r(\nu, x; u(x, y_j)) e^{\pi i x \nu} d\nu. \quad (7.11)$$

$A_r(\nu, x; u(x, y_j))$ is the AF of the j -th row $u(x, y_j)$. One row can now be used, e.g. $\hat{u}_r(x; y_0)$ to determine $u(x_i, 0)$ up to a global complex factor:

$$\begin{aligned} \hat{u}(x_i, y_j) &= \hat{u}_c(y_j; x_i) \frac{\hat{u}_r(x_i; y_0)}{\hat{u}_c(y_0; x_i)} \\ &= u^*(x_i, 0)u(x_i, y_j) \frac{u^*(0, y_0)u(x_i, y_0)}{u^*(x_i, 0)u(x_i, y_0)} \\ &= u^*(0, y_0)u(x_i, y_j). \end{aligned} \quad (7.12)$$

$\hat{u}(x, y)$ is the final 2D result, which is the reconstructed complex input function $u(x, y)$, multiplied by a global constant factor $u^*(0, y_0)$.

A brief complexity analysis shows that for a 2D-input distribution with $N \times N$ samples, this method requires the reconstruction of N two-dimensional AFs, i.e. N^3 data. Using traditional methods, a four-dimensional AF (N^4) must be reconstructed. Furthermore, for the reconstruction of a four-dimensional AF, it is insufficient to merely vary the z -position.

In the following, we first present optical 1D operators and then give a thorough description and numerical simulation for the reconstruction method.

7.3.1 Optical 1D propagator

In the previous theoretical description, a 1D propagation operator is required. Such an operator must perform an imaging operation for one axis (x) and an independent propagation operation for the other (y). Here the desired ABCD-matrix is:

$$\begin{pmatrix} \mathbf{A} & \mathbf{B} \\ \mathbf{C} & \mathbf{D} \end{pmatrix} = \begin{pmatrix} 1 & 0 & 0 & 0 \\ 0 & 1 & 0 & z \\ 0 & 0 & 1 & 0 \\ 0 & 0 & 0 & 1 \end{pmatrix}, \quad (7.13)$$

where one looks for the optical system consisting of only lenses and pieces of free space propagation. Here the realization should not only have as few elements as possible, but should also provide the following flexibilities. First, one should avoid adjusting the parameter z in Eq. 7.13 by varying the lens for diverse focal lengths, since this is not practical and even impossible for arbitrary focal lengths. Therefore, the acceptable choice is varying one propagation distance to realize the diverse z . Second, negative z could be realized.

The setup in Fig. 7.5 implements the desired 1D propagation operator. In the reference plane at $z = 0$, input $u(x, y)$ is located. In case of $z_p = 0$, the intensity of input $u(x, y)$ is captured on the CCD camera. Changing z_p allows for propagation only in the y -direction, while for the x -axis, a one-to-one mapping is performed. The camera has the intensity of a 1D (y) Fresnel propagated input signal. To analyze the optical setup, the x - and y -axes (Fig. 7.6 a and b) are separately observed. This is possible since

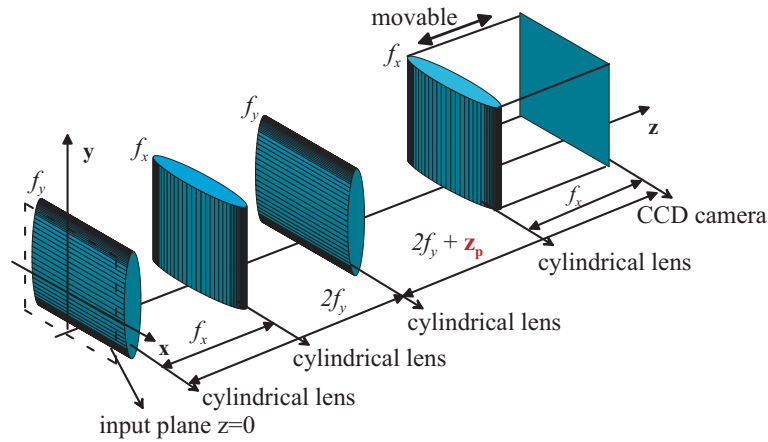
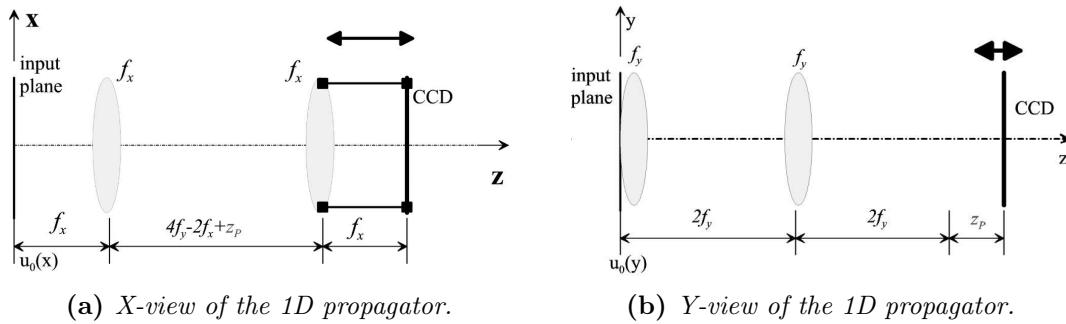


Figure 7.5: 1D optical propagator, where the y-axis is the affected axis.

the Fresnel propagation and cylindrical lenses are x-y-separable. However, it does not mean that separateness is a restriction of the input signal from using this reconstruction method.



(a) X-view of the 1D propagator.

(b) Y-view of the 1D propagator.

Figure 7.6: The 1D propagator separately observed for the x- and y-axes.

First, the x-axis performs a one-to-one mapping for every z_p because, for this system, the distance between two lenses can be varied without affecting the intensity distribution of the output plane. On the y-axis at $z = 4f_y$, a one-to-one mapping is observed because this system corresponds to the classic imaging system with unit magnification. By adding a z_p , the desired 1D propagation can be implemented, but only on the y-axis.

The performance of the setup can be described using the following ABCD matrices:

$$\begin{pmatrix} \mathbf{A} & \mathbf{B} \\ \mathbf{C} & \mathbf{D} \end{pmatrix} = \begin{pmatrix} -1 & 0 & 0 & 0 \\ 0 & -1 & 0 & -z_p \\ \frac{4f_y - 4f_x + z_p}{f_x^2} & 0 & -1 & 0 \\ 0 & 0 & 0 & -1 \end{pmatrix}, \quad (7.14)$$

When compared with Eq. 7.13, one observable difference is the matrix entry $\frac{4f_y - 4f_x + z_p}{f_x^2}$, which only affects the phase. Since intensity is measured, this matrix entry then has no effect on these measurements. Another difference is the matrix in Eq. 7.14, which is the product of the matrix in Eq. 7.13 with the minus identity matrix $-\mathbf{I}$. Chapter 2 pointed out that multiplying the minus identity matrix $-\mathbf{I}$ indicates a mirrored coordinate.

As designed, the given setup in Fig. 7.5 performs an optical 1D propagator. Its experimental verification is given in section 7.3.3. For practical reasons, the propagation distance is limited to $\pm(2f_y - f_x)$. Therefore, only a finite angular segment of AF can be measured using this system.

7.3.2 Optical 1D Fourier-propagator

The propagation operator described above can only measure the intensity for distances $|z| < 2f_y - f_x$, which corresponds with an angle segment of the full 2D space in the ambiguity domain. In order to measure the remaining angle segment, a 1D FT and propagation operator has been developed, i.e., a 1D Fourier transformation and propagation operator over a distance z_F is performed. Here, the desired ABCD-matrix for such a 1D Fourier-propagator is as follows:

$$\begin{pmatrix} \mathbf{A} & \mathbf{B} \\ \mathbf{C} & \mathbf{D} \end{pmatrix} = \begin{pmatrix} 1 & 0 & 0 & 0 \\ 0 & 1 & 0 & z_F \\ 0 & 0 & 1 & 0 \\ 0 & 0 & 0 & 1 \end{pmatrix} \begin{pmatrix} 1 & 0 & 0 & 0 \\ 0 & 0 & 0 & -f \\ 0 & 0 & 1 & 0 \\ 0 & \frac{1}{f} & 0 & 0 \end{pmatrix} = \begin{pmatrix} 1 & 0 & 0 & 0 \\ 0 & \frac{z_F}{f} & 0 & -f \\ 0 & 0 & 1 & 0 \\ 0 & \frac{1}{f} & 0 & 0 \end{pmatrix}. \quad (7.15)$$

An optical system consisting of only lenses and pieces of free space propagation is desired. Similar to a 1D propagator, divers z_F can be adjusted by varying one aspect of the propagation distance.

Fig.7.7 shows a system which realizes the optical 1D Fourier-propagator. To discuss

its operation, the x- and y-axes are again considered separately. For the x-axis (Fig.

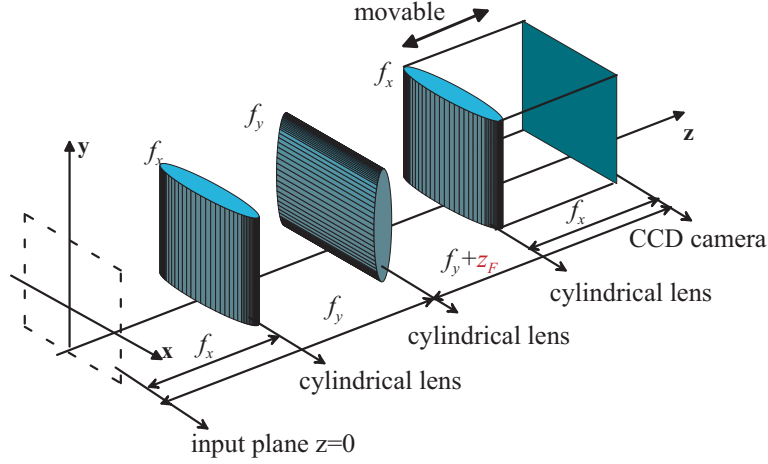
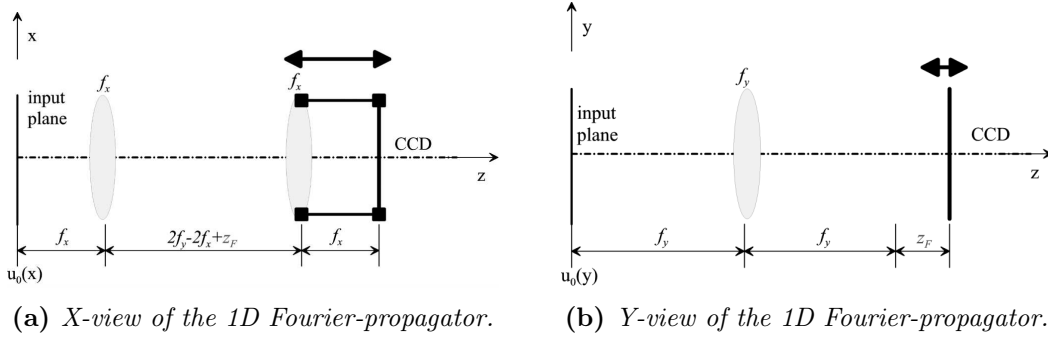


Figure 7.7: 1D optical Fourier-propagator, where the y-axis is the affected axis.



(a) X-view of the 1D Fourier-propagator. (b) Y-view of the 1D Fourier-propagator.

Figure 7.8: The 1D Fourier-propagator separately observed for the x- and y-axes.

7.8a), the optical system is identical to the 1D propagation operator. For the y-axis (Fig. 7.8b), the system is a 2f- Fourier transformer. At $z_f = 0$, $\tilde{u}\left(-\frac{x}{\lambda f_y}\right)$ is obtained. The additional separation z_f allows for the combination of Fourier transformation with propagation. The system can also be described in terms of the following ray-transfer matrices.

$$\begin{pmatrix} \mathbf{A} & \mathbf{B} \\ \mathbf{C} & \mathbf{D} \end{pmatrix} = \begin{pmatrix} -1 & 0 & 0 & 0 \\ 0 & \frac{-z_F}{f_y} & 0 & f_y \\ \frac{2f_y - 4f_x + z_F}{f_x^2} & 0 & -1 & 0 \\ 0 & \frac{-1}{f_y} & 0 & 0 \end{pmatrix}, \quad (7.16)$$

As designed, the system performs an intensity image for the x-axis and a sequence of Fourier transformations and propagations for the y-axis. Its experimental verification is given in section 7.3.3. For practical reasons, the propagation distance is limited to $\pm(f_y - f_x)$.

7.3.3 Experimental verification of 1D operators

To verify the functionality of the optical operators, the results of numerical 1D-operations of a two-dimensional wave field are compared with results from experimental 1D operators. As an input signal, we have used a circular aperture with a diameter of $0.6\mu m$ (Fig. 7.9), which is illuminated by a plane wave. The 1D

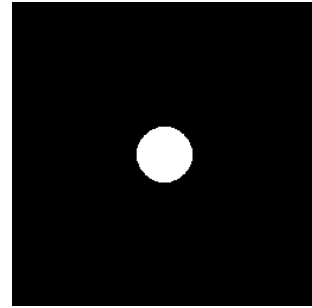


Figure 7.9: *A circular aperture.*

Fresnel propagation behind the circular aperture has been numerically calculated and measured using the 1D propagator. Figures 7.10a and 7.10b illustrate calculated and measured intensity distributions. The 1D FT of the circular aperture has also been numerically calculated and measured using the 1D Fourier-propagator with $z_F = 0$. Figures 7.11a and 7.11b illustrate calculated and measured intensity distributions. Comparisons clearly indicate that the two setups perform the desired operations.

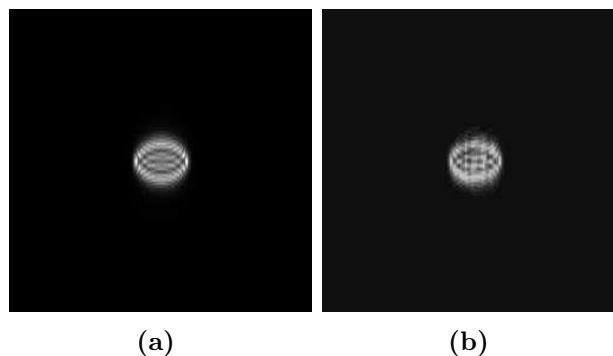


Figure 7.10: *One-dimensional light propagation behind the circular aperture. Comparisons of intensities calculated using a numerical simulation (a) and measured using the optical 1D propagator (b).*

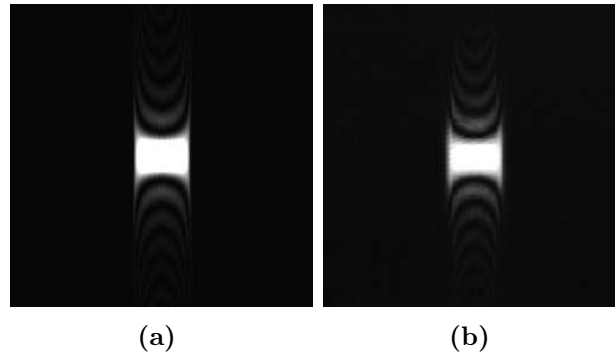


Figure 7.11: One-dimensional FT of the circular aperture. Comparisons of intensities calculated using a numerical simulation (a) and measured using the optical 1D Fourier-propagator ($z_F = 0$) (b).

7.3.4 Outline of the method and a numerical demonstration

The first proposed concept for reconstructing the complex amplitude of light by use of AF is a complete AF reconstruction (CAFR), by which the complete AF is calculated using intensity measurements. To solve the problem of a limited accessible z -range, AF is divided into dark blue and bright blue segments shown in Fig. 7.12a. Both segments can be achieved using intensity measurements within the limited and accessible z -range. The solution is to use the Fourier property of AF; the FT of $u(x)$ indicates a 90° rotation of $A(x', \nu'; u)$.

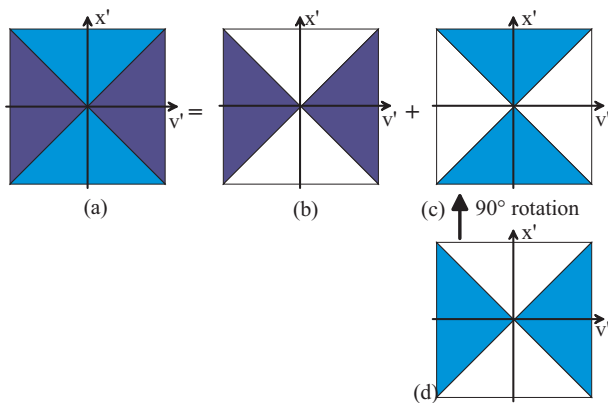


Figure 7.12: The complete AF (a) can be considered as the integration of the dark blue segment (b) and the bright blue segment (c), the white segments in (b) and (c) have a value of zero. Segment (c) is achieved through (d) using the Fourier-propagator.

The CAFR begins with acquiring data by measuring the intensities for a set of z -positions using a 1D propagator and 1D Fourier-propagator. Following data acquisition is data processing. The columns of all measured 2D intensities are numbered from 1 (left) to N (right). The columns with the same number, i.e., i -th columns, are then collected and transformed by Fourier. Finally, it is inserted to the proper line on AF, which also

corresponds with the i -th column of an input signal. Now, AF is complete. From this, the complex i -th column can be reconstructed, but with an unknown constant. This is repeated for columns with all numbers from 1 to N . All columns of the input signal are also obtained, but with unknown constants in each column. To eliminate unknown constants, one row of the input signal is reconstructed, which can be realized by rotating the input signal by 90° . Using this row, reconstructed columns can be adjusted by proper values, referred to as an x-correction. After implementing an x-correction, the complex 2D input signal is reconstructed consisting of one global unknown constant.

Fig. 7.13 illustrates the entire CAFR. The result of a numerical reconstruction is shown at the end of this figure. Next to the numerical result, the original 2D signal is also shown for comparison. The 2D input signal is a micro lens array with two different focus lengths. Compared with the original input signal, the major difference is located in phases where the modulus is zero. It is well-known that the phase is indeterminate if the modulus is zero.

The next section discusses an improvement in this reconstruction method using the redundancy property of AF.

7.4 Improved reconstruction method

This section will show that the efficiency of the previously described method can be further improved using the redundancy of AF. The redundancy of AF allows for the complete AF to be obtained from one of its own segments. The reconstruction method is then illustrated. An algorithm for minimizing phase errors is also demonstrated. Finally, experimental results of a 2D phase element will be presented.

7.4.1 Redundancy property of the ambiguity function

As previously mentioned, the phase-space representation contains the same amount of information as its complex input signal, but its dimension is doubled. Dragoman [Dra03; Dra05] Testorf and Semichaevsky [Tes05; ST04] utilize this redundancy and point out that the complex signal can be reconstructed using only a section of AF. The approach presented in the following is very similar to the method described by Dragoman [Dra03], which utilizes one line of an AF parallel to the frequency axis.

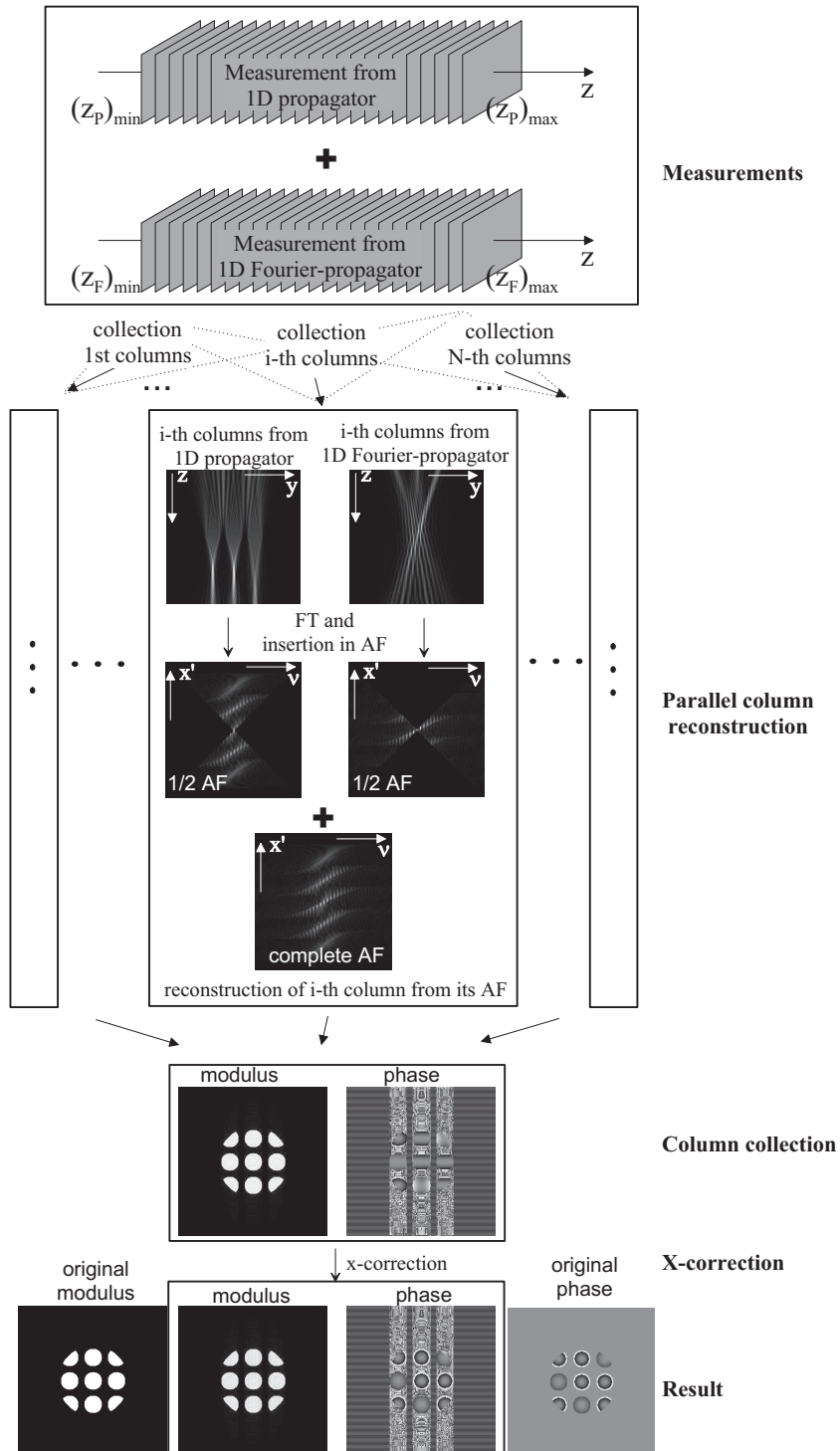


Figure 7.13: Outline of the reconstruction method and a numerical demonstration. Field size: $N = 256$ and $\delta x = 5\mu\text{m}$.

For simplicity, the following description is restricted to one-dimensional signals. In the spatial definition of AF, described in the first line of Eq. 7.1, the shift of x' is symmetrical; therefore, it is denoted as the symmetric definition of AF. By applying the substitution $x'' = x + x'/2$ and renaming $x'' \rightarrow x$, an equivalent asymmetrical definition can be obtained:

$$A(\nu', x'; u) = \int_{-\infty}^{+\infty} u(x)u^*(x - x')e^{-2\pi i x \nu'} dx e^{\pi i x' \nu'}, \quad (7.17)$$

In the following section, this definition will be used during the redundancy investigation. A product function is defined as $F(x, x'; u) = u(x)u^*(x - x')$, which is the inverse Fourier transformation of AF, multiplied by a phase factor $e^{-\pi i x' \nu'}$:

$$F(x, x'; u) = u(x)u^*(x - x') = \int_{-\infty}^{+\infty} A(\nu', x'; u) e^{-\pi i x' \nu'} e^{2\pi i x \nu'} d\nu'. \quad (7.18)$$

The Fourier relationship between A and F is only one-dimensional. Like AF, the product function F has twice the dimensions as its input function u , but the redundancy here is more obvious. For the following, the first variable of product function F , i.e. x is considered a row position, while the second variable, i.e. x' is a column position. Then, the Fourier relation between A and F is row-based. The product function has the following redundancy property,

$$F(x, -x'; u) = F^*(x + x', x'; u), \quad (7.19)$$

where function values in the x, x' - plane can be determined using complex conjugation of function values for appropriately shifted positions. This raises the question concerning the minimum amount of information, required to reconstruct the full F-function. By introducing the sampling width $\delta x'$, which is equal to the sampling width δx of the intensity measurement, i.e. camera resolution, it can be shown, that F can be computed recursively from its first two rows $F(x, 0; u)$ and $F(x, \delta x'; u)$, i.e., all rows $F(x, n\delta x'; u)$ with $n \geq 2$ can be obtained using the following equation:

$$F(x, n\delta x'; u) = \prod_{k=1}^{n-1} \frac{F(x - k\delta x', \delta x'; u)}{F(x - k\delta x', 0; u)} F(x, \delta x'; u). \quad (7.20)$$

This recursion equation requires the term in the denominator, $F(x - k\delta x', 0; u) = u(x - k\delta x')u^*(x - k\delta x')$ to be nonzero for all indices k . If there is a zero in the intensity for some index k , the nominator for this index is also zero, because the nominator term $F(x - k\delta x', \delta x'; u) = u(x - k\delta x')u^*(x - k\delta x' - \delta x')$ contains the same factor.

$F(x - k\delta x', 0; u)$ is effectively the intensity at $z = 0$ shifted by $k\delta x'$. Therefore, utilizing redundancy requires that u is effectively a phase element with amplitude variations being allowed, but amplitude zeros are inadmissible. There is one exception to this restriction: if amplitude is completely zero outside some region, then reconstruction is also possible, since the phase in this region is irrelevant.

With this restriction, the product function F can be reconstructed from two lines. Since each row of AF is a Fourier transformation of the product function with respect to variables x and ν' , the complete AF can also be reconstructed from its first two rows $A(\nu, \delta x'; u)$ and $A(\nu, 0; u)$.

7.4.2 Improving the method based on redundancy properties

Using the 1D propagation operator described in section 7.3.1, the dark blue segments of the ambiguity function in Fig. 7.14 can be obtained using intensity measurements for a set of positions within the range $|z| < \delta x' / (\lambda \delta \nu')$. $\delta \nu'$ is the sampling distance of the ambiguity function in the ν' -direction. By using discrete Fourier transformation methods with N samples, the sampling width is given by $\delta \nu' = 1 / (N \delta x')$. Instead of measuring the bright blue segments in Fig. 7.14 for the range $|z| > \delta x' / (\lambda \delta \nu')$, redundancy of the product function is used. The improved method starts with row $A(\nu', x' = 0; u)$, which, after an inverse Fourier transformation, yields the product function $F(x, x' = 0; u)$. The second required row is $F(x, \delta x'; u)$, which may be obtained through the inverse Fourier transformation of $A(\nu', \delta x'; u)$. One must realize, however, that $A(\nu', \delta x'; u)$ is not completely known, since one value $A(0, \delta x'; u)$ is missing from measurement data. This value corresponds with an intensity measurement for the infinite propagation distance, $z \rightarrow \infty$. In principle, this value could be obtained by applying a 1D optical Fourier operator. In practice, changing the optical setup would affect the reconstruction quality due to alignment errors. Changing the optical setup can be avoided by assessing the missing value from a priori information.

Here, the modified product function $\widehat{F}(x, \delta x'; u)$ at $x' = \delta x'$ is obtained from the Fourier transformation of the first row of AF, where the value $A(0, \delta x'; u)$ at position

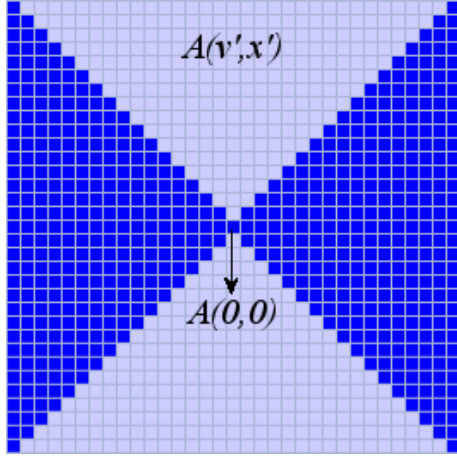


Figure 7.14: Different domains of AF , where the v' -axis is horizontal, while the x' -axis is vertical. The dark blue regions are accessible through intensity measurements for a series of finite propagation distances.

$x = 0$ is set to zero. According to properties for the Fourier transformation, the relationship between the modified product function $\hat{F}(x, \delta x'; u)$ and correct product function $F(x, \delta x'; u)$ is

$$F(x, \delta x) = \hat{F}(x, \delta x) + \frac{A(0, \delta x)}{N}, \quad (7.21)$$

indicating that the two functions only differ in a constant bias. N represents the number of pixels in the row. If the input signal $u(x)$ is limited on space, i.e. $u(x) = 0$ is outside an aperture,

$$u(x) = 0 \quad \text{for} \quad |x| > \frac{W}{2} \quad (7.22)$$

then the product function is also zero outside this aperture:

$$F(x, \delta x) = u(x)u^*(x - \delta x) = 0 \quad \text{for} \quad |x| > \frac{W}{2} \quad (7.23)$$

W is the full width of this aperture. From equations 7.21 and 7.23, it can be concluded that

$$\hat{F}(x_{out}, \delta x : u) = -\frac{A(0, \delta x)}{N} \quad \text{for} \quad x_{out} \in \left\{ x; |x| > \frac{W}{2} \right\}. \quad (7.24)$$

Thus the bias can be obtained from the background value outside the aperture. In a practical situation, this background is usually noisy, and the accuracy of bias can be

improved by statistically averaging the background value using the following equation:

$$A(0, \delta x; u) = -N \left\langle \widehat{F}(x_{out}, \delta x; u) \right\rangle_{x_{out}} . \quad (7.25)$$

Using this additional step, the second row of the product function is known. Now, the procedure demonstrated in section 7.4.1 can be applied to reconstruct the product function. Finally, we can use the Fourier transformation property (Eq. 7.18) to recover AF.

For this method, a total of $2N$ two-dimensional intensity measurements are necessary, which is half the number of measurements compared to the method in section 7.3. The $N - 1$ required sampling positions on the z -axis are given in the following:

$$z_m = \frac{\delta x}{m\lambda\delta\nu} \quad m = -\frac{N}{2} .. \frac{N}{2} - 1, \quad m \neq 0. \quad (7.26)$$

For the line $x' = 0$, one intensity measurement at $z = 0$ is needed. To resolve the unknown phase factors in Eq. 7.7, a second set of N measurements with $u(x, y)$ rotated by 90° are necessary.

7.4.3 Residue minimization algorithm for phase elements

The proposed algorithm computes AF and the complex wave front from a set $2N$ intensity measurements. In any practical situation, measured intensity values are affected by noise due to imperfections in illumination, contaminations in the optical system and camera and quantization noise. This section will illustrate how the second set of N measurements may be utilized to improve reconstruction quality.

As mentioned in the previous section, each column reconstruction is uncertain because of a complex constant factor. To resolve this factor for each column, measurements are repeated by rotating the object by 90° , resulting in another set of N intensity measurements. Although only one row $u(x, y_0)$ at $y = y_0$ is sufficient for determining the unknown constant in each column, all N rows may be used as redundant data to reduce measurement errors.

In the following, $\phi(x, y)$ is referred to as the correct phase function of the complex wave front, $\hat{\phi}^c(x, y)$ as the phase function resulting from column reconstruction with the mentioned unknown constant in each column, and $\hat{\phi}^r(x, y)$ as the phase function

resulting from the row reconstruction with the mentioned unknown constant in each row. For a wave front without phase anomalies, the curl of any gradient must be eliminated. This is equivalent [Bre00] to the presented requirement at the end of section 7.4.1, where the element amplitude is nonzero inside the measurement aperture. Thus, using Stokes' theorem, the contour integral of the phase gradient must be zero:

$$\oint_{\Gamma} \nabla \phi \cdot d\mathbf{r} = \int_A (\nabla \times \nabla \phi) \cdot d\mathbf{A} = 0. \quad (7.27)$$

For the contour integral in Eq. 7.27, an infinitesimal rectangular path Γ with area A is chosen, starting at (x, y) along the points $(x + \delta x, y)$, $(x + \delta x, y + \delta y)$, $(x, y + \delta y)$ and back to (x, y) .

If notations $\phi_{j,k} = \phi(j\delta x, k\delta y)$, and $\widehat{\phi}_{j,k}^r = \widehat{\phi}^r(j\delta x, k\delta y)$ $\widehat{\phi}_{j,k}^c = \widehat{\phi}^c(j\delta x, k\delta y)$ are used for the sampled phase functions, the discrete form of Eq. 7.27 for the correct phase would be:

$$(\phi_{j+1,k} - \phi_{j,k}) + (\phi_{j+1,k+1} - \phi_{j+1,k}) - (\phi_{j+1,k+1} - \phi_{j,k+1}) - (\phi_{j,k+1} - \phi_{j,k}) = 0. \quad (7.28)$$

Due to experimental imperfections, the right hand side of Eq. 7.29 for the measured row and column phase reconstructions is generally not zero, but has a finite residue value of $r_{j,k}$:

$$(\widehat{\phi}_{j+1,k}^r - \widehat{\phi}_{j,k}^r) + (\widehat{\phi}_{j+1,k+1}^c - \widehat{\phi}_{j+1,k}^c) - (\widehat{\phi}_{j+1,k+1}^r - \widehat{\phi}_{j,k+1}^r) - (\widehat{\phi}_{j,k+1}^c - \widehat{\phi}_{j,k}^c) = r_{j,k}. \quad (7.29)$$

To reestablish consistency for these equations, correction terms $\delta\widehat{\phi}_{j,k}^r$, $j \in \{0..N-2\}$ $k \in \{0..N-1\}$ and $\delta\widehat{\phi}_{j,k}^c$, $j \in \{0..N-1\}$ $k \in \{0..N-2\}$ are added to each bracket in Eq. 7.29, resulting in the following equation:

$$\delta\widehat{\phi}_{j,k}^r + \delta\widehat{\phi}_{j+1,k}^c - \delta\widehat{\phi}_{j,k+1}^r - \delta\widehat{\phi}_{j,k}^c = -r_{j,k}. \quad (7.30)$$

Additive correction terms should compensate residues. Applying these corrections to all discrete positions (j, k) $j, k \in \{0..N-2\}$ results in a system of $(N-1)^2$ linear equations

with $2N(N-1)$ unknowns, as given in Eq. 7.31.

$$\underbrace{\left(\begin{array}{c} \overbrace{\begin{matrix} 1 & 0 \cdots 0 & -1 & 0 & \cdots 0 \\ \end{matrix}}^{(N-1)N \text{ elements}} & \overbrace{\begin{matrix} 1 & -1 & 0 \cdots 0 \\ \end{matrix}}^{N(N-1) \text{ elements}} \\ \overbrace{\begin{matrix} 0 & 1 \cdots 0 & 0 & -1 & \cdots 0 \\ \end{matrix}}^{(N-1)N \text{ elements}} & \overbrace{\begin{matrix} 1 & -1 & 0 \cdots 0 \\ \end{matrix}}^{N(N-1) \text{ elements}} \\ \vdots & \vdots \\ \overbrace{\begin{matrix} 0 & 0 \cdots 1 & 0 & 0 & \cdots -1 \\ \end{matrix}}^{(N-1)N \text{ elements}} & \overbrace{\begin{matrix} 1 & -1 & 0 \cdots 0 \\ \end{matrix}}^{N(N-1) \text{ elements}} \\ \overbrace{\begin{matrix} 1 & 0 \cdots 0 & -1 & 0 & \cdots 0 \\ \end{matrix}}^{(N-1)N \text{ elements}} & \overbrace{\begin{matrix} 0 & 1 & -1 \cdots 0 \\ \end{matrix}}^{N(N-1) \text{ elements}} \\ \vdots & \vdots \end{array} \right)}_{\text{Matrix } \mathbf{M}} \underbrace{\left(\begin{array}{c} \delta \widehat{\phi}_{0,0}^r \\ \delta \widehat{\phi}_{1,0}^r \\ \vdots \\ \delta \widehat{\phi}_{N-2,N-1}^r \\ \delta \widehat{\phi}_{0,0}^c \\ \delta \widehat{\phi}_{1,0}^c \\ \vdots \\ \delta \widehat{\phi}_{N-1,N-2}^c \end{array} \right)}_{\text{Vector } \mathbf{c}} = \underbrace{\left(\begin{array}{c} -r_{0,0} \\ -r_{1,0} \\ \vdots \\ -r_{N-2,0} \\ -r_{0,1} \\ \vdots \\ -r_{N-2,N-2} \end{array} \right)}_{\text{Vector } \mathbf{b}} \quad (7.31)$$

Since this system of linear equations (Eq. 7.31) has more unknowns than equations, it is an underdetermined system. This implies that there is not just one unique solution for the correction vector \mathbf{c} , but an entire solution space. Here, the solution vector \mathbf{c} with a minimal Euclidean norm is of more interest. Therefore, singular value decomposition (SVD) is the most appropriate method for solving the problem. For the size of this particular problem, SVD requires a great deal of memory and, consequently, is very slow. Performance can be significantly increased if a regularization technique [GvL96; Gro93] is applied. Eq. 7.31 is reformulated as

$$\begin{bmatrix} \mathbf{M} \\ \lambda \mathbf{I} \end{bmatrix} \mathbf{c} = \begin{bmatrix} \mathbf{b} \\ \mathbf{0} \end{bmatrix}, \quad (7.32)$$

where \mathbf{I} is the identity matrix and λ is a regularization parameter, assumed to be small. Eq. 7.32 is an over-determined system, which can be solved using the pseudo-inverse, resulting in the following least square solution:

$$\min_{\mathbf{c}} \left\{ \left\| \begin{bmatrix} \mathbf{M} \\ \lambda \mathbf{I} \end{bmatrix} \mathbf{c} - \begin{bmatrix} \mathbf{b} \\ \mathbf{0} \end{bmatrix} \right\|_2^2 \right\} \mathbf{c} = \min_{\mathbf{c}} \{ \|\mathbf{M}\mathbf{c} - \mathbf{b}\|_2^2 + \lambda^2 \|\mathbf{c}\|_2^2 \}. \quad (7.33)$$

Although the matrix size increases using regularization, sparse matrix techniques [PTVF92] enable a fast solution. Here, a regularization parameter of $\lambda = 10^{-3}$ is chosen. It has

been discovered that parameters of $\lambda < 10^{-3}$ have no significant effect on the solution. Experimental results applying this residue minimization algorithm are presented in the next section.

7.4.4 Experimental results

To verify the proposed method, a 2D phase-element has been reconstructed, which for reference, can also be measured using an interferometer. The phase-element is a micro lens array with a pitch of $400\mu m$ and a focal length of $30mm$. Additionally, a masking aperture with a diameter of approximately 3×3 lenses is used, as shown in Fig. 7.15. The phase element is illuminated with collimated light from a Helium-Neon-Laser ($\lambda = 632.8nm$). The measurement setup includes the 1D propagation operator. To capture 2D intensity images a SONY B/W CCD camera with 765×576 pixels and a pixel size of $8.6\mu m \times 8.3\mu m$ is used. To realize the 1D propagation for different distances, the CCD camera and the adjacent lens are shifted together in the z direction. The maximal travel path is $|z_P| \leq N \cdot \delta x^2 / \lambda = \pm 6.27cm$ with $N = 576$.

The results of this method with and without the error minimization technique using the residue minimization algorithm are shown in Fig.7.16. Reference measurements obtained with the Mach-Zehnder interferometer have an accuracy of approximately $\lambda/10$. Phase differences shown in Figures 7.16b, Fig.7.16d are calculated as differences between the reconstruction and the interferometer measurements. Without applying the residue minimization algorithm, the root-mean-square (RMS) and peak-to-valley (PV) values of the phase difference are $0.83rad$ (or 0.13λ) and $5.6rad$. By applying the residue minimization algorithm, RMS and PV values are reduced to $0.45rad$ (or 0.07λ) and $3.4rad$. Furthermore, this comparison demonstrates that experimental results are in agreement with interferometer measurements.

7.5 Conclusion

A new method used to reconstruct 2D complex wave fields is presented. This method uses 1D properties of the ambiguity function. Reconstruction operations are performed for one dimension, while the other dimension is considered a series of parallel optical channels. The validity of the new approach is verified through a numerical simulation and also by comparisons made between the simulation and experiment. Based on the

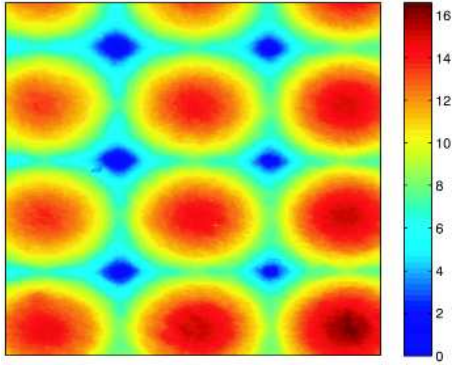


Figure 7.15: *The 2D phase function of the lens-array in rad, measured by an interferometer.*

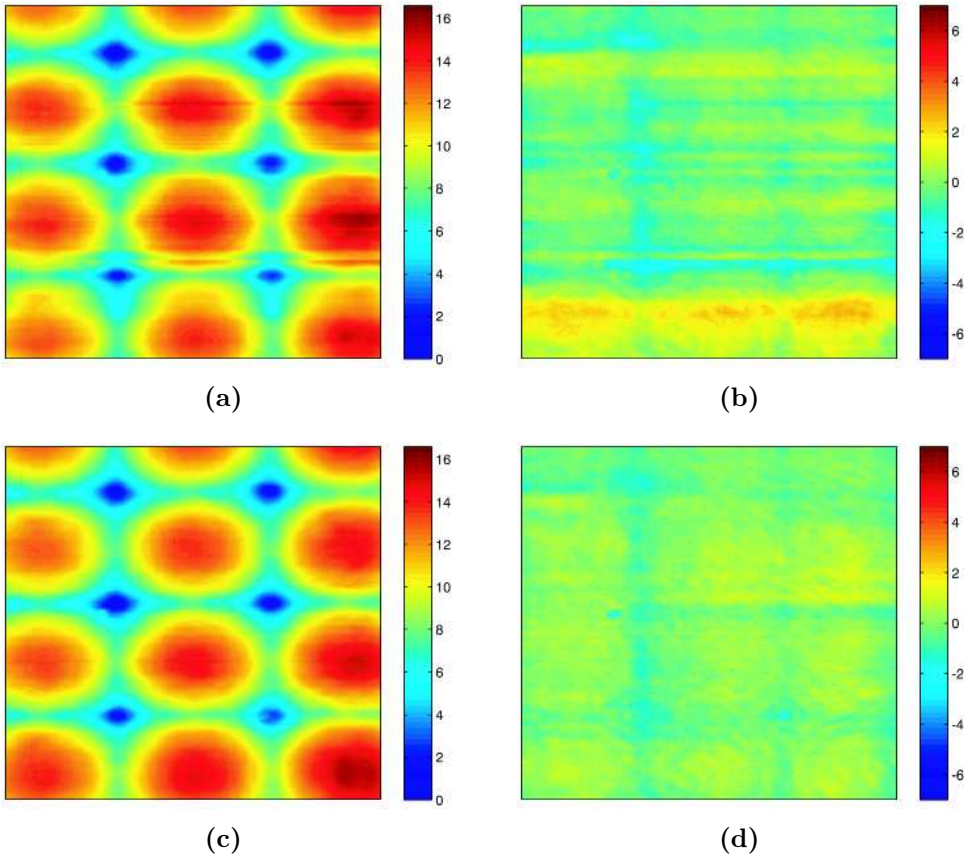


Figure 7.16: *Comparing experimental reconstruction results with and without residue minimization. (a) Reconstructed 2D phase function in rad; (b) Phase difference of (a) to the interferometric measurement in rad; (c) Reconstructed 2D phase function in rad using the residue minimization algorithm; (d) Phase difference of (c) to the interferometric measurement in rad.*

redundancy properties of AF, the number of required measurements has been further reduced. To reduce measurement noise, a residue minimization algorithm is proposed, which has improved experimental results. By applying a regularization technique, the system of equations can be efficiently solved.

Part III

Experimental Results

Chapter 8

Fabricating alignment structures for a fiber resonator in thick resist

This chapter demonstrates an application of lithographic technology in atom optics. A method is presented to mount and align an optical fiber-based resonator on the flat surface of an "atom chip" with ultra high precision. Structures for mounting a pair of fibers, which constitute the fiber resonator are produced by a spin-coated SU-8 photoresist technique using UV deep lithography. The design and production of SU-8 structures are discussed in detail. The quality of these alignment structures and the performance of the fiber resonator will be analyzed in the next chapter using measured finesse.

8.1 Introduction

Although integrated optics is a widespread and important field in today's technology, especially in the telecommunication sector, integrated optics is beginning to gain importance in other areas, including atomic physics and quantum optics [BBDE01]. In the developing field of quantum information processing, the manipulation of neutral atoms with so-called atom chips provides a new, extremely promising approach [FKS⁺02; FKC⁺00]. This concept relies on the capability of controlling magnetically trapped atoms that hover micrometers above a micro-structured surface that carries electric currents and charges to provide the necessary fields. To date, integrated optical access to trapped atoms has not yet been implemented on these atom chips.

There are various types of micro-optical components that have been developed over the past few decades, including photonic crystals, waveguides, and numerous fiber optical devices. Optical fibers are by far the most mature technology for low-loss optical guidance. Using fiber optics, a set of different devices on an atom chip can be built. This chapter gives an easy method for mounting fibers on the chip surface using an epoxy photoresist (SU8) that can form quite thick structures and enable easy positioning and alignment. The following images¹ show examples using the optical fiber to investigate interactions between light and atoms.

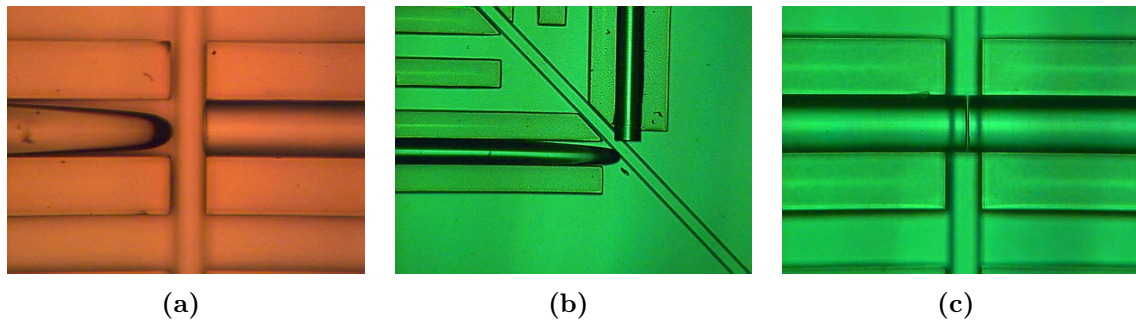


Figure 8.1: *In all three images, SU8 alignment structures adjacent to fibers are visible. (a) A tapered lensed fiber can be used to focus light on very small spot sizes, which can be applied when investigating the fluorescence interaction between light and atoms. (b) Alternative geometry used for fluorescence measurements based on the tapered lens fiber. (c) Two fibers facing each other form an optical cavity to investigate the absorption interaction between light and atoms.*

This chapter concentrates on the third variant, shown in Fig.8.1c, i.e., the absorption interaction between light and atoms. While atoms absorb light, a light beam is significantly attenuated by atoms. When applying this method, even small amounts of atoms can easily be detected. However, this method fails if only one single atom is present. In this case, the attenuation of the light beam is much too small to be measurable. To detect single atoms, the following trick can be used: the atom is placed between two highly reflecting mirrors. These mirrors form an optical resonator, where the light is reflected back and forth. Although the attenuation of the light beam in presence of one atom is small between two consecutive reflections, a large effect results after many reflections. An important step will rest on the on-chip detection of single atoms that can be achieved using an optical fiber resonator [HKH⁺03]. For this approach, fibers are mounted in a

¹These images are from <http://www.physi.uni-heidelberg.de/physi/atph/atomchip2/atomchip?page=CAVc>

superstructure fabricated from an SU-8 resist that provides accurate positioning and alignment. These fibers can easily be inserted by hand and are automatically aligned with sub-micrometer precision.

Developing a fiber resonator is a cooperative project, in which the research groups of Prof. Brenner in Mannheim and Prof. Schmiedmayer at Heidelberg have participated. The main task of the group at Mannheim is to fabricate micro alignment structures on an atom chip used to mount the fiber. Mirror coatings are attached to the fibers using a transfer technique. This step is operated by the group in Heidelberg. The next section will discuss the fabrication process of alignment structures using lithographic technology.

SU-8 is an epoxy-based, chemically amplified solvent-developed negative resist that is typically patterned using 365-436 nm UV aligners. Its specific properties facilitate the production of thick structures with smooth, nearly vertical sidewalls [RPF⁺]. Because of the high mechanical, chemical, and thermal stability of the polymerized SU-8, it is used to fabricate a wide range of micro components, such as optical planar waveguides, for which it achieves outstanding thermal stability and controllable numerical apertures; mechanical parts, such as micro gears for engineering applications; micro fluidic systems and micro reactors for biochemical processing [RPF⁺].

To assess the quality of these alignment structures, the fiber resonator itself is used. Since the finesse of the resonator strongly depends on losses introduced through misalignment, it is a good way of measuring the coupling efficiency and alignment precision of the SU-8 fiber splice.

8.2 Fiber resonator setup

A Fabry-Perot-type fiber resonator setup is sketched in Fig. 8.2(a). It is produced by coupling two pieces of single-mode fibers (with a 4.9 μm mode field diameter) with dielectric mirrors glued to the outer ends of the fibers [WHS⁺06]. A small gap of a few micrometers between the inner ends of the fibers provides access to magnetically trapped atoms that interact with the light field. An important property of a resonator

is its finesse which is written as

$$\mathcal{F} = \frac{\delta\nu}{\Delta\nu} \approx \frac{\pi}{\sum_i \alpha_i}, \quad (8.1)$$

where α_i is the loss factor per single pass, $\delta\nu$ is the free spectral range, and $\Delta\nu$ is the full width at half the maximum of the resonances. This approximation is valid for $\mathcal{F} \gg 1$. For a more detailed description of the resonator theory, one should review textbooks authored by Demtröder [Dem03] and Siegman [Sie86]. For a resonator with a sufficient finesse ($\mathcal{F} > 100$), the additional loss caused by light scattering inside the gap by atoms can be used to detect the presence of even single atoms in the gap [HKH⁺03]. To obtain a high enough finesse, fiber ends must be aligned with sub-micrometer precision.

8.2.1 Intrinsic losses

In the following, all loss mechanisms of the intact fiber resonator are referred to as intrinsic losses, i.e., all losses without introducing the gap. Losses are basically determined by the quality of the glued mirrors at the ends of the fiber. The loss caused by the fiber itself is 3 dB/km, as stated by the manufacturer. With a typical length of $L = 10\text{cm}$ for resonators, this is equivalent to a negligible loss of 0.0003 dB or 0.007 %. In principle, transmission through the mirrors is determined by the properties of the dielectric stack and can be chosen to meet specific requirements. However, the thickness of the glue layer, alignment precision, internal losses, and surface roughness limits the achievable reflectivity. The most important limitation, which cannot be overcome, is the spreading unguided light mode in the glue layer and within the mirror itself. This leads to a reduced coupling of reflected light back into the fiber.

8.2.2 Losses caused by the gap

After cutting the resonator and introducing the gap, the light coupling between the two pieces will be reduced, thus introducing additional loss, resulting from light scattering at the newly introduced surfaces and from transversal, angular, and longitudinal misalignment. The relevant geometric parameters are shown in Fig. 8.2(b). Rotational misalignment converts a potentially imperfect core-cladding concentricity into transversal misalignment [SN79].

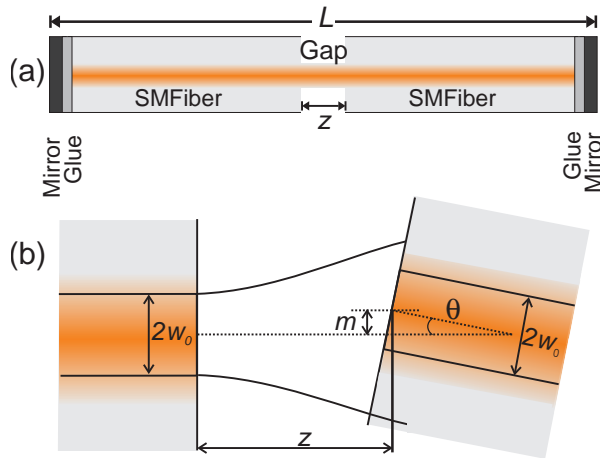


Figure 8.2: (a) Fiber resonator of length L , including a gap of length z . Dielectric mirrors are glued to the outer ends of the resonator. (b) Sketches of possible misalignments at the gap. The mode of diameter $2w_0$ that leaves the first fiber, diverges and is partially coupled into the second fiber, which exhibits a longitudinal displacement z , a transversal displacement m , and an angle misalignment θ .

For a fiber with a single-step refractive index profile, a Gaussian approximation [GT98] for the fundamental mode field distribution can be used. Typically, the Gaussian approximation deviates by less than 1% from the true mode field. In general, the power coupling efficiency of two fibers can be calculated using the overlap integral of the fiber optical field modes. Efficiency decreases quadratically with geometric parameters for slight deviations from perfect alignment. The crucial parameters for efficient light coupling are the transversal misalignment and the angle between the optical axes of two fiber pieces. Because of the weak dependence of the mode field diameter in the near field, coupling loss caused by longitudinal misalignment is not so critical. One must take into account that Fresnel back-reflection at the gap surfaces leads to a coupled system of three resonators. The influence of longitudinal mode symmetry on resonator finesse vanishes for small gap sizes.

8.3 UV deep lithography using SU-8 photoresist

8.3.1 Structural requirements

Alignment structures for the fiber resonator must meet some specific requirements. They must tolerate temperature changes and gradients. In typical experiments with atoms trapped in microscopic potentials, currents carried by metallic structures lead to local temperature increases of as much as 100°C. Furthermore, the structure must be taller than the fiber radius ($r = 67.5 \mu\text{m}$); thus, exposure to a thick resist is needed. To prevent lateral and angular misalignment, i.e., parallel and perpendicular to the sub-

strate plane, an undercut sidewall profile is superior to a vertical sidewall profile. With such a profile, the separation between sidewalls decreases proportionally to the distance from the substrate surface [see Fig. 8.3(c)], thus clamping the fiber. To meet these requirements, SU-8 is highly suitable because of its thermal stability and outstanding lithographic performance. The undercut sidewall profile can be obtained by optimizing the lithographic process steps. The optimization techniques include fine-tuning the exposure dose and post-exposure bake (PEB) time.

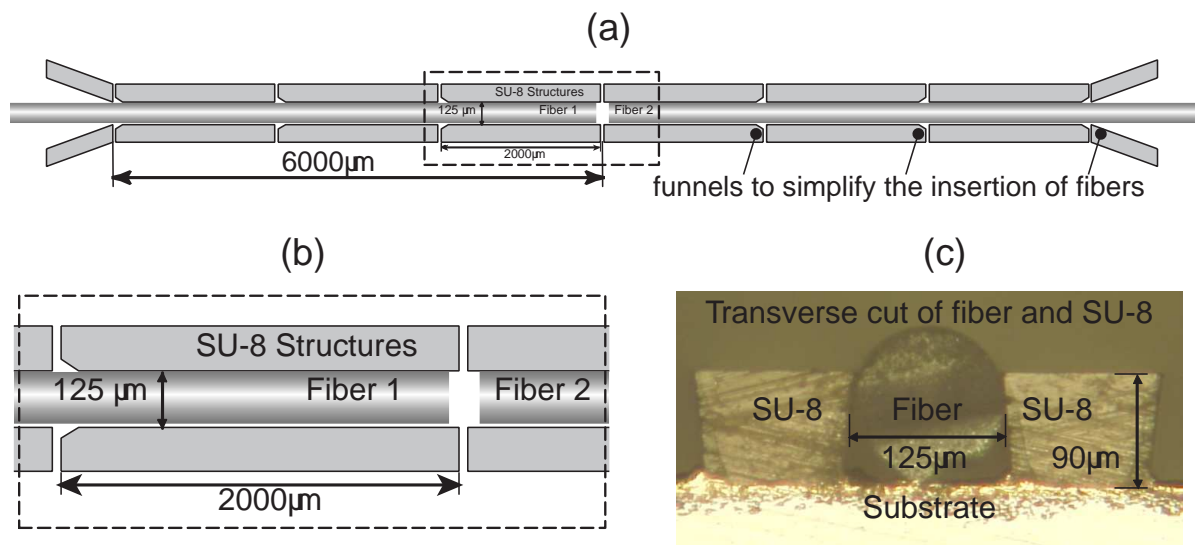


Figure 8.3: (a) Layout of the alignment structure; (b) A magnified part (dotted rectangle); (c) The undercut sidewall profile.

The layout of the desired alignment structure with fibers is shown in Figure 8.3. This design includes funnels to simplify the insertion of the fiber. To avoid angular misalignment, the total length of the alignment structure is chosen as 6000 μm , and it is divided into several sub-segments to reduce stress induced by thermal expansion.

8.3.2 Optimizing the fabrication process

The process for fabricating alignment structures includes substrate coating, soft bake, UV exposure, PEB and development. Each process has a strong influence on the final structure; there are complex interrelations among single process steps. Substrate cleaning and dehydrate baking prior to spin coating can improve SU-8 adhesion. An insufficient soft bake results in mask adhesion and an uneven resist layer. On the other hand, an overly extended soft bake time causes stress and cracking in final structures. The

degree of polymerization is controlled by both the exposure dose and bake conditions. All interrelations increase the complexity of optimization. To accelerate the optimization process, variations are limited to parameters having the strongest influence on final results. Specific to this project, a slight undercut sidewall profile is important and can be optimized by varying the exposure dose and PEB conditions. Compared with PEB conditions, the exposure dose has a stronger influence on the sidewall profile. Therefore, optimization is obtained by varying the exposure dose.

The entire process is described in detail in the following. To improve the adhesion of SU-8 films, gold-coated silicon substrates are cleaned in an ultrasonic bath for five minutes at room temperature. They are then rinsed in distilled water and dehydrated on a hot plate at 200 °C for one hour immediately before use. After cooling to room temperature, approximately three grams of SU-8 50 resist are spread over 5 cm × 5 cm of the substrate's central area. The resist is then spin-coated at 500 rpm for 20 seconds, followed by 2000 rpm for another 20 seconds. This produces an approximately 90 μm thick film. The coated film is then pre-baked on a hot plate in two steps to allow the solvent to evaporate. In the first step, a temperature of 65 °C is used for 10 min. The temperature is then ramped up to 95 °C for approximately six minutes and then held constant at 95 °C for two hours. After cooling to room temperature, the substrate is exposed under the desired mask using a standard 365 nm UV light source. To optimize the undercut sidewall profile, a reduced exposure dose is used. During PEB time, the exposed area of the SU-8 film is selectively polymerized. The post-bake process is also performed in two steps. The substrate is placed on the hot plate at 65 °C for one minute. This step is necessary to avoid an image flow before the resist is slightly polymerized. Then, the substrate is immediately placed on another hot plate at 95 °C for 10 minutes. After PEB, the substrate is removed from the hot plate and cooled to room temperature. Finally, the non-polymerized regions of the SU-8 film are removed in SU-8 developer for 12 minutes. To observe the sidewall profile, the substrate is cut with a precision dicing saw. Microscopic images of sidewall profiles are shown in Fig. 8.4 for different exposure times. Pictures indicate that the degree of the undercut becomes larger with lower exposure doses. This result can be explained by light diffraction at the mask aperture. Because the adhesion of the resist to the substrate decreases with lower exposure doses, a compromise between an acceptable undercut and a sufficient adhesion has been chosen, which corresponds to Fig. 8.4(b).

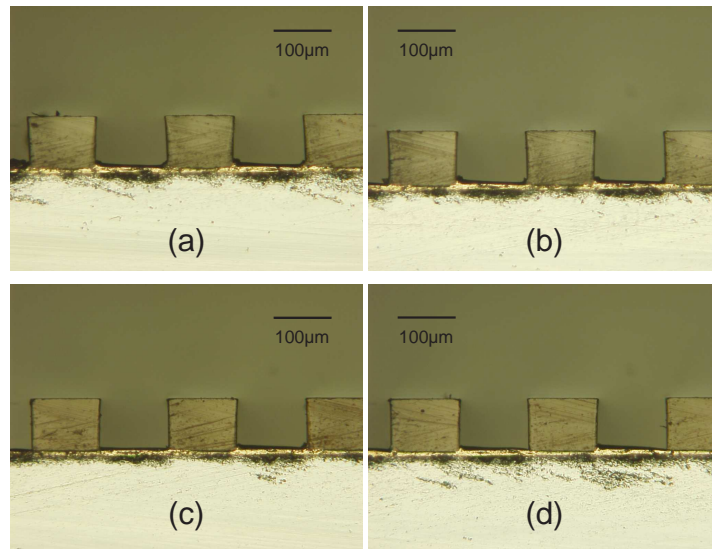


Figure 8.4: *Microscopic images of the cross section of SU-8 structures with increased exposure time from (a) to (d).*

While the finesse of the resonator strongly depends on losses introduced by misalignment, measured finesse is a suitable indicator of the quality of SU-8 alignment structures. In the next chapter, the quality of SU-8 structures will be indirectly determined by the performance of the resonator, i.e., by measured finesse.

Chapter 9

Quality of SU-8 structures and resonator performance

This chapter will show the quality of lithographically fabricated SU-8 alignment structures and the performance of the fiber resonator. While the finesse of the resonator strongly depends on losses introduced through misalignment, measured finesse is a suitable indicator of the quality of SU-8 alignment structures. Measured finesse shows that the coupling loss of SU-8 structures is less than 0.013 dB.

9.1 Building a fiber resonator

Building a fiber resonator and measuring finesse have been completed by the research group in Heidelberg. This section only gives a brief overview of building a fiber resonator. For a detailed explanation, we refer to Wilzbach's thesis [2007].

A piece of single mode fiber with a length of approximately 10 cm is first polished on both ends. The next step is realizing cavity with implanted mirrors on both ends. The mirror coatings are attached to fibers using a transfer technique. In this process, dielectric mirror coatings with a transmittance of 0.1% to 1% are manufactured on a glass substrate. The adhesion between the coating and the glass substrate is fairly low. When the coating is glued to an optical fiber it is possible to transfer the coating from the substrate to the fiber. The transmittance T is near to 1% for cavities with implanted mirrors. A relatively high loss of 1% for cavities with implanted mirrors have several origins, in addition to those caused by the gap. For some cavities, the main intrinsic

loss occurs in the glue layers holding the mirror coatings to the fibers. These glue layers are typically a few micrometers thick. This leads to losses similar to those caused by the gap. Glued mirrors are also sensitive to angular misalignment.

A cavity, similar to that shown in Fig. 8.2a, but without a gap, has been built by inserting two planar mirrors into a fiber with a length of approximately 10 cm. This fiber cavity is subsequently cut into two halves and the new surfaces are polished. An actual cavity of this kind is shown in Fig. 8.1c, where the cavity is mounted on an atom chip using an SU-8 structure to hold the fibers. The drawback of this cavity geometry is that finesse is rather low, mainly because of the fiber gap and glue layers, as described above. Cavities with inserted mirrors typically reach a finesse of a few hundred. Losses due to glue layers can be reduced by directly coating the fiber instead of using the transfer technique. The losses due to the gap itself can also be reduced by introducing collimation optics to the gap, such as a small grin lens or a tapered fiber. Such additional optics will however introduce additional Fresnel reflections and may also require active alignment of the gap.

9.2 Measurement results

The quality of the SU-8 fiber splice is indirectly determined by first measuring the finesse of an intact resonator and then splitting and inserting it into the structures. The transmitted light intensity is recorded while scanning the laser over several free spectral ranges of the fiber resonator. A model function is fitted to the data, yielding the finesse according to Eq. 8.1. The results are averaged over several hundred runs of the experiment. The finesses of two intact resonators are found to be $\mathcal{F}_1 = 110.4 \pm 0.3$ and $\mathcal{F}_2 = 152.8 \pm 1.1$. After cutting the resonators and polishing the surfaces, the pieces are introduced into SU-8 structures. Fiber ends are observed under a microscope and the gap sizes are minimized to touching fibers. Finesses are then measured as $\mathcal{F}_1 = 101.1 \pm 0.5$ and $\mathcal{F}_2 = 132.0 \pm 1.3$, thus giving an additional average loss of $\alpha = (0.29 \pm 0.04)\%$ or (0.013 ± 0.002) dB. Neglecting other additional losses, this corresponds to a pure lateral misalignment of $m = 150$ nm or a pure angular misalignment of $\theta = 6.3 \times 10^{-3}$ rad $\approx 0.36^\circ$. These losses are an upper limit for the SU-8, since many other losses are unaccounted for, including the fiber core-cladding eccentricity or polished fiber facets.

To test thermal stability, the temperature of the substrate varies between 20 and

70°C. The finesse of the inserted fiber resonator shows no change during heating. Another test for the quality of SU-8 structures is a finesse measurement as a function of the gap size. One measurement is done inside the SU-8 structures and one outside the structures. The measurement outside is performed using nano-positioning stages, which in principle can be tuned to a few nanometers. Finesse is optimized when the positioning stages are used. Nevertheless, the finesse obtained inside the SU-8 structures always remains higher than those obtained using the positioning stages. The structures have also allowed long-term stability for a fiber cavity in a high-vacuum environment. The fiber cavity used in the setup keeps its finesse of circa 20 for over one year without realignment. Fig. 9.1 ¹ shows an atom chip holding optical fibers by applying SU8 alignment structures.

9.3 Conclusion

In summary, a method for aligning fibers on a flat surface using SU-8 superstructures has been demonstrated. The aligned fibers represent a Fabry-Perot-type resonator that detects atoms. Different loss mechanisms for this type of fiber resonator have also been investigated. The layout for SU-8 alignment structures has been introduced, which enables easy positioning and alignment. The undercut sidewall profile also offers a method for fixing the fiber. To achieve this structure, the lithographic process is optimized. Furthermore, a technique quantifying losses due to misalignment is demonstrated with the help of the fiber resonator itself. The finesse measurements indicate that the SU-8 superstructures are of superior quality.

¹This image is from <http://www.physi.uni-heidelberg.de/physi/atph/atomchip2/atomchip?page=CAVc>

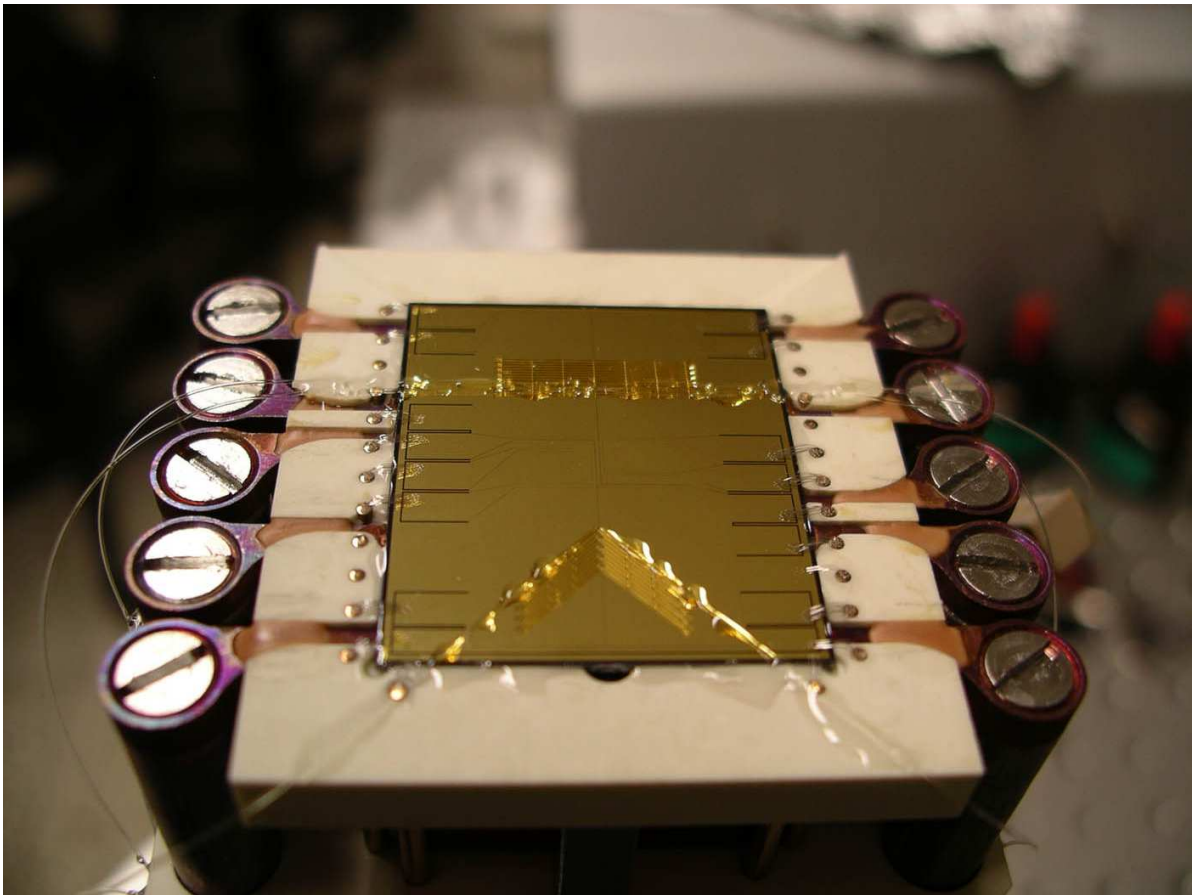


Figure 9.1: *A picture of the atom chip holding optical fibers. The atoms are trapped at the center of the gold surface and can then be transported to regions holding the optical devices. Massive copper structures are used in an initial phase of the experiment to generate the fields needed for the magneto optical trap and large volume magnetic traps.*

Chapter 10

Fabrication of micro lenses using replication techniques

The application in this chapter is an extension of the previous one. In this chapter, the cost-efficient replication technique is applied to fabricate meniscus micro lenses. The meniscus micro lens originated from a plane-convex micro lens-array and is produced through double-sided replication. To enable this, two different replication techniques are used: thermal and ultraviolet (UV) molding processes. After production, a pair of meniscus micro lenses, with facing concave sides, coated with a dielectric mirror, will constitute a micro confocal cavity in the coming application that detects single atoms. The design of the confocal micro cavity and how micro meniscus lenses are produced will be discussed. Replication qualities of thermal and UV-molded structures are examined using an interferometer and compared with the original master.

10.1 Introduction

Increasing requirements for higher speed, performance and interconnected complexity and smaller scale integration makes developments in micro optical components evolutionary. Micro optical components are already widely viewed as not only helpful, but crucial elements in today's technology, especially in integrated optics. Most components include diffractive gratings, micro lenses, and micro prisms. These alone enable a widespread field of optical applications, such as the Hartmann-Shack wavefront sensor in adaptive optics, the Fresnel zone plate in light collimation and the replacement of conventional

optical systems with compact and lightweight planar solutions [BS88; JH89; BKK⁺92].

Replicating polymer materials with techniques such as UV embossing, hot embossing and injection molding is one of most cost-efficient fabrication technologies. In addition to having a very high throughput, equipment required for replication is relatively inexpensive; the replication process is also relatively simple. Because of these advantages, replication technology is not only a significant technology in the IC industry, but is also beginning to gain importance in micro optical applications, such as patterning integrated micro structures.

In the previous chapter, we used a Fabry-Perot type resonator, which is produced by coupling two pieces of single mode fiber ($4.9\mu\text{m}$ mode field diameter) with dielectric mirrors glued to the outer ends of the fibers. A small gap of a few microns between the inner ends of the fibers provided access to magnetically trapped atoms interacting with the light field. Fibers are mounted in a superstructure fabricated from SU-8 resist, providing accurate positioning and alignment. Fibers can easily be inserted "by hand" and are automatically aligned with sub-micron precision. In [WHS⁺06], the finesse of the resonator is inversely proportional to the loss per single pass. Only with a resonator demonstrating sufficient finesse, the additional loss caused by atoms can be used to detect the presence of single atoms. The average finesse from the last approach with SU-8 alignment structures is determined to be 117.

To obtain a higher finesse or detection efficiency, a micro confocal cavity, constituted by two facing concave dielectric mirrors, is used for the next approach. Light coming into the cavity comes from a piece of single mode fiber. To optimize coupling efficiency, the entrance light on the mirror needs a phase front matching the mirror surface, i.e., identical curvatures. To enable this match, light is focused using a convex surface to obtain the desired phase front. After entering into the cavity, light is reflected back and forth. If magnetically trapped atoms are located in the micro cavity, the interaction between light and atoms causes a reduction in light exiting out of the cavity. By doing so, single atoms are detected. For this purpose, two identical meniscus lenses are required. Their concave sides constitute the confocal cavity. One convex side focuses on entrance light to the desired phase front; the other convex side focuses exiting light into another piece of fiber. The following sections specify parameters for such a micro meniscus lens, give details about fabrication processes using hybrid replication techniques and analyse the qualities of a replicated lens-array by comparing them with the original master.

10.2 Micro cavity setup

The micro confocal cavity setup is sketched in Fig. 10.1. In the center of this setup is a micro confocal cavity, consisting of two symmetrically located concave mirrors with a radius curvature of R_c , and free space between the mirrors with the distance of $L_{res} = R_c$. The mode of diameter $2w_0$ that leaves the left single-mode fiber diverges over distance L_{cf} in a vacuum and converges through a spherical convex surface using UV-curable pre-polymers. After further propagating in UV-curable pre-polymers over distance L_a , the light hits the concave mirror and enters into the confocal cavity. The gap between the mirrors provides access to magnetically trapped atoms, which should be detected through interactions between atoms and the light field.

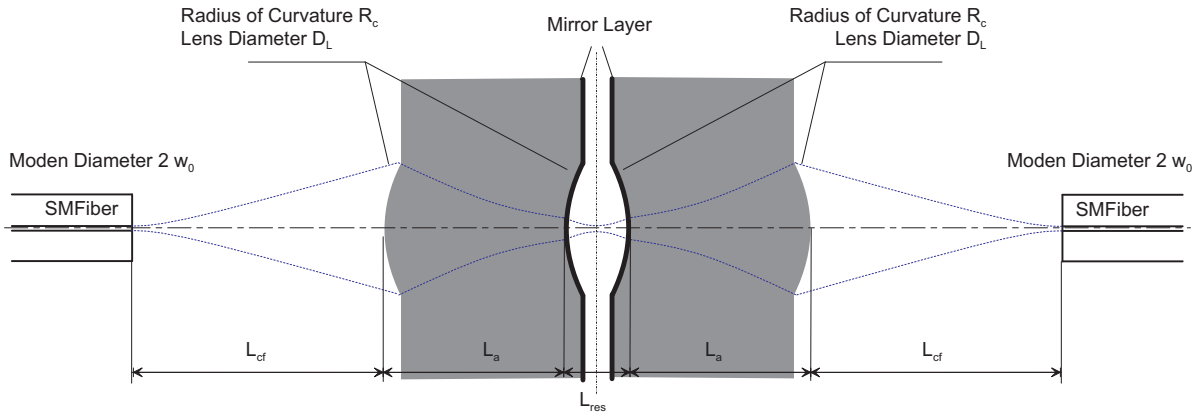


Figure 10.1: *The design configuration of the micro cavity, constructed with two meniscus micro lenses. Here, the lateral amplitude distribution can be perfectly approximated using a Gaussian function; the blue curve indicates the spot size of the Gaussian beam.*

If the wave-front of incoming light on the mirror is parallel to the mirror surface, energy loss due to the refraction on the mirror interface could be minimized. In other words, there will be more light inside the cavity. Furthermore, if the distance between two mirrors is chosen in such a way that the wave-front curvature of light traveling to the right matches the right mirror curvature, there is no light divergence for reflecting light moving back and forth inside the micro confocal cavity. Therefore, the amount of light introduced into the micro cavity remains stable, while the spot size remains small. Consequently, light can be reflected back and forth more times inside the small-sized cavity, keeping the probability of interaction between atoms and light relatively high. The parameters for the micro cavity are determined by matching wave-front curvatures

to mirrors curvatures, which will be discussed in the next section.

10.2.1 Determining all parameters

Before determining all parameters, those primarily fixed by a manufacturer are first given. The single mode optical fiber in use has a mode diameter of $2w_0 = 4.9\mu m$, while the micro lens has a curvature radius of $R_c^{si} = 120\mu m$ and a diameter of $D_L = 95\mu m$, determined by the original stamp used for replication. The cavity length $L_{res} = R_c^{si}$ is fixed by the confocal cavity. With these four fixed parameters, the thickness of micro meniscus lens L_a and distances L_{cf} between the fiber end and the convex spherical surface are determined. As mentioned previously, to obtain a stable and fine light field inside a micro cavity, the curvature of the incoming wave-front on the concave mirror should match the curvature of the mirror.

The light field in a single mode fiber can be perfectly approximated using a rotationally symmetrical Gaussian function. The ABCD law [BK62] is expedient for predicting the parameters of a Gaussian beam exiting from an optical system. A Gaussian beam is characterized by the $1/e$ amplitude spot size w and the phase front radius R^{pf} with superscript pf for a phase-front, distinguished from the curvature radius R^{si} , with superscript si for the spherical interface. Positive R^{pf} means that the center of the phase-front curvature is located in front of the observation point, while the negative R^{pf} means that the center of the phase-front curvature is located behind the observation point. These quantities are combined to form a complex beam parameter q , given as

$$\frac{1}{q} = \frac{1}{R^{pf}} - \frac{i\lambda}{\pi w^2}, \quad (10.1)$$

where λ is the wavelength. As mentioned in Chapter 2, the complex parameter q has another alternative expression:

$$q = z + iz_0. \quad (10.2)$$

Here, $z_0 = \frac{\pi w_0^2}{\lambda}$ is denoted by the Rayleigh range and w_0 by the beam waist, i.e., the smallest spot size. The real part z indicates the location of the beam waist. The definition of its sign is analogous to the sign of the curvature radius; the positive z means that the beam waist is located in front of the observation point, while negative

z means that the beam waist is located behind the observation point. The ABCD-law allows one to trace Gaussian beams through any optical structure for which elements A, B, C, and D of the ray-transfer matrix are known, shown in the following:

$$q_o = \frac{Aq_i + B}{Cq_i + D}, \quad (10.3)$$

with q_i showing the entrance and q_o exit Gaussian beams. The ABCD matrices for symmetrical Gaussian beams are the same as those for ray transfer matrices for 1D optics, discussed in Chapter 2. In this chapter, matrices for thin lenses are not elementary matrices because the micro meniscus lens is relatively thick, compared with its diameter.

Table 10.1: Ray transfer matrices for used optical components.

Element	Matrix	Remarks
Propagation in a medium of a constant refractive index	$\begin{pmatrix} 1 & d \\ 0 & 1 \end{pmatrix}$	$d = \text{distance}$
Refraction on a spherical interface	$\begin{pmatrix} 1 & 0 \\ \frac{n_2 - n_1}{n_2 R^{si}} & \frac{n_1}{n_2} \end{pmatrix}$	$R^{si} = \text{radius of curvature, } R^{si} > 0$ for curvature center before interface; $n_1 = \text{initial refractive index;}$ $n_2 = \text{final refractive index.}$

Table 10.1 lists ray transfer matrices for two elementary optical structures - the propagation in homogeneous media and refractions at spherical interfaces - which will be primarily used at a later time. The curvature of the spherical interface has a positive value if the center of the curvature is before the interface, while curvature of the spherical interface is negative if the center of the curvature follows the interface. This definition agrees with the signs of phase-front and waist location.

As previously mentioned, this section seeks a suitable distance between the fiber end and lens, L_{cf} ; and a suitable thickness for lens L_a , so that the curvature of the incoming phase-front on the concave mirror is equal to the curvature of the concave mirror itself, which is $120\mu m$. If the symmetric construction satisfies these requirements, the curvature of the outgoing phase-front is evidently matched with the curvature of the concave mirror on the right side. The ABCD-matrix of the optical system between the

propagation over L_{cf} and immediately before the first concave mirror is:

$$\begin{pmatrix} A & B \\ C & D \end{pmatrix} = \begin{pmatrix} 1 & L_a \\ 0 & 1 \end{pmatrix} \begin{pmatrix} 1 & 0 \\ \frac{1-n}{n \cdot 120\mu m} & \frac{1}{n} \end{pmatrix} \begin{pmatrix} 1 & L_{cf} \\ 0 & 1 \end{pmatrix}. \quad (10.4)$$

The new curvature radius of phase-front $R^{pf}(L_{cf}, L_a)$ is dependent on L_{cf} and L_a . To find out for which combination (L_{cf}, L_a) the phase-front R^{pf} is equal to $-120\mu m$, mathematics software MathCAD is used. One solution is located on $L_{cf} = 396.8\mu m$ and $L_a = 657.6\mu m$. In practice, these two values are feasible. First, the distance between the fiber end and the micro lens, L_{cf} , is less than the maximal distance, over which the local spot size at the location of the micro lens is still less than the radius of micro lens $D_L/2 = 47.5\mu m$:

$$L_{cf}^{max} = \frac{\pi w_0^2}{\lambda} \sqrt{\left(\frac{D_L}{2w_0}\right)^2 - 1} = 468\mu m. \quad (10.5)$$

Second, even a small deviation from the value $L_a = 657.6\mu m$ creates another matching construction of L_{cf} around $396.8\mu m$. The stability of the operating point will be discussed in detail in the following section.

10.2.2 Investigating the stability of an operating point

So far, all parameters of the micro cavity have been determined. Next, the stability of the chosen operating point $L_{cf} = 396.8\mu m$ and $L_a = 657.6\mu m$ will be investigated. If the thickness of micro lens L_a differs from its desired value, the following study will investigate whether another matched distance between fiber and lens L_{cf} can be found, so that the phase-front of the incoming Gaussian beam is still equal to the curvature radius of the cavity mirror. In Fig. 10.2, the acceptable points are shown near the chosen operating point $L_{cf} = 396.8\mu m$ and $L_a = 657.6\mu m$. This figure shows that even if the thickness of a micro lens varies from its desired value by $\pm 30\mu m$, another suitable alignment for L_{cf} in the range of $390\mu m$ to $407\mu m$ can be found, while the phase-front of an incoming Gaussian beam is still equal to the curvature radius of the cavity mirror. Viewing this aspect, the configuration of $L_a = 657.6\mu m$ is a feasible operating point.

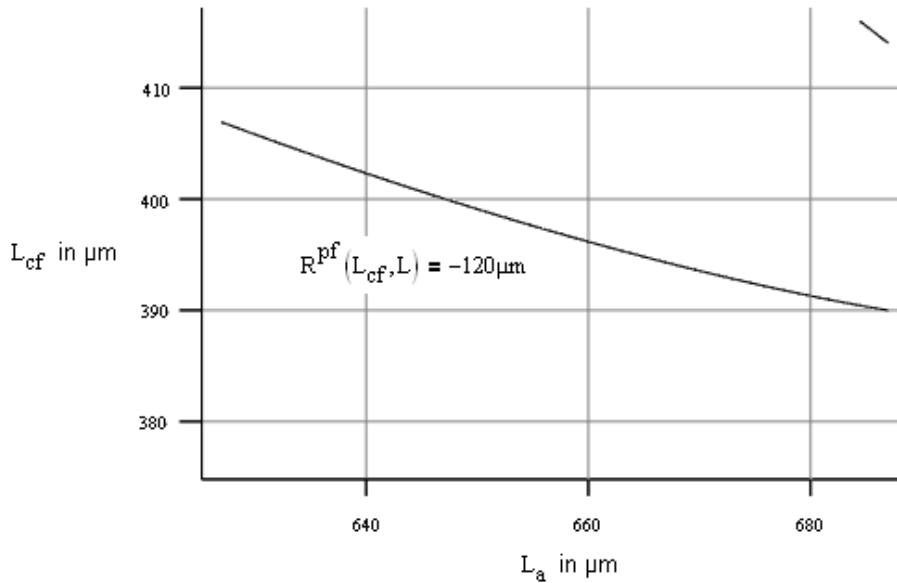


Figure 10.2: Near the chosen operating point $(L_{cf}, L_a) = (396.8 \mu m, 657.6 \mu m)$ are a set of other points on the black curve; the phase-front of an incoming Gaussian beam is matched to the curvature radius of the cavity mirror.

10.3 Fabricating micro lens-array using replication techniques

While micro plane-convex lenses are more commercially available than meniscus lenses or even plane-concave lenses, one micro plane-convex lens array is used as the stamp for double-sided replication. The curvature and diameter of the micro lens are determined by the manufacturer. Since its alignment in the range of $100 \mu m$ is very awkward, a two-dimensional micro-lens array is used instead of a single micro-lens so that one final replicator allows for lenses with little tolerance concerning desired thickness and centered displacement. Using a precision sawing machine, the micro lens-array is cut into two parts around the lenses that have optimal thickness and centered displacement. A 50×50 plane-convex lens-array from Süss Micro Optics Switzerland has been used as the original master; the radius of its curvature is $R = 120 \mu m$, the pitch is $100 \mu m$, and the diameter is $95 \mu m$. Since a negative copy of the lens-array stamp is required to replicate a convex lens-array, two different pre-polymers are applied: a thermally-curable Polydimethylsiloxane (abbr. PDMS) from Dow Corning Co. and a UV-curable polymer (NOA61) from Norland Products, Inc. The advantage of these two polymers is that

they do not stick together. For optimal optical clarity and hardness after curing, the final double-sided lens is manufactured using NOA61. Both thermal and UV replication processes include coating, curing, and releasing, and will be discussed later in detail.

10.3.1 Thermal replication

Fig. 10.3 schematically illustrates the process of thermal replication when forming a negative PDMS copy from a master. The master may be either the original Süss or a NOA61 lens-array. To obtain the desired thickness for the final lens-array, the master is prepared using a predefined spacer. The PDMS and curing agent are mixed using a weight ratio of 10:1. They are then thoroughly stirred to ensure uniformity and then degassed for 90 minutes using a vacuum. The viscous mixture is spread over the master. Afterwards, the pre-polymer is placed in a convection oven at 150°C and cured for 20 minutes. After cooling to room temperature, the PDMS replica containing a

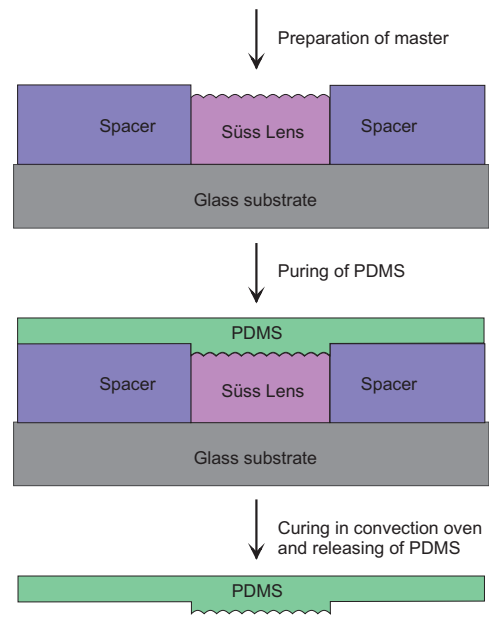


Figure 10.3: The fabrication process of thermal replication.

negative copy of the master can easily be peeled off. The cured PDMS replica can, if necessary, be rinsed with Isopropanol and dried under a gaseous stream of nitrogen.

In order to characterize the quality of the thermal molding process, a negative PDMS replica of the fused silica lens array is made. These two lens arrays are measured using an interferometer. The applied light source of the interferometer has a wavelength of 650nm. The refractive index of a Süss lens is 1.457 at 650nm, while the refractive index of PDMS is 1.4. To enable this comparison, the measured phase of a negative PDMS replica is first scaled using $\frac{n_{quartz}-1}{n_{PDMS}-1}$; and is then inverted. The phase difference in Fig. 10.4 is circa 2rad. Neglecting the tolerated specifications of refractive indices, this phase difference corresponds to a pure height difference of $\Delta h = 453nm$. This height deviation amounts to 5% and is due to the thermal expansion of pre-polymers during the curing process. Roughness in the curves is smaller than 0.3rad, which is below the resolution limit of the interferometer, and can therefore be considered noise.

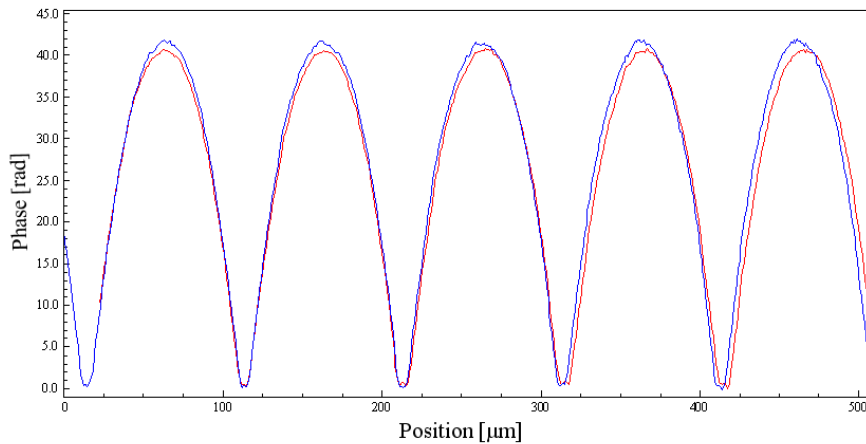


Figure 10.4: Interferometric analysis of fused silica arrays from Süss (blue) and PDMS impressions (red).

10.3.2 UV replication

Fig. 10.5 schematically illustrates the process of UV-replication when forming a negative NOA61 copy from a master, which may be an original Süss lens-array or PDMS lens-array. In the case where the master is a Süss lens-array, the master should be exposed to vapor deposition using an anti-sticking material to prevent NOA61 from sticking to the surface of the fused silica master. The applied anti-sticking material is Tridecafluoro-1,1,2,2-tetrahydrooctyl trichlorosilane. For a PDMS master, treating the surface with an anti-sticking material is not necessary. After applying the optional anti-sticking coating, the master is placed on the viscous prepolymer NOA61 layer, spread on a clean glass substrate. The prepolymer NOA61 is cured using UV light. If the anti-sticking material is applied, it must be checked under a micro-

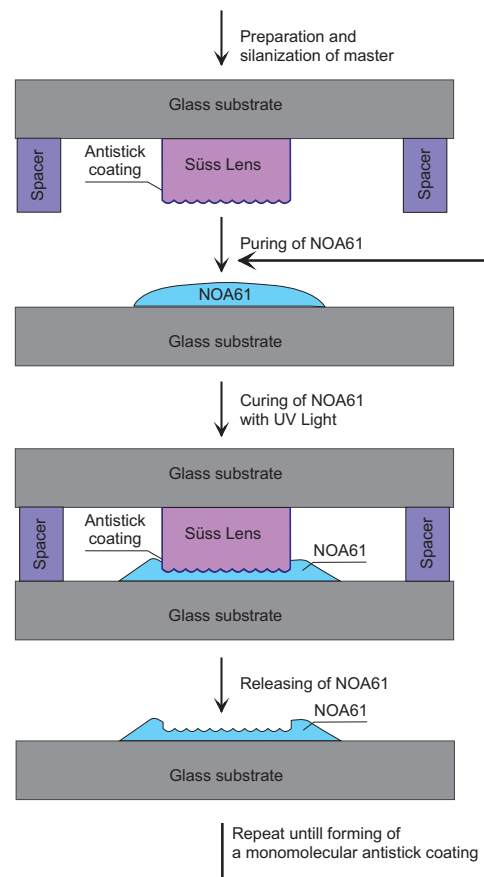


Figure 10.5: The fabrication process of UV-replication.

scope after releasing the NOA61 replica. If a speck of anti-sticking material is detected on the surface of the replica, the process, beginning with the second step listed in Fig. 10.5, must be repeated. Fig. 10.6 shows that after the ninth molding the anti-sticking material forms a homogeneous monolayer.

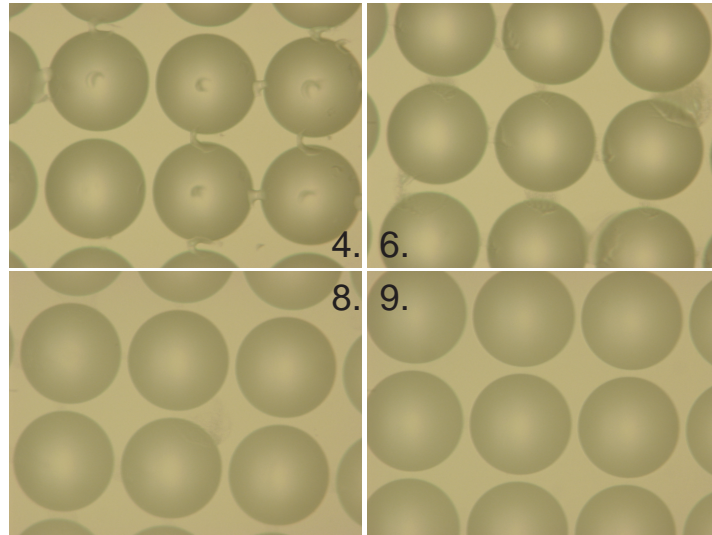


Figure 10.6: Microscopic images from a test series after surface treatment. The black numbers on the images indicate how many replications are indicative after a surface treatment has been performed. It is clear that the surface is more homogeneous with the growing number of replications.

In order to characterize the quality of the UV-molding process, a NOA61 negative replica of the fused silica array is made. Figure 10.7 shows the side view under a microscope after it has been cut into two parts using a precise sawing machine. The spherical surface is slight, but can be clearly seen on the top of the image. None of the same observations are completed for PDMS due to the fact that PDMS melts during the sawing process. The phase-fronts of the master and replica are measured using the same interferometer. To enable a comparison, the phase of PDMS is scaled by $\frac{n_{\text{quartz}}-1}{n_{\text{NOA61}}-1}$, and is then inverted. The refractive index for NOA61 is 1.557. The phase difference in Figure 10.8 is circa 1.2 rad. By neglecting tol-

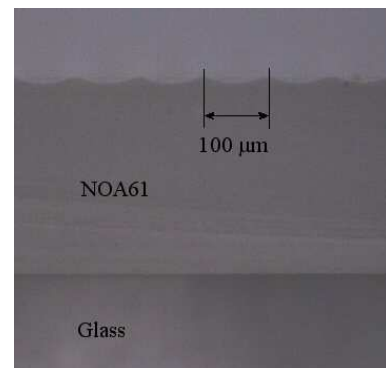


Figure 10.7: The cross-section of the negative NOA61 micro lens-array.

erated specifications of refractive indices, this phase difference corresponds to a pure height difference of $\Delta h = 272nm$. This indicates that the thermal expansion of NOA61, amounting to 3%, is smaller than PDMS. Here, roughness in the curves is also smaller than 0.3rad, which is below the resolution limit of the interferometer, and can therefore be considered noise.

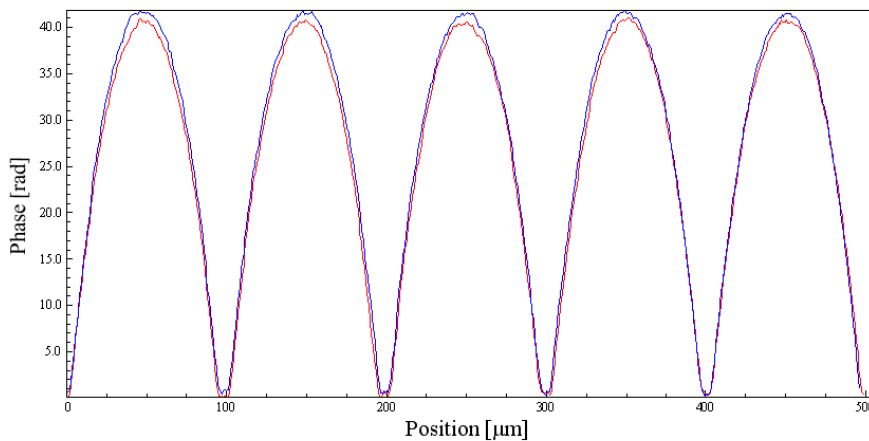


Figure 10.8: *Interferometric analysis of fused silica arrays from Süss (blue) and NOA61 impressions (red).*

The final double-sided micro lens is made from NOA61. The surface roughness of the substrates is extremely important concerning the quality of the dielectric mirror coatings. In order to determine the surface quality of molded arrays, a fused silica and a concave NOA61 array are scanned using an atomic force microscope (AFM). For the original fused silica arrays, the root-mean-squares (RMS) of surface roughness is measured at 2nm. The concave NOA61 array has an RMS surface roughness of 6nm [Wic06].

10.3.3 The entire fabrication process

Figure 10.9 schematically illustrates the entire fabrication process. Using UV-replication, a micro concave NOA61 lens-array is fabricated; the master for this process is the original Süss lens-array. This step uses the previously mentioned anti-sticking coating. After repeating the step nine times, the produced concave NOA61 lens-array is used as the master for the next step - the fabrication of a convex PDMS lens-array. In this step, thermal replication technology is used. The product resulting from this step, the convex

PDMS lens-array, is one master for the last step, the fabrication of a meniscus NOA61 lens-array. The other master of the last step is a concave PDMS lens-array produced using thermal replication technology with the Süß lens-array as its master. The reason two PDMS lens-arrays are used instead of one concave PDMS and original Süß lens-array is to not only prevent damage to the original Süß lens-array, but prevent the need for an anti-sticking coating on the final product. The final step produces the desired

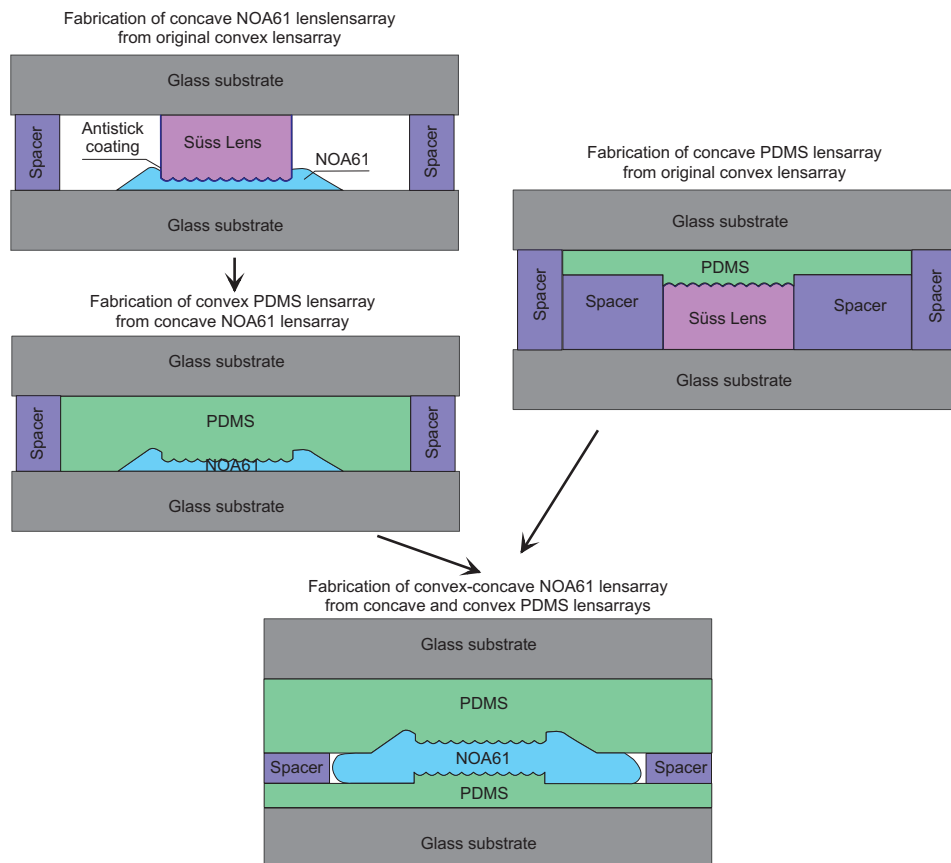


Figure 10.9: The entire flow diagram fabricating the desired meniscus lens-array.

meniscus lens-array from NOA61 using double-sided UV-replication. It is clear that the last spacer determines the thickness of the final lens-array. Spacers used during previous steps are primarily applied to obtain a good planarity of the replica.

10.4 Results

A final meniscus lens-array from NOA61 is shown under a microscope in Fig. 10.10. The side close to the observer is the concave side; the side away from the observer is the convex side. Through one concave lens, one can see a complete convex lens in the middle and four incomplete neighboring convex lenses.

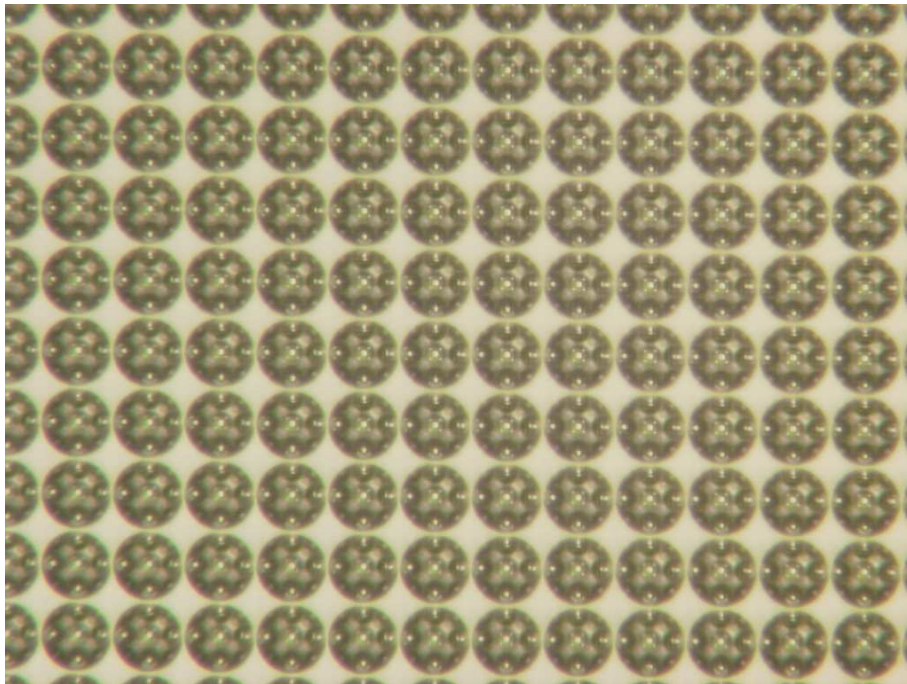


Figure 10.10: *The image of the meniscus NOA61 lens-array under a microscope. Large circle: concave side. Small circle: convex side.*

The observed downsizing of a convex lens-array through the concave lens can best be understood by viewing Fig. 10.11. The concave surface performs as a diverging lens with a focal length of $f' = (n_{NOA61} - 1)/R^{si} = 218\mu m$ and constitutes an imaging system with the convex surface serving as an object. The refractive index of NOA61 at the wavelength for illumination is 1.55 as stated by the manufacturer. The convex surface is placed at $658\mu m$. According to the lens formula, the image is virtual and located at $326\mu m$ on the same side of the lens as the object. Magnification is given as $326/658 \approx 0.5$.

After the meniscus lens-array with appropriate geometries has been constructed, applying the mirror coatings on NOA61 is the next crucial step. This is managed by the partner group in Heidelberg. Because of NOA61's relatively low flaming point, the

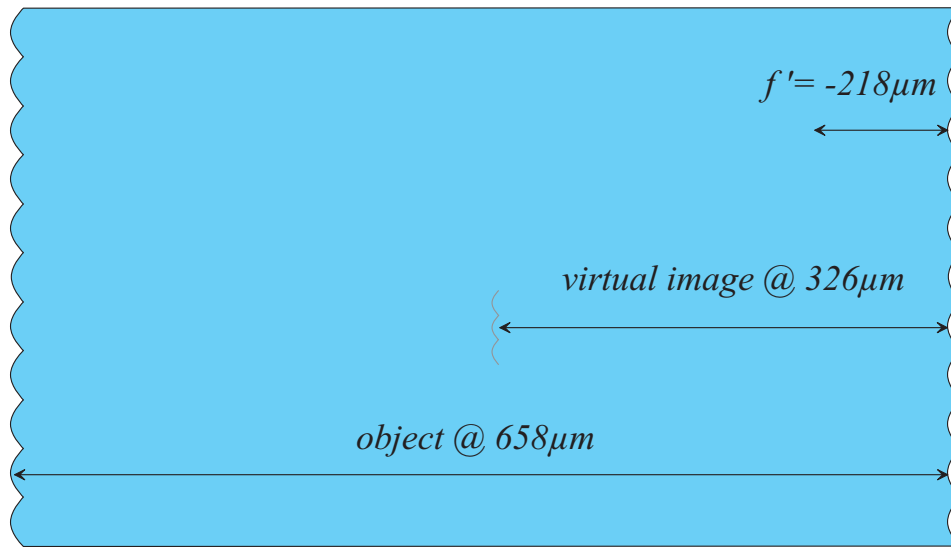


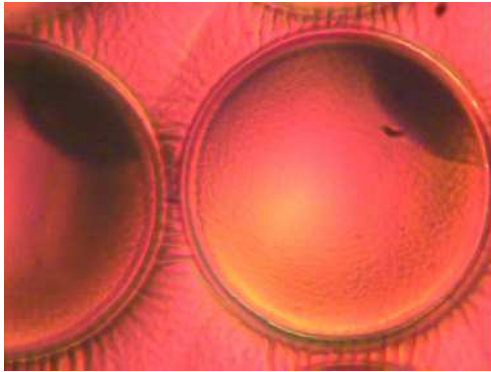
Figure 10.11: The configuration of an imaging system determines the downsizing of the convex side: the concave side is the object; while the convex side is serving as the imaging lens.

substrates must to be coated with an ion beam sputtering. The general compatibility between the polymer and coating has been verified during the test-run in order to confirm that the coatings would actually remain on the polymer.

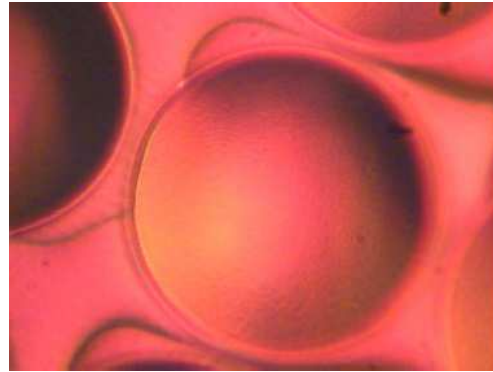
During experimentation, the final coating process is successful (Fig. 10.12). Most concave lenses are homogeneously coated. Under the microscope, some lenses exhibit wavy, rippled patterns in the coating. This is probably caused by very high surface tension, which is an unavoidable side-effect of ion beam sputter coating. Fortunately, the majority of lenses do not show these patterns in the coating and should prove usable. However, most lenses show a much finer, "orange peel" texture in the coating. Whether this affects the final reflectivity of these mirrors or not must be determined from actual cavity finesse measurements. The measurement of finesse will be completed by the group in Heidelberg. Unfortunately, these results will not be available until the delivery of this dissertation.

10.5 Conclusion

In summary, the ABCD-law is applied to determine the parameters of a micro confocal cavity. The micro cavity is constituted using two facing concave spherical surfaces



(a) Some lenses exhibit a strongly rippled coating. This is probably caused by high surface tensions which can not be avoided during IBS coating processes.



(b) Most lenses are largely homogeneous. Some lenses still exhibit a finely rippled, "orange peel", surface, which may also have been caused by surface tension.

Figure 10.12: These images show a view of the mirror-coated concave lenses [Wic06].

and will be used in atomic physics to detect single atoms. Two different cost-efficient replication technologies have been analyzed. Together, they enable the fabrication of a micro meniscus lens array from one plane-convex lens array. Two concave sides constitute the micro confocal cavity. The convex side focuses incoming light so that its phase-front is matched to the concave surface, which provides a high interaction probability between atoms and light.

Part IV

Conclusion

Chapter 11

Summary and perspectives

Summary

This thesis has focused on micro optics and deep lithography - key components and technology for many multidisciplinary applications. The main topics aim at solving particular problems facing these areas of research that have not been intensively discussed in other publications.

In a cooperative research project with the University of Heidelberg, an application of lithography technology in atom optics is introduced. A method to mount and align an optical fiber-based resonator on the flat surface of an "atom chip" with ultra high precision is presented. Structures for mounting a pair of fibers, constituting the fiber resonator, are produced with a spin-coated SU-8 photoresist technique using UV deep lithography. The design and production of SU-8 structures are discussed. Using measured finesse, the coupling loss of SU-8 structures acting as a kind of fiber splice are calculated as less than 0.013 dB. In the next improved approach, the ABCD-law for Gaussian beams is used to design a micro optical cavity constituted by two micro lenses. The micro cavity is also built into an atom chip to improve detection efficiency due to its high theoretical finesse. Micro lenses are fabricated using cost-efficient replication technology.

In Part II, a design tool is first given to solve the problem of synthesizing a minimal optical system consisting only of thin lenses and free spaces for a given ray-transfer matrix. These optical systems are not only one-dimensional but two-dimensional as well. Similar syntheses have been previously studied in some publications, but have lacked an attempt at minimality.

Modeling scalar mask diffraction in thick resist is then concerned with three special aspects of light propagation: energy investigation in scalar fields, mask diffraction in absorbing media and mask diffraction with spatially incoherent illumination. All aspects are key points for correctly modeling scalar mask diffraction. Due to the fact that the energy calculation for a scalar field is crucial when modeling scalar mask diffraction and most scalar theories require a square modulus to determine local energy flow, a conflict is observed in that energy flow must be a vector, but the square modulus is only a scalar. Consequently, this study attempts at deducing a proper definition for local energy flow using Maxwell's equations and giving a reason why the square modulus is commonly applied to energy calculations. Diverse diffraction theories are taken into consideration when deducing the definition of local energy flow.

When studying absorption, the Beer-Lambert law is often applied, however, it is insufficient for acquiring three-dimensional light distribution. This thesis shows how conventional plane wave expansion can be modified and then applied to the investigation of scalar mask diffraction in absorbing photoresists. While the most commonly used incoherent light propagations focus on the image plane, incoherent mask diffraction introduced in this thesis enables the acquisition of complete three-dimensional light distribution behind a mask. To support incoherent mask diffraction, a very simple setup has been developed to characterize the spatial incoherence of an illumination source.

An efficient tomographic method is then introduced that recovers two-dimensional complex amplitudes. This method does not need a reference wave and has been extensively demonstrated for one-dimensional amplitudes, while for two-dimensional amplitudes, it poses several problems owing to data acquisition. One potential application of this method is characterizing the wave front where no reference is available, for example, characterizing the light field from a laser-diode. Two helpful one-dimensional optical operators have been developed as necessary components for this method. Using them, one-dimensional propagations and Fourier transformations can be achieved. A residue minimizing algorithm, which improves experimental results, could certainly be applied for other phase retrieval methods.

Finally, the quality of alignment structures for the fiber resonator is given through the performance of the resonator, i.e. measured finesse. Additionally, the quality of the replicated micro lenses is interferometrically measured.

Perspectives

When modeling the lithographic process, there are other interesting topics not discussed in this thesis. In the IC industry, increasing the integration grade demands a reduction in the structure size. For structures with sub-wavelength apertures, polarization has a strong impact on exposure qualities. A rigorous coupled wave analysis, a finite difference time domain method, and a finite element method are classic vectorial methods for analyzing polarization effects. The main problem with these methods is the high calculation time. Improving efficiency is the actual key aspect in this area.

Another interesting aspect is the adequate modeling of the development process, used to simulate how the resist would dissolve in a developer solution, based on dissolution rate information. To do so, there are two main approaches: ray-tracing methods and cellular automata methods. Ray-tracing methods treat the progression of the resist-developer interface analogous to an optical wave front propagating through a thick inhomogeneous medium.

In order to simulate the complete lithographic process, a substantial empirical study is an inevitable step for discovering characteristics of photoresists, including a refractive index, the shrinkage factor, absorption length, dissolution rate, etc.

Part V

Appendix

Appendix A

Helpful rules for decomposing 4×4 symplectic matrices

A.1 Combining rotation matrices

Coordinate rotation implies rotating the local lateral coordinate system. For practical realization, this merely requires the rotation of the next physical component. Therefore, it is not considered an optical operation. Successive rotation matrices can be condensed to one rotation with an angle parameter of φ_{total} , given as the sum of successive rotation matrices. Another useful feature of rotation matrices is $\mathbf{R}(-\varphi) = \mathbf{R}^T(\varphi) = \mathbf{R}^{-1}(\varphi)$.

A.2 Interchanging isotropic propagation and rotation

The isotropic propagation operator $\mathbf{P}(z, z)$ commutes with coordinate rotation, i.e. $\mathbf{P}(z, z) \cdot \mathbf{R} = \mathbf{R} \cdot \mathbf{P}(z, z)$.

A.3 Simplifying two generalized lenses with intermediate rotation

Because of the structure of the matrix of a generalized lens, it is simple to show how

successive generalized lenses can be combined to form a new generalized lens:

$$\mathbf{L}_2^g \cdot \mathbf{L}_1^g = \begin{pmatrix} \mathbf{I} & \mathbf{0} \\ \mathbf{G}_2 & \mathbf{I} \end{pmatrix} \begin{pmatrix} \mathbf{I} & \mathbf{0} \\ \mathbf{G}_1 & \mathbf{I} \end{pmatrix} = \begin{pmatrix} \mathbf{I} & \mathbf{0} \\ \mathbf{G}_1 + \mathbf{G}_2 & \mathbf{I} \end{pmatrix} = \mathbf{L}^g. \quad (\text{A.1})$$

The following equation demonstrates the more general case of two generalized lenses separated by a rotation matrix $\mathbf{R}(\varphi)$. In this case, they can be combined into one generalized lens and rotation $\mathbf{R}(\varphi)$:

$$\begin{aligned} \mathbf{L}_2^g \mathbf{R}(\varphi) \mathbf{L}_1^g &= \underbrace{\mathbf{R}(-\varphi_1) \mathbf{L}(f_{1x}, f_{2y}) \mathbf{R}(\varphi_1)}_{\text{factoring of } \mathbf{L}_2^g \text{ as A7}} \mathbf{R}(\varphi) \mathbf{L}_1^g \\ &= \mathbf{R}(\varphi) \underbrace{\mathbf{R}(-\varphi_1 - \varphi) \mathbf{L}(f_{1x}, f_{2y}) \mathbf{R}(\varphi_1 + \varphi)}_{\mathbf{L}_2^g} \mathbf{L}_1^g \\ &= \mathbf{R}(\varphi) \mathbf{L}_2^g \mathbf{L}_1^g \\ &= \mathbf{R}(\varphi) \mathbf{L}_3^g \text{ or } \mathbf{L}_3^g \mathbf{R}(\varphi). \end{aligned} \quad (\text{A.2})$$

This rule of combination is important and frequently used for minimal decomposition, discussed in Section 2.3.3.

A.4 Simplifying two generalized propagations with intermediate rotation

Because of the structure of the matrix of a generalized propagation, it is simple to demonstrate how successive generalized propagations can be combined to form a new generalized propagation:

$$\mathbf{P}_2^g \cdot \mathbf{P}_1^g = \begin{pmatrix} \mathbf{I} & \mathbf{H}_2 \\ \mathbf{0} & \mathbf{I} \end{pmatrix} \begin{pmatrix} \mathbf{I} & \mathbf{H}_1 \\ \mathbf{0} & \mathbf{I} \end{pmatrix} = \begin{pmatrix} \mathbf{I} & \mathbf{H}_1 + \mathbf{H}_2 \\ \mathbf{0} & \mathbf{I} \end{pmatrix} = \mathbf{P}^g. \quad (\text{A.3})$$

The following considers the more general case of two generalized propagations separated by a rotation matrix $\mathbf{R}(\varphi)$. In this case, they can be combined into one generalized

propagation and rotation $\mathbf{R}(\varphi)$:

$$\begin{aligned}
\mathbf{P}_2^g \mathbf{R}(\varphi) \mathbf{P}_1^g &= \underbrace{\mathbf{R}(-\varphi_1) \mathbf{P}(z_{1x}, z_{2y}) \mathbf{R}(\varphi_1)}_{\text{factoring of } \mathbf{P}_2^g \text{ as A8}} \mathbf{R}(\varphi) \mathbf{P}_1^g \\
&= \mathbf{R}(\varphi) \underbrace{\mathbf{R}(-\varphi_1 - \varphi) \mathbf{P}(z_{1x}, z_{2y}) \mathbf{R}(\varphi_1 + \varphi)}_{\mathbf{P}_2'^g} \mathbf{P}_1^g \\
&= \mathbf{R}(\varphi) \mathbf{P}_2'^g \mathbf{P}_1^g \\
&= \mathbf{R}(\varphi) \mathbf{P}_3^g \text{ or } \mathbf{P}_3^g \mathbf{R}(\varphi). \tag{A.4}
\end{aligned}$$

This rule of combination is important and frequently used for minimal decomposition, discussed in Section 2.3.3.

A.5 Transforming a general symplectic matrix to matrix with a symmetric sub-matrix

A matrix transformation, frequently used in Chapter 2, concerns transforming a general symplectic matrix to matrix with a symmetric sub-matrix using a rotation matrix. The following example transforms sub-matrix \mathbf{B} to a new symmetric matrix \mathbf{B}' ; the required rotation matrix is given as the following:

$$\begin{pmatrix} \mathbf{A}' & \mathbf{B}' \\ \mathbf{C}' & \mathbf{D}' \end{pmatrix} = \begin{pmatrix} \mathbf{A} & \mathbf{B} \\ \mathbf{C} & \mathbf{D} \end{pmatrix} \cdot \mathbf{R}(\varphi_1), \tag{A.5}$$

$$\text{with } \mathbf{B} = \begin{pmatrix} b_{11} & b_{12} \\ b_{21} & b_{22} \end{pmatrix}, \varphi_1 = \arctan\left(\frac{b_{21} - b_{12}}{b_{11} + b_{22}}\right), \mathbf{B}'^T = \mathbf{B}'.$$

The tangent function has a period of π . Therefore, the rotation matrix with angle $\pi + \varphi_1$ is another solution that transform \mathbf{B} to a symmetric matrix. When compared with Eq. A.5, all sub-matrices have a negative sign:

$$\begin{pmatrix} -\mathbf{A}' & -\mathbf{B}' \\ -\mathbf{C}' & -\mathbf{D}' \end{pmatrix} = \begin{pmatrix} \mathbf{A} & \mathbf{B} \\ \mathbf{C} & \mathbf{D} \end{pmatrix} \cdot \mathbf{R}(\pi + \varphi_1), \text{ with } -\mathbf{B}'^T = -\mathbf{B}'. \tag{A.6}$$

Using the rotation matrix property, the following can be written:

$$\begin{pmatrix} \mathbf{A} & \mathbf{B} \\ \mathbf{C} & \mathbf{D} \end{pmatrix} = \begin{pmatrix} \mathbf{A}' & \mathbf{B}' \\ \mathbf{C}' & \mathbf{D}' \end{pmatrix} \cdot \mathbf{R}(-\varphi_1). \quad (\text{A.7})$$

The conversion of \mathbf{B} to a symmetric matrix can also be realized using a left multiplication with a rotation. The calculation is similar and will not be discussed in detail. If sub-matrix \mathbf{B} is symmetric, the angle φ_1 will be zero; thus, the rotation matrix is the identity matrix. If the concerned sub-matrix is \mathbf{A} , \mathbf{C} or \mathbf{D} , these transformations are similar with the only difference being that the angle of the rotation matrix is calculated using entries from the concerned sub-matrix.

A.6 Transforming a symplectic matrix to matrix with a diagonal sub-matrix

Another frequently used operation is transforming a symmetric 2×2 sub-matrix into a diagonal matrix. The symmetric sub-matrix \mathbf{B}' from Eq. A.5 is used here as an example. By using one rotation matrix and its transposition, the symmetric sub-matrix \mathbf{B}' can be transformed into a diagonal matrix \mathbf{B}'' :

$$\begin{pmatrix} \mathbf{A}'' & \mathbf{B}'' \\ \mathbf{C}'' & \mathbf{D}'' \end{pmatrix} = \mathbf{R}^T(\varphi_2) \cdot \begin{pmatrix} \mathbf{A}' & \mathbf{B}' \\ \mathbf{C}' & \mathbf{D}' \end{pmatrix} \cdot \mathbf{R}(\varphi_2), \quad (\text{A.8})$$

with $\mathbf{B}' = \begin{pmatrix} b'_{11} & b' \\ b' & b'_{22} \end{pmatrix}$, $\mathbf{B}'' = \begin{pmatrix} b''_{11} & 0 \\ 0 & b''_{22} \end{pmatrix}$, $\varphi_2 = \frac{1}{2} \arctan\left(\frac{2b'}{b'_{22} - b'_{11}}\right)$.

Consequently, if the two transformations in equations A.5 and A.8 are combined, an arbitrary 2×2 sub-matrix can be transformed into a diagonal matrix using the two

following rotation matrices:

$$\begin{pmatrix} \mathbf{A}'' & \mathbf{B}'' \\ \mathbf{C}'' & \mathbf{D}'' \end{pmatrix} = \mathbf{R}(\beta) \cdot \begin{pmatrix} \mathbf{A} & \mathbf{B} \\ \mathbf{C} & \mathbf{D} \end{pmatrix} \cdot \mathbf{R}(\alpha) \quad (\text{A.9})$$

$$\text{with } \mathbf{B} = \begin{pmatrix} b_{11} & b_{12} \\ b_{21} & b_{22} \end{pmatrix} \quad \mathbf{B}'' = \begin{pmatrix} b''_{11} & 0 \\ 0 & b''_{22} \end{pmatrix}$$

$$\beta = \frac{1}{2} \left[\arctan \left(\frac{b_{21}-b_{12}}{b_{11}+b_{22}} \right) - \arctan \left(\frac{b_{12}+b_{21}}{b_{22}-b_{11}} \right) \right]$$

$$\alpha = \frac{1}{2} \left[\arctan \left(\frac{b_{12}+b_{21}}{b_{22}-b_{11}} \right) + \arctan \left(\frac{b_{21}-b_{12}}{b_{11}+b_{22}} \right) \right] .$$

If sub-matrix \mathbf{B} is a zero matrix, angles α and β equal zero. Using the property of a rotation matrix, the following can also be written:

$$\begin{pmatrix} \mathbf{A} & \mathbf{B} \\ \mathbf{C} & \mathbf{D} \end{pmatrix} = \mathbf{R}(-\beta) \cdot \begin{pmatrix} \mathbf{A}'' & \mathbf{B}'' \\ \mathbf{C}'' & \mathbf{D}'' \end{pmatrix} \cdot \mathbf{R}(-\alpha). \quad (\text{A.10})$$

A.7 Factorizing a generalized lens matrix

If the given ABCD-matrix has a symmetric left bottom sub-matrix, it can be identified as a generalized astigmatic lens. In this case, it can be decomposed into two rotation matrices with one intermediate astigmatic lens:

$$\begin{pmatrix} \mathbf{I} & \mathbf{0} \\ \mathbf{G} & \mathbf{I} \end{pmatrix} = \mathbf{R}(-\varphi) \mathbf{L}(f_x, f_y) \mathbf{R}(\varphi), \quad \text{with } \mathbf{G}^T = \mathbf{G} = \begin{pmatrix} g_{11} & g \\ g & g_{22} \end{pmatrix}. \quad (\text{A.11})$$

To obtain these parameters, rule R6 is used for the following:

$$\varphi = \frac{1}{2} \arctan \left(\frac{2g}{g_{11}-g_{22}} \right) \quad (\text{A.12})$$

$$f_x = \frac{-1}{g_{11} \cos^2 \varphi + g_{22} \sin^2 \varphi + g \sin(2\varphi)} \quad (\text{A.13})$$

$$f_y = \frac{-1}{g_{11} \sin^2 \varphi + g_{22} \cos^2 \varphi - g \sin(2\varphi)}. \quad (\text{A.14})$$

A.8 Factorizing a generalized propagation matrix

If the given ABCD-matrix has a symmetric right top sub-matrix, it can be identified as a generalized anisotropic propagation. In this case, it can be decomposed into two rotation matrices with an intermediate anisotropic propagation:

$$\begin{pmatrix} \mathbf{I} & \mathbf{H} \\ \mathbf{0} & \mathbf{I} \end{pmatrix} = \mathbf{R}(-\varphi)\mathbf{P}(z_x, z_y)\mathbf{R}(\varphi), \text{ with } \mathbf{H}^T = \mathbf{H} = \begin{pmatrix} h_{11} & h \\ h & h_{22} \end{pmatrix}. \quad (\text{A.15})$$

To obtain these parameters, rule R6 is used to obtain the following:

$$\varphi = \frac{1}{2} \arctan\left(\frac{2h}{h_{11}-h_{22}}\right) \quad (\text{A.16})$$

$$z_x = h_{11} \cos^2 \varphi + h_{22} \sin^2 \varphi + h \sin(2\varphi) \quad (\text{A.17})$$

$$z_y = h_{11} \sin^2 \varphi + h_{22} \cos^2 \varphi - h \sin(2\varphi). \quad (\text{A.18})$$

A.9 Factorizing a generalized scale matrix

If the given ABCD-matrix has the form of a block diagonal matrix, it can be identified as a generalized anisotropic propagation. In this case, it can be decomposed into two rotation matrices with an intermediate anisotropic propagation:

$$\begin{pmatrix} \mathbf{A} & \mathbf{0} \\ \mathbf{0} & \mathbf{A}^{T^{-1}} \end{pmatrix} = \mathbf{R}(\beta)\mathbf{S}(m_x, m_y)\mathbf{R}(\alpha), \text{ with } \mathbf{A} = \begin{pmatrix} a_{11} & a_{12} \\ a_{21} & a_{22} \end{pmatrix}. \quad (\text{A.19})$$

To obtain these parameters, rule R6 is used for the following:

$$\alpha = \frac{1}{2} \left[\arctan\left(\frac{a_{12}+a_{21}}{a_{11}-a_{22}}\right) + \arctan\left(\frac{a_{12}-a_{21}}{a_{11}+a_{22}}\right) \right] \quad (\text{A.20})$$

$$\beta = \frac{1}{2} \left[\arctan\left(\frac{a_{12}-a_{21}}{a_{11}+a_{22}}\right) - \arctan\left(\frac{a_{12}+a_{21}}{a_{11}-a_{22}}\right) \right] \quad (\text{A.21})$$

$$m_x = a_{11} \cos \alpha \cos \beta - a_{22} \sin \alpha \sin \beta + a_{21} \cos \alpha \sin \beta - a_{12} \sin \alpha \cos \beta \quad (\text{A.22})$$

$$m_y = a_{22} \cos \alpha \cos \beta - a_{11} \sin \alpha \sin \beta + a_{21} \sin \alpha \cos \beta - a_{12} \cos \alpha \sin \beta. \quad (\text{A.23})$$

A.10 Factorizing a generalized rotation in phase space

If the given ABCD-matrix is an orthogonal diagonal matrix \mathbf{Q} that satisfies $\mathbf{Q}^T \mathbf{Q} =$

\mathbf{I} , it can be identified as a generalized anisotropic rotation for phase space. In this case, it can be decomposed into two rotation matrices with one intermediate anisotropic rotation of phase space:

$$\mathbf{Q} = \begin{pmatrix} \mathbf{A} & \mathbf{B} \\ \mathbf{C} & \mathbf{D} \end{pmatrix} = \mathbf{R}(\beta) \mathbf{\Psi}(\varphi_x, \varphi_y) \mathbf{R}(\alpha). \quad (\text{A.24})$$

To obtain these parameters, rule R6 is used in the following:

$$\alpha = \frac{1}{2} \left[\arctan \left(\frac{a_{12}+a_{21}}{a_{11}-a_{22}} \right) + \arctan \left(\frac{a_{12}-a_{21}}{a_{11}+a_{22}} \right) \right] \quad (\text{A.25})$$

$$\beta = \frac{1}{2} \left[\arctan \left(\frac{a_{12}-a_{21}}{a_{11}+a_{22}} \right) - \arctan \left(\frac{a_{12}+a_{21}}{a_{11}-a_{22}} \right) \right] \quad (\text{A.26})$$

$$\varphi_x = \arctan \left(\frac{b_{11} \cos \alpha \cos \beta - b_{22} \sin \alpha \sin \beta + b_{21} \cos \alpha \sin \beta - b_{12} \sin \alpha \cos \beta}{a_{11} \cos \alpha \cos \beta - a_{22} \sin \alpha \sin \beta + a_{21} \cos \alpha \sin \beta - a_{12} \sin \alpha \cos \beta} \right) \quad (\text{A.27})$$

$$\varphi_y = \arctan \left(\frac{b_{22} \cos \alpha \cos \beta - b_{11} \sin \alpha \sin \beta + b_{21} \sin \alpha \cos \beta - b_{12} \cos \alpha \sin \beta}{a_{22} \cos \alpha \cos \beta - a_{11} \sin \alpha \sin \beta + a_{21} \sin \alpha \cos \beta - a_{12} \cos \alpha \sin \beta} \right). \quad (\text{A.28})$$

A.11 Realizin a scale matrix

If an optical system for a scale matrix is desired, its realization requires four elements in sequence: **LPLP** or **PLPL**. In addition, solutions for their parameters are not unique. In the following, some useful realizations are given. Using the Kepler telescope, as described in equations A.29 and A.30, the two lenses have focal lengths of (a_x, a_y) and (b_x, b_y) . Using a space-lens-space imaging setup, as described in equations A.31 and A.32, the two propagations have distances of (a_x, a_y) and (b_x, b_y) .

$$\mathbf{S} \left(-\frac{b_x}{a_x}, -\frac{b_y}{a_y} \right) = \mathbf{P} \left(\frac{b_x(a_x+b_x)}{a_x}, \frac{b_y(a_y+b_y)}{a_y} \right) \underbrace{\mathbf{L}(b_x, b_y) \mathbf{P}(a_x + b_x, a_y + b_y) \mathbf{L}(a_x, a_y)}_{\text{Kepler-telescop}} \quad (\text{A.29})$$

$$= \underbrace{\mathbf{L}(b_x, b_y) \mathbf{P}(a_x + b_x, a_y + b_y) \mathbf{L}(a_x, a_y)}_{\text{Kepler-telescop}} \mathbf{P} \left(\frac{(a_x+b_x)a_x}{b_x}, \frac{(a_y+b_y)a_y}{b_y} \right) \quad (\text{A.30})$$

$$= \mathbf{L} \left(\frac{b_x^2}{a_x+b_x}, \frac{b_y^2}{a_y+b_y} \right) \underbrace{\mathbf{P}(b_x, b_y) \mathbf{L} \left(\frac{a_x b_x}{a_x+b_x}, \frac{a_y b_y}{a_y+b_y} \right) \mathbf{P}(a_x, a_y)}_{\text{b-f-g imaging setup}} \quad (\text{A.31})$$

$$= \underbrace{\mathbf{P}(b_x, b_y) \mathbf{L} \left(\frac{a_x b_x}{a_x+b_x}, \frac{a_y b_y}{a_y+b_y} \right) \mathbf{P}(a_x, a_y) \mathbf{L} \left(\frac{a_x^2}{a_x+b_x}, \frac{a_y^2}{a_y+b_y} \right)}_{\text{b-f-g imaging setup}} \quad (\text{A.32})$$

Decomposition is not unique, since for a given $m_{x,y}$ in $\mathbf{S}(m_x, m_y)$, there is a continuous range of solutions for $a_{x,y}$ and $b_{x,y}$, satisfying $m_{x,y} = b_{x,y}/a_{x,y}$. If an anisotropic propagation or an isotropic propagation with negative distance is required in the above equations, they can be realized using decompositions discussed in R13 or R14.

A.12 Realizing a rotation in phase space

If an optical system for a phase space rotation is desired, its realization requires three elements in sequence: **PLP** or **LPL**.

$$\Psi(\varphi_x, \varphi_y) = \mathbf{L} \left(\frac{\sin \varphi_x}{1 - \cos \varphi_x}, \frac{\sin \varphi_y}{1 - \cos \varphi_y} \right) \mathbf{P}(\sin \varphi_x, \sin \varphi_y) \mathbf{L} \left(\frac{\sin \varphi_x}{1 - \cos \varphi_x}, \frac{\sin \varphi_y}{1 - \cos \varphi_y} \right) \quad (\text{A.33})$$

$$= \mathbf{P} \left(\frac{1 - \cos \varphi_x}{\sin \varphi_x}, \frac{1 - \cos \varphi_y}{\sin \varphi_y} \right) \mathbf{L} \left(\frac{1}{\sin \varphi_x}, \frac{1}{\sin \varphi_y} \right) \mathbf{P} \left(\frac{1 - \cos \varphi_x}{\sin \varphi_x}, \frac{1 - \cos \varphi_y}{\sin \varphi_y} \right) \quad (\text{A.34})$$

If an anisotropic propagation or an isotropic propagation with negative distance is required in the above equations, they can be realized using decompositions discussed in R13 or R14.

A.13 Realizing anisotropic propagation

Since anisotropic propagation is excluded from the list of elementary operations, a method is provided for finding minimal optical decomposition for the anisotropic propagation operator:

$$\mathbf{P}(z_x, z_y) \text{ with } z_x \neq z_y. \quad (\text{A.35})$$

The optical realization of anisotropic propagation consists of five elements: **LPLPL**, and has two alternative constructions: if $z_x > z_y$,

$$\begin{aligned} \mathbf{P}(z_x, z_y) &= \mathbf{R}(\pi) \mathbf{L}(z_x - z_y, z_x - z_y) \mathbf{P}(z_x - z_y, z_x - z_y) \\ &\quad \mathbf{L} \left(\frac{(z_x - z_y)^2}{3z_x - 2z_y}, \frac{(z_x - z_y)^2}{2z_x - z_y} \right) \mathbf{P}(z_x - z_y, z_x - z_y) \mathbf{L}(z_x - z_y, z_x - z_y), \end{aligned} \quad (\text{A.36})$$

if $z_x < z_y$,

$$\begin{aligned} \mathbf{P}(z_x, z_y) &= \mathbf{R}(\pi)\mathbf{L}(z_y - z_x, z_y - z_x)\mathbf{P}(z_y - z_x, z_y - z_x) \\ &\quad \mathbf{L}\left(\frac{(z_y - z_x)^2}{2z_y - z_x}, \frac{(z_y - z_x)^2}{3z_y - 2z_x}\right)\mathbf{P}(z_y - z_x, z_y - z_x)\mathbf{L}(z_y - z_x, z_y - z_x). \end{aligned} \quad (\text{A.37})$$

Both decompositions only contain propagations with positive isotropic distances and can be used even if one of z_x and z_y is zero. In equations A.36 and A.37, only the middle lens is astigmatic, while the other lenses are rotationally symmetric.

A.14 Realizing isotropic propagation with negative distance

Realizing isotropic propagation with a negative distance requires three elements in sequence: **LPL**.

$$\mathbf{P}(-z, -z) = \mathbf{R}(\pi)\mathbf{L}\left(\frac{z}{2}, \frac{z}{2}\right)\mathbf{P}(z, z)\mathbf{L}\left(\frac{z}{2}, \frac{z}{2}\right) \quad (\text{A.38})$$

Here, $\mathbf{R}(\pi)$ implies inverting the detector plane.

Bibliography

- [AM83] H. H. Arsenault and B. Macukow. Factorization of the transfer matrix for symmetrical optical systems. *J. Opt. Soc. Am.*, 73:1350–1359, 1983.
- [Ars80] H. H. Arsenault. Generalization of the principal plane concept in matrix optics. *Am. J. Phys.*, 48:397–399, 1980.
- [AS94] S. Abe and J. T. Sheridan. Optical operations on wave functions as the abelian subgroups of the special affine fourier transformation. *Opt. Lett.*, 19:1801–1803, 1994.
- [BA06] M. J. Bastiaans and T. Alieva. Synthesis of an arbitrary abcd-system with fixed lens positions. *Opt. Lett.*, 31:2414–2416, 2006.
- [BBDE01] G. Birkel, F.B.J. Buchkremer, R. Dumke, and W. Ertmer. Atom optics with microfabricated optical elements. *Opt. Commun.*, 191:67–81, 2001.
- [BK62] G. D. Boyd and H. Kogelnik. Generalised confocal resonator theory. *Bell Sys. Tech. J.*, 41:1347–1369, 1962.
- [BKC98] S. B. Bollepalli, M. Khan, and F. Cerrina. Modeling image formation in layered structures: Application to x-ray lithography. *Proc. MSM*, 1:53–58, 1998.
- [BKK⁺92] K.-H. Brenner, M. Kufner, S. Kufner, J. Moisel, A. Müller, S. Sinzinger, M. Testorf, J. Götttert, and J. Mohr. Application of three-dimensional micro-optical components formed by lithography, electroforming, and plastic molding. *Appl. Opt.*, 32:6464–6469, 1992.
- [Bou54] C. J. Bouwkamp. Diffraction theory. *Rep. Prog. Phys.*, 17:35–100, 1954.

- [Bre00] K.-H. Brenner. Method for designing arbitrary two-dimensional continuous phase elements. *Opt. Lett.*, 25:31–33, 2000.
- [BS88] K. H. Brenner and F. Sauer. Diffractive reflective optical interconnects. *Appl. Opt.*, 27:4251–4254, 1988.
- [BW99] M. Born and E. Wolf. *Principles of Optics*. Cambridge University Press, 7.th edition, 1999.
- [Cas81] L. W. Casperson. Synthesis of gaussian beam optical systems. *Appl. Opt.*, 20:2243–2249, 1981.
- [DDB02a] D. Dragoman, M. Dragoman, and K.-H. Brenner. Amplitude and phase recovery of rotationally symmetric beams. *Appl. Opt.*, 41:5512–5518, 2002.
- [DDB02b] D. Dragoman, M. Dragoman, and K.-H. Brenner. Tomographic amplitude and phase recovery of vertical-cavity surface-emitting lasers by use of the ambiguity function. *Opt. Lett.*, 27:1519–1521, 2002.
- [Dem03] W. Demtröder. *Laser Spectroscopy*. Springer Verlag, Berlin - Heidelberg, 2003.
- [DH97] N. Delen and B. Hooker. Free-space beam propagation between arbitrarily oriented planes based on full diffraction theory: a fast fourier transform approach. *J. Opt. Soc. Am. A*, 15:857–867, 1997.
- [Dra03] D. Dragoman. Redundancy of phase-space distribution functions in complex field recovery problems. *Appl. Opt.*, 42:1932–1937, 2003.
- [Dra05] D. Dragoman. Reply to comment on 'redundancy of phase-space distribution functions in complex field recovery problems'. *Appl. Opt.*, 44:58–59, 2005.
- [Fie78] J. R. Fienup. Reconstruction of an object from the modulus of its fourier transform. *Opt. Lett.*, 3:27–29, 1978.
- [Fie79] J. R. Fienup. Space object imaging through the turbulent atmosphere. *Opt. Eng.*, 18:529–534, 1979.

- [Fie80] J. R. Fienup. Iterative method applied to image reconstruction and to computer generated holograms. *Opt. Eng.*, 19:297–305, 1980.
- [FKC⁺00] R. Folman, P. Krüger, D. Cassettari, B. Hessmo, T. Maier, and J. Schmiedmayer. Controlling cold atoms using nano-fabricated surfaces: Atom chips. *Phys.Rev. Lett.*, 84:4749–4752, 2000.
- [FKS⁺02] R. Folman, P. Krüger, J. Schmiedmayer, J. Denschlag, and C. Henkel. Microscopic atom optics: From wires to an atom chip. *Adv. At. Mol. Opt. Phys.*, 48:263–356, 2002.
- [FM97] D. G. Flagello and T. D. Milster. High-numerical-aperture effects in photoresist. *Appl. Opt.*, 36:8944–8951, 1997.
- [FMR96] D. G. Flagello, T. Milster, and A. E. Rosenbluth. Theory of high-na imaging in homogeneous thin film. *J. Opt. Soc. Am. A*, 13:53–64, 1996.
- [Fou59] L. M. Foucault. Memoire sur la construction des telescopes en verre argente. *Ann. Obs. Imp. Paris*, 5:197–237, 1859.
- [GN96] T. E. Gureyev and K. A. Nugent. Solution of the transport-of-intensity equation with nonuniform intensity. *J. Opt. Soc. Am. A*, 13:1670–1682, 1996.
- [Goo96] J. Goodman. *Introduction to Fourier Optics*. McGraw-Hill, New York, 2nd edition, 1996.
- [GRN95] T. E. Gureyev, A. Roberts, and K. A. Nugent. Phase retrieval with the transport-of-intensity equation: matrix solution with use of zernike polynomials. *J. Opt. Soc. Am. A*, 12:1932–1941, 1995.
- [Gro93] C. W. Groetsch. *Inverse problems in the mathematical sciences*. Braunschweig Wiesbaden: Vieweg, 1993.
- [GS72] R. W. Gerchberg and W. O. Saxton. A practical algorithm for the determination of phase from image and diffraction plane pictures. *Optik*, 35:237–246, 1972.

- [GT98] A. Ghatak and K. Thyagarajan. *Introduction to fiber optics*. Cambridge University Press, 1998.
- [GvL96] G. H. Golub and C. van Loan. *Matrix computations*. The Johns Hopkins University Press, 3rd edition, 1996.
- [HKH⁺03] P. Horak, B.G. Klappauf, A. Haase, R. Folman, J. Schmiedmayer, P. Domokos, and E.A. Hinds. Possibility of single atom detection on a chip. *Phys. Rev. A*, 67:043806/1–9, 2003.
- [Hön52] H. Hönl. Eine strenge formulierung des klassischen beugungsproblems. *Z. Physik*, 131:290–304, 1952.
- [Hop77] H. H. Hopkins. Image formation with coherent and partially coherent light. *Photogr. Sci. Eng.*, 21:114–123, 1977.
- [JB04] J. Jahns and K.-H. Brenner. *Microoptics - From Technology to Applications*. Springer, 2004.
- [JH89] J. Jahns and A. Huang. Planar integration of free-space optical components. *Appl. Opt.*, 28:1602–1605, 1989.
- [JLS99] Xunya Jiang, Qiming Li, and C. M. Soukoulis. Symmetry between absorption and amplification in disordered media. *Phys. Rev. B*, 59:R9007, 1999.
- [Lal68] E. Lalor. Conditions for the validity of the angular spectrum of plane waves. *J. Opt. Soc. Am.*, 58:1235–1237, 1968.
- [LB03] X. Liu and K.-H. Brenner. Reconstruction of two-dimensional complex amplitudes from intensity measurements. *Opt. Commun.*, 225:19–30, 2003.
- [LBW⁺05] X. Liu, K. H. Brenner, M. Wilzbach, M. Schwarz, T. Fernholz, and J. Schmiedmayer. Fabrication of alignment structures for a fiber resonator by use of deep-ultraviolet lithography. *Appl. Opt.*, 44:6857–6860, 2005.
- [Loh93] A. W. Lohmann. Image rotation, wigner rotation, and the fractional fourier transform. *J. Opt. Soc. Am. A*, 10:2181–2186, 1993.

- [LW55] A. Lohmann and H. Wegener. Behandlung der optischen abbildung durch entwicklung nach ebenen wellen. *Zeitschrift für Physik*, 143:431–434, 1955.
- [MA83] B. Macukow and H. H. Arsenault. Matrix decompositions for nonsymmetrical optical systems. *J. Opt. Soc. Am.*, 73:1360–1366, 1983.
- [MBC⁺95] D. F. McAlister, M. Beck, L. Clarke, A. Mayer, and M. G. Raymer. Optical phase retrieval by phase-space tomography and fractional-order fourier transformation. *Opt. Lett.*, 20:1181–1183, 1995.
- [NS82] M. Nazarathy and J. Shamir. First-order optics - a canonical operator representation: lossless systems. *J. Opt. Soc. Am.*, 72:356–364, 1982.
- [Oug98] Kurt Edmund Oughstun. The angular spectrum representation and the sherman expansion of pulsed electromagnetic beam fields in dispersive, attenuative media. *Pure Appl. Opt.*, 7:1059–1078, 1998.
- [PB97] C. Palma and V. Bagini. Extension of the fresnel transform to abcd systems. *J. Opt. Soc. Am. A*, 14:1774–1779, 1997.
- [PO06] P. Almoró G. Pedrini and W. Osten. Complete wavefront reconstruction using sequential intensity measurements of a volume speckle field. *Appl. Opt.*, 45:8596–8605, 2006.
- [POZ05] G. Pedrini, W. Osten, and Y. Zhang. Wave-front reconstruction from a sequence of interferograms recorded at different planes. *Opt. Lett.*, 30:833–835, 2005.
- [PTVF92] W. H. Press, S. A. Teukolsky, W. T. Vetterling, and B. P. Flannery. *Numerical Recipes in C*. Cambridge University Press, 2nd edition, 1992.
- [RA03] S. A. Ramakrishna and A. D. Armour. Propagating and evanescent waves in absorbing media. *Am. J. Phys.*, 71:562–567, 2003.
- [Rag96] R. Ragazzoni. Pupil plane wavefront sensing with an oscillating prism. *J. of Mod. Opt.*, 43:289–293, 1996.
- [Ram04] S. A. Ramakrishna. On the dual symmetry between absorbing and amplifying random media. *PRAMANA J. o. Phys.*, 62:1273–1279, 2004.

- [RBM94] M. G. Raymer, M. Beck, and D. F. McAllister. Complex wave-field reconstruction using phase-space tomography. *Phys. Rev. Lett.*, 72:1137–1140, 1994.
- [RPF⁺] R. Ruhmann, K. Pfeiffer, M. Falenski, F. Reuther, R. Engelke, and G. Grützner. Su-8: a high performance material for mems applications. Technical report.
- [SC02] B. W. Smith and J. Cashmore. Challenges in high na, polarization, and photoresists. *Proc. SPIE*, 4691:11–24, 2002.
- [Sch42] H. Scheffers. Vereinfachte ableitung der formeln für die fraunhoferschen beugungserscheinungen. *Annalen der Physik*, 434:211–215, 1942.
- [She67] G. C. Sherman. Application of the convention theorem to rayleigh’s integral formulars. *J. Opt. Soc. Am.*, 57:546–547, 1967.
- [Sie86] A.E. Siegman. *Lasers*. University Science Books, Mill Valley, CA, 1986.
- [SM98] R. Simon and N. Mukunda. Iwasawa decomposition in first-order optics: universal treatment of shape-invariant propagation for coherent and partially coherent beams. *J. Opt. Soc. Am. A*, 15:2146–2155, 1998.
- [SMS85] E.C.G. Sudarshan, N. Mukunda, and R. Simon. Realisation of first order optical systems using thin lenses. *OPTICA ACTA*, 32:855–872, 1985.
- [SN79] M. Saruwatari and K. Nawate. Semiconductor laser to single-mode fiber coupler. *Appl. Opt.*, 18:1847–1856, 1979.
- [SP71] R. V. Shack and B. C. Platt. Production and use of a lenticular hartmann screen. *J. Opt. Soc. Am.*, 61:656, 1971.
- [SS81] Jakob J. Stamnes and Bjorn Spjelkavik. Focusing at small angular apertures in the debye and kirchhoff approximations. *Opt. Commun.*, 40:81–85, 1981.
- [ST04] A. Semichaevsky and M. Testorf. Phase-space interpretation of deterministic phase retrieval. *J. Opt. Soc. Am. A*, 21:2173–2179, 2004.

- [Sta86] Jakob J. Stamnes. *Waves in focal regions: propagation, diffraction and focusing of light, sound and water waves*. Bristol [u.a.] : Hilger, 1986.
- [Str84] N. Streibl. Phase imaging by the transport equation of intensity. *Opt. Commun.*, 49:6–10, 1984.
- [Tea83] M. R. Teague. Deterministic phase retrieval: a green's function solution. *J. Opt. Soc. Am. A*, 73:1434–1441, 1983.
- [Tes05] M. Testorf. Comment on 'redundancy of phase-space distribution functions in complex field recovery problems'. *Appl. Opt.*, 44, 2005.
- [TT97a] J. Tu and S. Tamura. A new technique for reconstruction of a complex wave field by means of measurement of three-dimensional intensity. *SPIE*, 3170:108–115, 1997.
- [TT97b] Jinhong Tu and Shinichi Tamura. Wave field determination using tomography of the ambiguity function. *Phys. Rev. E*, 55:1946–1949, 1997.
- [TVLB95] P. Török, P. Varga, Z. Laczik, and G. R. Booker. Electromagnetic diffraction of light focused through a planar interface between materials of mismatched refractive indices: an integral representation. *J. Opt. Soc. Am. A*, 12:325–332, 1995.
- [Wey19] H. Weyl. Ausbreitung elektromagnetischer wellen über einem ebenen leiter. *Ann. Physik*, 60:481–500, 1919.
- [WHS⁺06] M. Wilzbach, A. Haase, M. Schwarz, D. Heine, K. Wicker, X. Liu, K.-H. Brenner, S. Groth, Th. Fernholz, B. Hessmo, and J. Schmiedmayer. Detecting neutral atoms on an atom chip. *Fortschr. Phys.*, 54:746–764, 2006.
- [Wic06] K. Wicker. Micro cavities for cavity qed. Master's thesis, University of Heidelberg, 2006.
- [Wil07] M. Wilzbach. *Single atom detection on an atom chip with integrated optics*. PhD thesis, University of Heidelberg, 2007.
- [WL81] E. Wolf and Y. Li. Conditions for the validity of the debye integral representation of focused fields. *Opt. Commun.*, 39:205–210, 1981.

- [Wol59] E. Wolf. Electromagnetic diffraction in optical systems. i. an integral representation of the image field. *Proc. R. Soc. London Ser. A*, 253, 1959.
- [Wol04] K. B. Wolf. *Geometric Optics on Phase Space*. Springer, Berlin, 2004.
- [ZMD96] Z. Zalevsky, D. Mendlovic, and R. G. Dorsch. Gerchberg-saxton algorithm applied in the fractional fourier or the fresnel domain. *Opt. Lett.*, 21:842–844, 1996.

Acknowledgements

I would like to express my gratitude to all of those who contributed to the success of this thesis.

- Thank you very much, Professor Brenner, for supervising this thesis, for your fruitful discussions that stimulated my interests in many fields and for allowing me the scientific freedom necessary to accomplish this thesis.
- I would like to thank Professor Jahns for furnishing a second opinion on this thesis.
- Special thanks to Mr. Stumpfs for his technical assistance and to Mrs. Volk for her organizational support.
- I would also like to thank all of my diploma students for putting so much effort into the experiment. Particularly, thank you, Christian Hruscha, for your efforts in obtaining successful experimental results in phase reconstruction and for your brilliant idea of minimizing experimental errors.
- Particularly, I want to thank Marco Wilzbach, Kai Wicker and Prof. Schmiedmayer of the University of Heidelberg, for their fruitful cooperation in applying the micro optical elements produced by lithography in atomic physics.
- Thank you very much, Jianjun, for all of your care, support, and patience over these years.

About the author

Xiyuan Liu was born May 7, 1974, in P.R. China. Beginning in 1991, she studied Mechanical Electronics Engineering at the Xi'an Institute of Technology, P.R. China, and obtained a Bachelor of Engineering in 1995. In 1998, she began studying computer engineering at the University of Mannheim, Germany. Her subjects of study include optoelectronics, communications engineering and image processing. Her diploma thesis, written in 2002, is entitled "*Reconstruction of the light phases by use of the Ambiguity-function*". Following this, she began her PhD work with the Chair of Optoelectronics, Professor Brenner, at the University of Mannheim, Germany.

List of publications

Conference Proceedings

- X. Liu and K.-H. Brenner, *Reconstruction of two-dimensional complex amplitudes from intensity measurements*, IOG 2002, Proceedings 1st Workshop Information Optics, 67-73, ISSN 1684-7296, Mannheim (2002)
- X. Liu and K.-H. Brenner, *Nichtinterferometrische Rekonstruktion komplexer zweidimensionaler Wellenfelder aus Intensitätsmessungen*, 105th Annual Meeting in Bad Kreuznach/Germany (2004)
- X. Liu and K.-H. Brenner, *New treatment of light propagation in absorbing media*, 106th Annual Meeting in Breslau/Polen(2005)
- X. Liu, K.-H. Brenner, M. Wilzbach, M. Schwarz, T. Fernholz and J.Schmiedmayer,

Integrated fiber resonator for atom detection using deep UV-lithography, 106th Annual Meeting in Breslau/Polen(2005)

- X. Liu, K.-H. Brenner and C. Hruscha, *Efficient reconstruction of two-dimensional complex amplitudes using the ambiguity function of one-dimensional slices*, EOS Topical Meeting On Advanced Optical Imaging Techniques, London, pp. 40-41, ISBN 3-00-016360-3 (2005)
- X. Liu and K.-H. Brenner, *Effiziente Rekonstruktion zweidimensionaler komplexer Amplituden mit der Ambiguity-Funktion von eindimensionalen Schnitten*, 107th Annual Meeting in Weingarten/Germany (2006)
- X. Liu, C. Hruscha and K.-H. Brenner, *Efficient reconstruction of two-dimensional complex amplitudes using the Ambiguity function of one-dimensional slices*, ICO Topical Meeting on Optoinformatics/Information Photonics, St. Petersburg/Russia (2006)
- X. Liu and K.-H. Brenner, *Effiziente numerische Behandlung teilkohärenter Lichtausbreitung*, 107th Annual Meeting in Weingarten/Germany, DGaO-Proceedings, ISSN: 1614-8436, <http://www.dgao-proceedings.de> (2006)
- X. Liu and K.-H. Brenner, *Exakte Intensitäts- bzw. Energiefluss-Berechnung eines skalaren Lichtfelds*, 108th Annual Meeting in Seebad Heringsdorf/Germany (2007)
- X. Liu and K.-H. Brenner, *Anwendung der Tiefenlithographie für die Spleißung von Monomodefasern*, 109th Annual Meeting in Esslingen/Germany (2008)

Refereed Journals

- X. Liu and K.-H. Brenner, *Reconstruction of two-dimensional complex amplitudes from intensity measurements*, Opt. Commun., Vol. **225**, pp. 19-30 (2003)
- X. Liu, K.-H. Brenner, M. Wilzbach, M. Schwarz, T. Fernholz and J. Schmiedmayer, *Fabrication of alignment structures for a fiber resonator by use of deep-ultraviolet lithography*, Appl. Opt. **44**, pp. 6857-6860 (2005)

-
- M. Wilzbach, A. Haase, M. Schwarz, D. Heine, K. Wicker, X. Liu, K.-H. Brenner, S. Groth, Th. Fernholz, B. Hessmo and J. Schmiedmayer, *Detecting Neutral Atoms on an Atom Chip*, Fortschr. Phys. **54**, 746-764 (2006)
 - M. Wilzbach, D. Heine, S. Groth, X. Liu, B. Hessmo and J. Schmiedmayer, *A simple integrated single-atom detector*, arXiv:0801.3255v1 (2008)
 - X. Liu, C. Hruscha and K.-H. Brenner, *Efficient reconstruction of two-dimensional complex amplitudes utilizing the redundancy of the ambiguity function*, Appl. Opt. **47**, E1-E7 (2008)
 - X. Liu and K.-H. Brenner, *Minimal optical decomposition of ray transfer matrices*, Appl. Opt. **47**, E88-E98 (2008)
 - X. Liu and K.-H. Brenner, *Tiefenlithographie zum Spleißen von Singlemodefasern*, Photonik 5/2008 (2008)